2014

Analysis of a 10-year Nearshore Wave Database and its Implications to Littoral Processes

Luis Humberto Montoya
University of North Florida, l.montoya.97582@unf.edu

ANALYSIS OF A 10-YEAR NEARSHORE WAVE DATABASE AND ITS IMPLICATIONS TO LITTORAL PROCESSES

by

Luis H. Montoya

A thesis submitted to the

School of Engineering

In partial fulfillment of the requirements for the degree of

Master of Science in Civil Engineering

UNIVERSITY OF NORTH FLORIDA

SCHOOL OF ENGINEERING

April, 2014

The thesis "Analysis of a 10-year Nearshore Wave Database and its Implications to Littoral Processes" submitted by Luis Humberto Montoya in partial fulfillment of the requirements for the degree of Master of Science in Civil Engineering has been

Approved by the thesis committee: Date:

_____ _____

Dr. William R. Dally, PhD, P.E.,
Thesis Advisor and Committee Chairperson

_____ _____

Dr. Don Resio, PhD

_____ _____

Thobias Sando, Ph.D.

Accepted for the School of Engineering:

_____ _____

Murat Tiryakioglu, Ph.D.
Director of the School of Engineering

Accepted for the College of Computing, Engineering, and Construction:

_____ _____

Mark A. Tumeo, Ph.D., P.E.
Dean of the College of Computing, Engineering, and Construction

Accepted for the University of North Florida:

_____ _____

Len Roberson
Dean of the Graduate School

ACKNOWLEDGEMENT

I would like to thank God for his blessings, unconditional love and support throughout these two years. Thanks to Dr. Dally (Advisor and Committee Chair) for his help, support, advices and for providing the valuable data that were used for this thesis. I want to give special thanks to Dr. Resio (Committee Member) for his guidance and support during my research, I will always be grateful to him. Also, thanks to the Taylor Engineering Research Institute for funding my research and to Dr. Sando (Committee Member) and Dr. Bacopoulos for their help and support.

I would like to thank my wife, Monica Collazos, for always being there for me, for her love and for pushing me to become a better student every day. Finally, I want to thank my dad, Eberth Montoya, my mom, Luz Stella Cortes, and brothers, Jose, Ronald and Eberth, because I will be graduating with my masters thanks to their sacrifice, love, and support.

TABLE OF CONTENTS

FIGURES

TABLES

ABSTRACT

The variability of the nearshore wave climate is investigated via the analysis of over 10 years of Acoustic Doppler Current Profiler (ADCP) data from a gauge deployed at Melbourne Beach, FL. Examples of large yearly variability in the significant wave height, peak period, mean direction and energy distribution are found in the data. Estimates of the averaged spectra for the entire record show that the average wave energy is distributed almost symmetrically with the peak being close to shore-normal. It was expected that the peak would be shifted towards the north of shore-normal considering net north to south longshore sediment transport at this location. Further analysis of the directional spectra partitioned into three directional windows reveals that waves from the southeast (avg. H_{mo} = 0.78 m) are less energetic than those from the northeast (avg. H_{mo} = 0.87 m), but they arrive from the south 53% more often.

Additionally, energy-based significant wave height (H_{mo}), peak period (T_p) and mean period (T_{mean}) distributions are studied and modeled with notable success.

Radiation stress (S_{xy}) estimates are computed using both rigorous integration as well as parameter-based approximations. These two estimates are correlated but the parameter-based approximation over predicts S_{xy} by 42%, because this method assigns all the wave energy into one direction (Ruessink et al., 2001).

Finally, it is shown by the S_{xy} total average that the net longshore forcing at this location is indeed north to south, but yearly and seasonal variability were quite high. The results indicate that short-term wave records may not provide accurate information for planning purposes. For

example, if only 3 months of data were collected at this site, there would be a 33% chance that the mean longshore forcing would be erroneously directed from south to north.

Chapter 1:

INTRODUCTION

It is well-established, based on historical shoreline change near inlets in the region, that the net long-term longshore transport in the east coast of Florida (FL) is predominantly north to south (Absalonsen and Dean, 2010). If this is the case, it stands to reason that the net longshore wave forcing should be north-to-south. Figure 1.1 and 1.2 show accretion on the north (updrift) side and erosion on the south (downdrift) side reconciling with the fact that longshore sediment transport is north to south in east FL.This coastal process was examined with a long-term dataset consisting of ten years of nearshore wave measurements. This dataset is very valuable because it is a relatively long record of high-resolution directional spectra measured in the nearshore. This rich dataset was also used to perform the following analyses: 1) to explore the variability in the nearshore wave climate, 2) to quantify the nearshore distribution of energy flux according to the direction and frequencies of waves, 3) to model the energy-based significant wave height, mean period and peak period distributions, 4) to examine the seasonal and annual variability of the radiation stress, and 5) to establish the importance of long-term records.

The Florida Coastal Forcing Project (FCFP) (Leadon, Dally, and Osiecki, 2002) collected slightly more than ten years of nearshore wave data in Melbourne Beach, Florida using an Acoustic Doppler Current Profiler (ADCP). The FCFP dataset is very valuable because it is a relatively long record of high-resolution, directional spectra measured in the nearshore, with nearly a 94% capture rate. Located ~39.3 km south to the entrance of Cape Canaveral Port and ~23.6 km north of Sebastian inlet, the waves measured by the ADCP are an indication of the

coastal processes in these two locations. Figure 1.3 presents a picture with the three locations labeled. The FCFP dataset will give valuable insight in regard to the nearshore processes in east Florida.

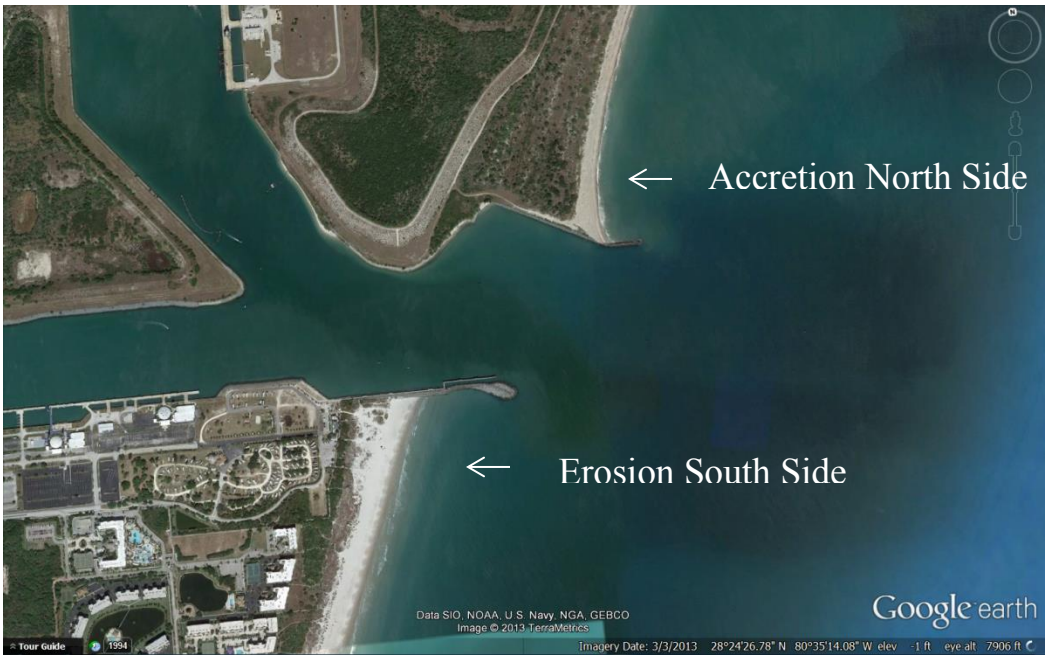

Figure 1.1: Entrance to Port Canaveral, Florida, showing accretion on the updrift (north) side and erosion on the downdrift (south) side as commonly occurs at jettied inlets on Florida's east coast.

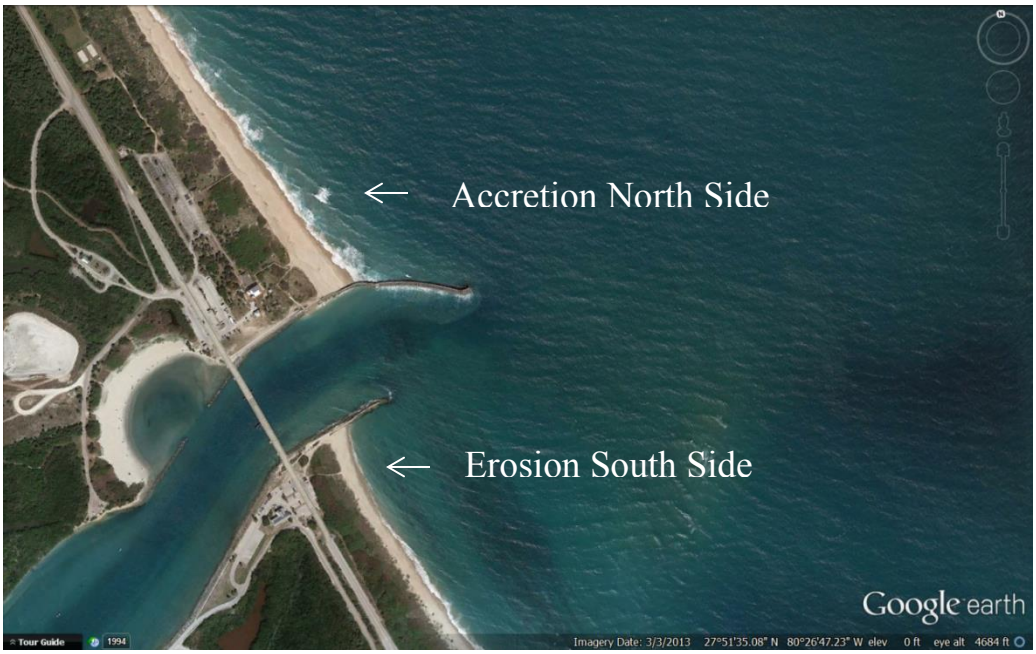

Figure 1.2: Sebastian Inlet, Florida, showing accretion on the updrift (north) side and erosion on the downdrift (south) side

Some of the things that will be learned from this study/analysis are: 1) better information for coastal management, 2) better assessment of wave directionality for wave energy collection in the nearshore, 3) better quantification and understanding of wave climate and longshore forcing and its variability along the coast, 4) better understanding of wave force for sediment movement, 5) long-term modeling of wave parameters, and 6) a better understanding of the importance of maintaining a long-term record.

Currently millions of dollars are being invested annually in our coasts by the construction and maintenance of jetties and inlets, construction and maintenance of ports and other coastal structure, dredging of inlets and channels and beach nourishment projects. There is currently a need of more long-term nearshore wave records. Long-term datasets are needed in order to optimize these investments.

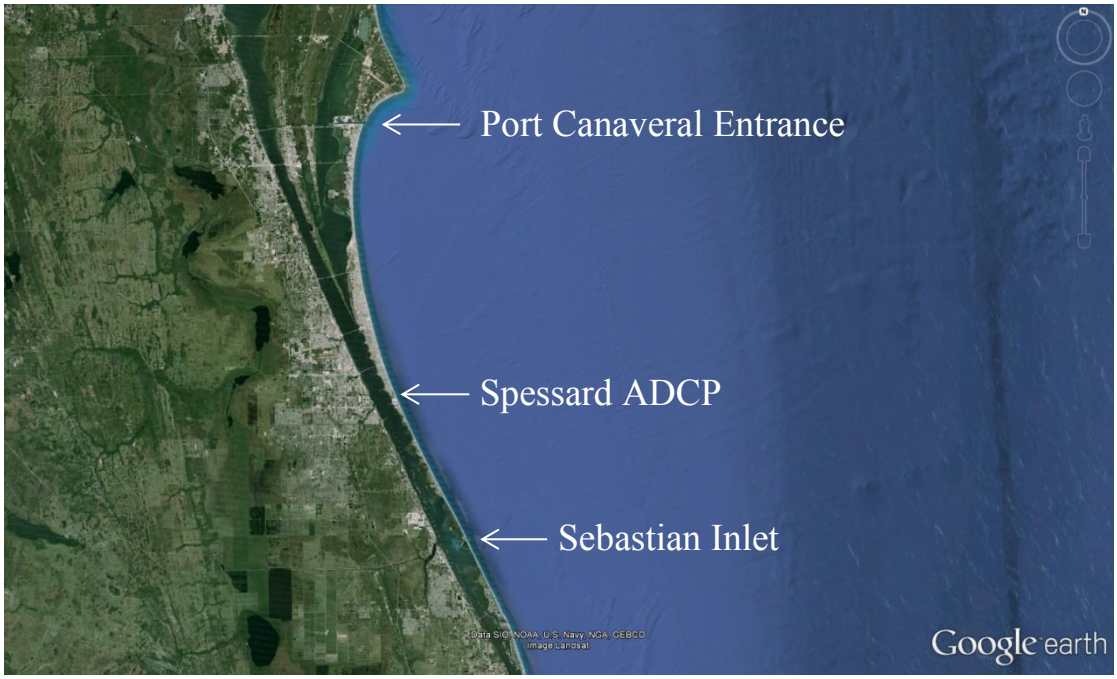

Figure 1.3: East coast of Florida, showing Port Canaveral entrance north of Spessard, the Spessard ADCP in the middle and Sebastian inlet south of Spessard.

1.1 Background on the Spessard Station

The FCFP began in late August of 2001 with the installation of an Acoustic Doppler Current Profiler (ADCP) and a weather station at Spessard Holland North Beach Park in Brevard County, on the coast of east-central Florida (see Appendix A). The wave gauge was located offshore of Spessard Holland Park, approximately 640 m from the dune at a mean depth of ~8.5, m as shown in Figures 1.4 and 1.5 (note the shoreline orientation of 73°). The ADCP collected data for ten years (8/28/01-10/28/11), whereas the weather station instrument (directional anemometer) collected data for six years (9/12/02-10/7/08). A shore station shed was installed at the park, from which a double-armored steel cable ran under the dune and then along the sea floor to the ADCP and was used to power the ADCP and upload collected data.

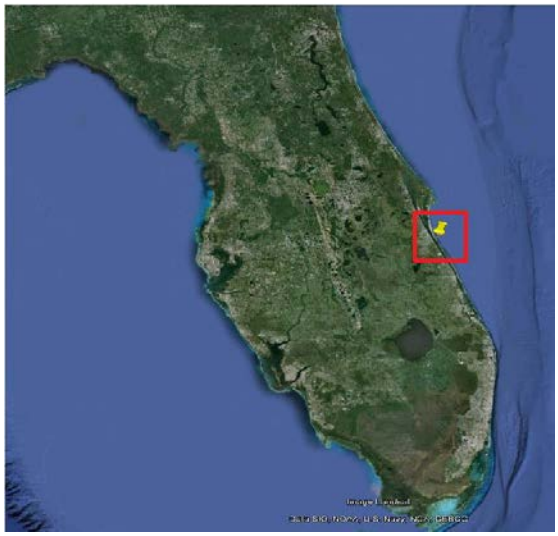

Figure 1.4: The Florida Peninsula, and the location of Melbourne Beach.

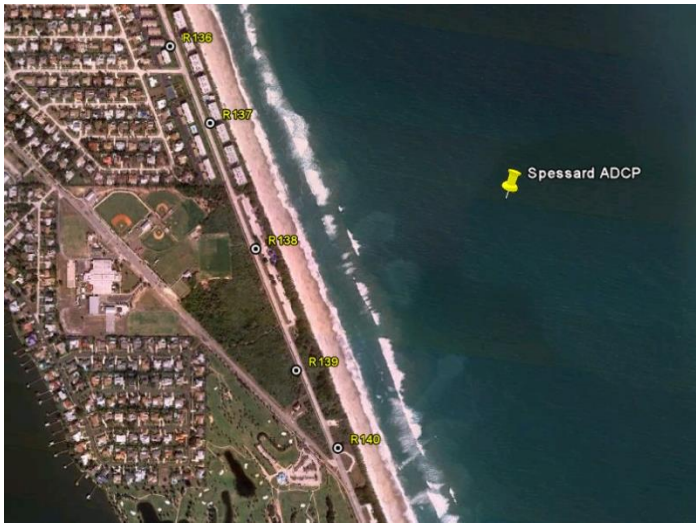

Figure 1.5: Melbourne Beach, showing the location where the ADCP was deployed.

A special mounting structure was designed and fabricated specifically for the ADCP wave gauge. The anchoring/mounting system consisted of a 10 ft. long, 4 in, diameter stainless steel pipe (‘spud’) that was fitted with a coupling flange on one end. The coupling enabled it to be

attached to a boat-based pumping system so that the spud could be jetted into a sand or mud bottom (Figure 1.6). The wave instrument was clamped inside a specially designed aluminum 'hat', which is bolted to the top of the jetted spud. With the spud jetted in place, a diver could retrieve the instrument and replace it with a fresh one, generally requiring only a few minutes of bottom-time.

Figure 1.6: ADCP attached to the jetted spud at Spessard

A jetted spud was used so that the instrument could be located sufficiently above the bed to avoid burial by sediment. The mounting hat and relatively thin spud presented a minimal drag surface, thereby reducing scour potential. As opposed to a bottom-resting frame, the spud always maintained its vertical orientation and did not settle into the bed.

1.2 Data Collection

Two different spud locations, approximately 180 ft. apart, were used during the data collection through the years. Spud 1 was located at N28° 32.672; W80° 32.672', while spud 2 was located at N28° 3.355; W80° 32.701'. Figure 1.7 shows the location of the spuds.

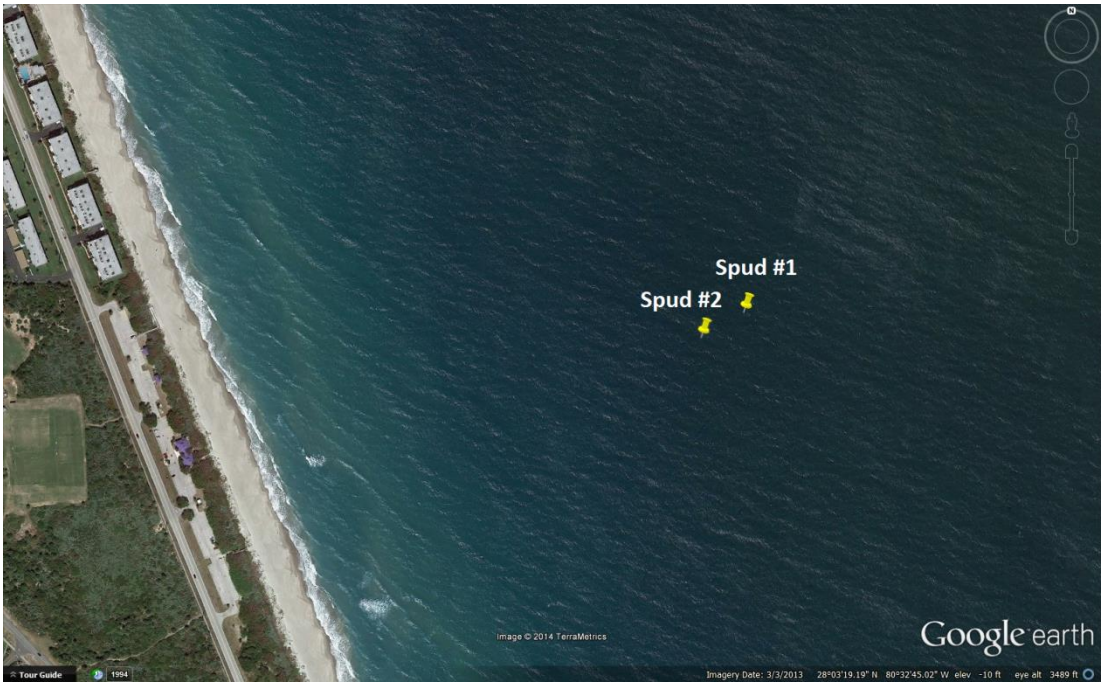

Figure 1.7: Location of the two spuds used for the FCFP.

The ADCP wave gauge has the capability to collect data in cabled and self-recording mode. The FCFP wave record was collected using both modes. In cabled mode, the wave gauge needs to be connected to a power supply and a computer through a special cable, whereas in self-recording mode the gauge needs a battery to be installed internally to operate. The only difference between these two modes, besides the source of energy, is that in cabled mode the data can be acquired

and processed instantaneously (real-time) while in self-recording mode the wave gauge needs to be retrieved to acquire and process the data. The wave gauge was programmed to record measurements for 20 minutes once every two hours.

The FCFP data collection process went smoothly for the majority of the time. The few times when the instrument did not collect data was because of cable failure, power outage, converter failure, gauge malfunction, lightning strikes, and weak batteries. Overall, the wave gauge had a data return rate of approximately 94%.

1.3 Data Processing

The first task was to organize and compile the data onto one hard drive. After compiling the data, some of the files were concatenated in order to reduce the number of files that had to be handled. These files had to be sent to a Teledyne RD Instruments engineer, who concatenated them by year.

The raw data files were then processed using the ADCP manufacturer's (RD Instruments) proprietary software called WavesMon. This software is equipped with a multitude of user-selectable options, which include frequency bands, frequency thresholds, bin selection, number of angles, number of Iterative Maximum Likelihood Method (IMLM) iterations, correction for currents, and wave parameter and spectral output, to name a few. The wave analysis can be performed from several methods including water particle velocity, surface tracking, and pressure, or a combination of the three. Most of the data were processed using measurements of the water particle velocity, but when a beam went bad during the deployment then pressure or surface track would be used. Also, there were a few times when the pressure gauge clogged during a

deployment so surface track had to be used. A comprehensive analysis of all the options and methods available in this software is beyond the scope of this thesis. Thus far all of the data were processed using default values except for: frequency bands were changed from 64 to 128, altitude of the ADCP above the bottom was adjusted depending on the spud (spud #1 altitude= 1 m, spud #2 altitude: 1.5 m) and the IMLM iterations were set to 3.

The raw data files were processed using 'Format 8' of the WavesMon software, which generated both a wave parameter file and a directional spectra file. Appendix B shows a sample wave parameter file and directional spectra file. For consistency, all of the raw data was processed using Format 8.

1.4 Other Available Long-Term Records

The US Army Corps of Engineers Field Research Facility (FRF), located in Duck, NC, was established in 1977. This is one of the few facilities in the US with a long-term wave database. One part of the FRF program consists of a linear array of pressure transducers installed at the 8 m depth contour (U.S. Army, 2014). This methodology is good for measuring directional wave spectra except when currents are present, because pressure gauges do not recognize the currents. Unlike the pressure gauges, the ADCP can measure the current depth profile as well as the directional wave spectra.

Thanks to this database many different processes have been studied and much advancement has been made. Numerical models have been validated and calibrated and our understanding of the coastal processes has increased. To keep increasing the knowledge and the advancement within this field more accurate studies have to be made with small margins of error. This is one of the

reasons why the FRF and FCFP databases are so valuable. Currently there is a need in Florida for more long-term datasets to better understand the processes that take place on the coast.

Chapter 2:

DATA PROCESSING RESULTS

Chapter 2 presents the data processing results from the Spessard station, in which the focus is to explore the variability in the wave record. The first part of the chapter will present an overview of the entire data record via the energy-based significant wave height, H_{mo}. Two sample years were chosen (2002-2003 and 2004-2005) to be compared and contrasted according to their significant wave height (H_{mo}), peak period (T_p) and mean direction (θ_{mean}). An explanation on how these years were chosen is provided in section 2.1. Time series for the whole record are also presented in Appendix C so that the reader can examine them fully. Finally, this chapter presents an averaged 2D spectrum and directional distribution analysis for the selected years and the entire record.

2.1 Analysis of Basic Wave Parameters

Figure 2.1 presents a time series of energy-based significant wave height, H_{mo} measured at Spessard Holland North Beach Park between August 28, 2001 and October 28, 2011. The few gaps of significance in the record are noted and the cause of each is provided. The record includes data from Hurricane Jeanne (9/25/04) and Hurricane Wilma (10/24/05), but not Hurricane Francis (9/04/04) due to a power outage. Furthermore, some of the years have active storm seasons while others do not, suggesting significant variability in the wave forcing from one year to another.

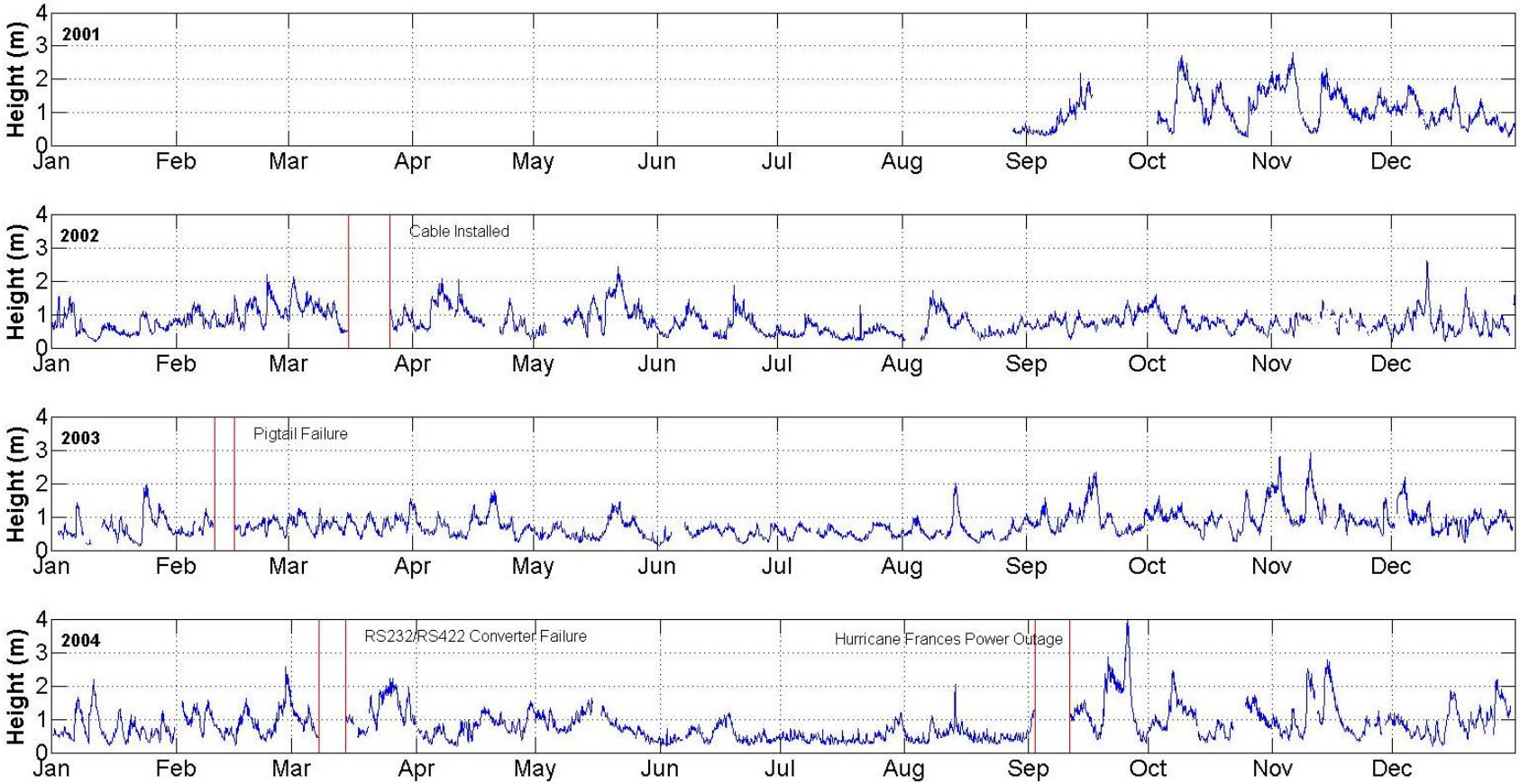

Figure 2.1a: Record of energy-based significant wave height (H_{mo}) from the Spessard Station (continued).

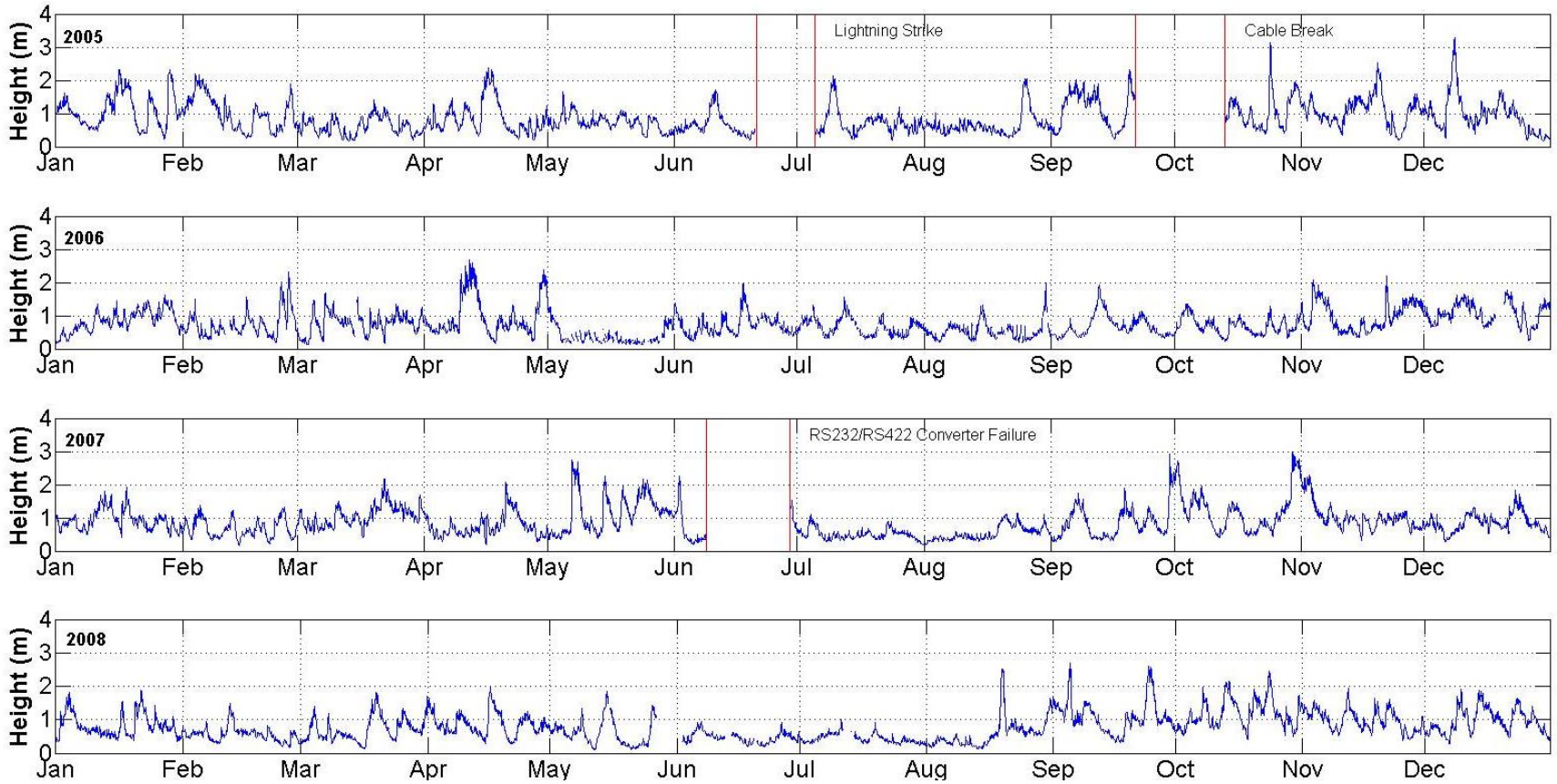

Figure 2.1b: Record of energy-based significant wave height (H_{mo}) from the Spessard Station (continued).

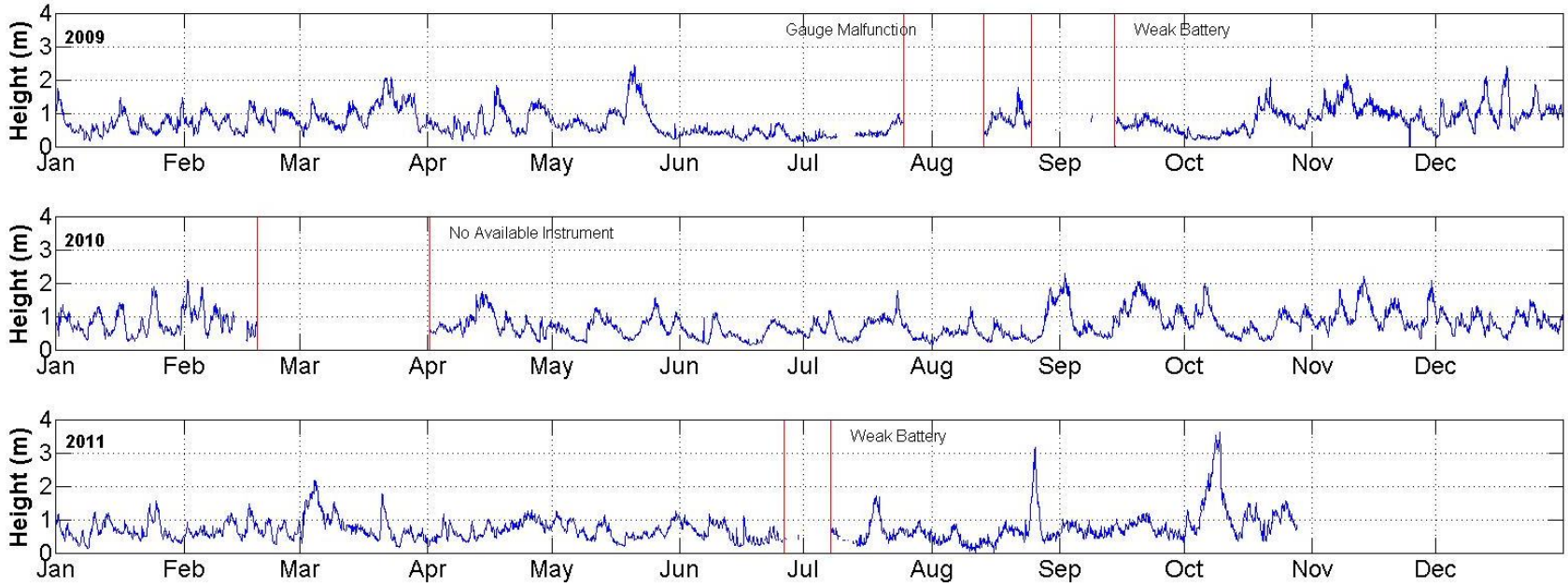

Figure 2.1c: Record of energy-based significant wave height (H_{mo}) from the Spessard Station (concluded).

Cumulative total wave power was computed for each year, starting Sept. 1 and ending Aug. 30 of the subsequent year, using the full spectrum. Cumulative wave power is defined as.

$$Wave\ \ Power = \int_{t_1}^{t_2} \int_{0}^{\infty} \int_{-\pi}^{\pi} E(f,\theta) c_g(f) d\theta\ df\ dt \qquad (2.1)$$

in which $E(f,\theta)$ is the frequency-direction energy spectrum, $c_g(f)$ is the frequency dependent group velocity and t_1 and t_2 are the start and stop dates that define a period. By calculating power, active and calm years can be identified. Table 2.1 presents the results ranked from largest to smallest cumulative power. The time period of 2004-2005 (referred to as 04-05 hereafter) had the largest cumulative wave power of 85,912 MW per unit length of beach, whereas 2002-2003 (referred as 02-03 hereafter) had the smallest cumulative power of 42,776 MW per unit length of beach. The difference in cumulative wave power between these two periods is large [43,135 MW], indicating very different wave climates, which that can be compared and contrasted.

Table 2.1: Cumulative Wave Power

Ranking	Time Period	MW per unit length of beach
1	**9-01-04 to 9-01-05**	85,912
2	**9-01-06 to 9-01-07**	81,281
3	**9-01-01 to 9-01-02**	80,152
4	**9-01-08 to 9-01-09**	73,876
5	**9-01-03 to 9-01-04**	70,389
6	**9-01-05 to 9-01-06**	68,309
7	**9-01-07 to 9-01-08**	63,686
8	**9-01-10 to 9-01-11**	63,364
9	**9-01-09 to 9-01-10**	52,134
10	**9-01-02 to 9-01-03**	42,776

Figures 2.2, and 2.3, present time series of some of the wave parameters measured by the ADCP during 02-03 and 04-05, respectively. The top panel in each figure contains the energy-based significant wave height, the middle panel presents the dominant wave period, and the bottom panel provides the mean wave direction.

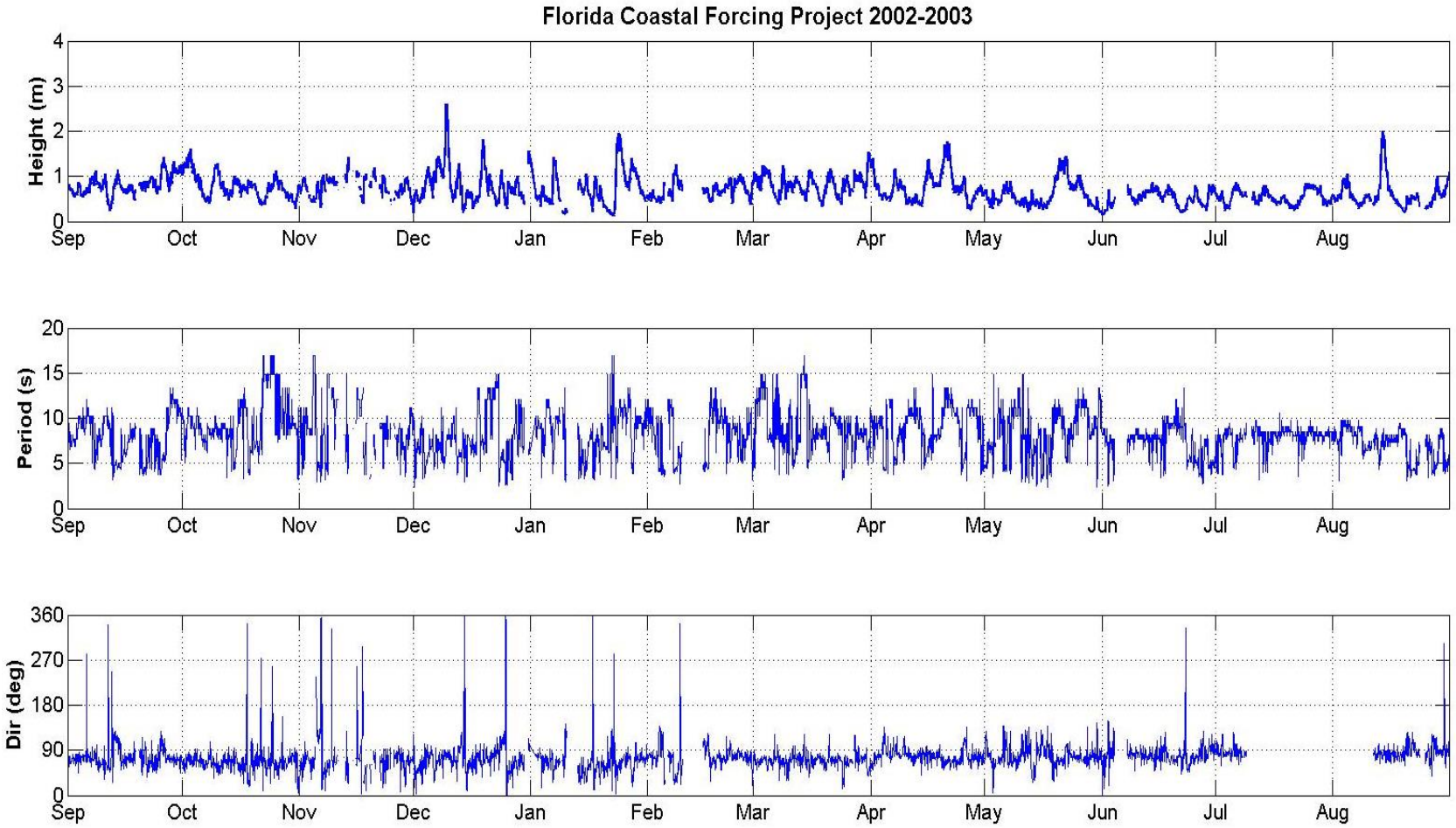

Figure 2.2: Record of energy-based significant wave height (H_{mo}), Peak Period (T_p) and Mean Direction (θ_{mean}) from the Spessard Station 2002-2003.

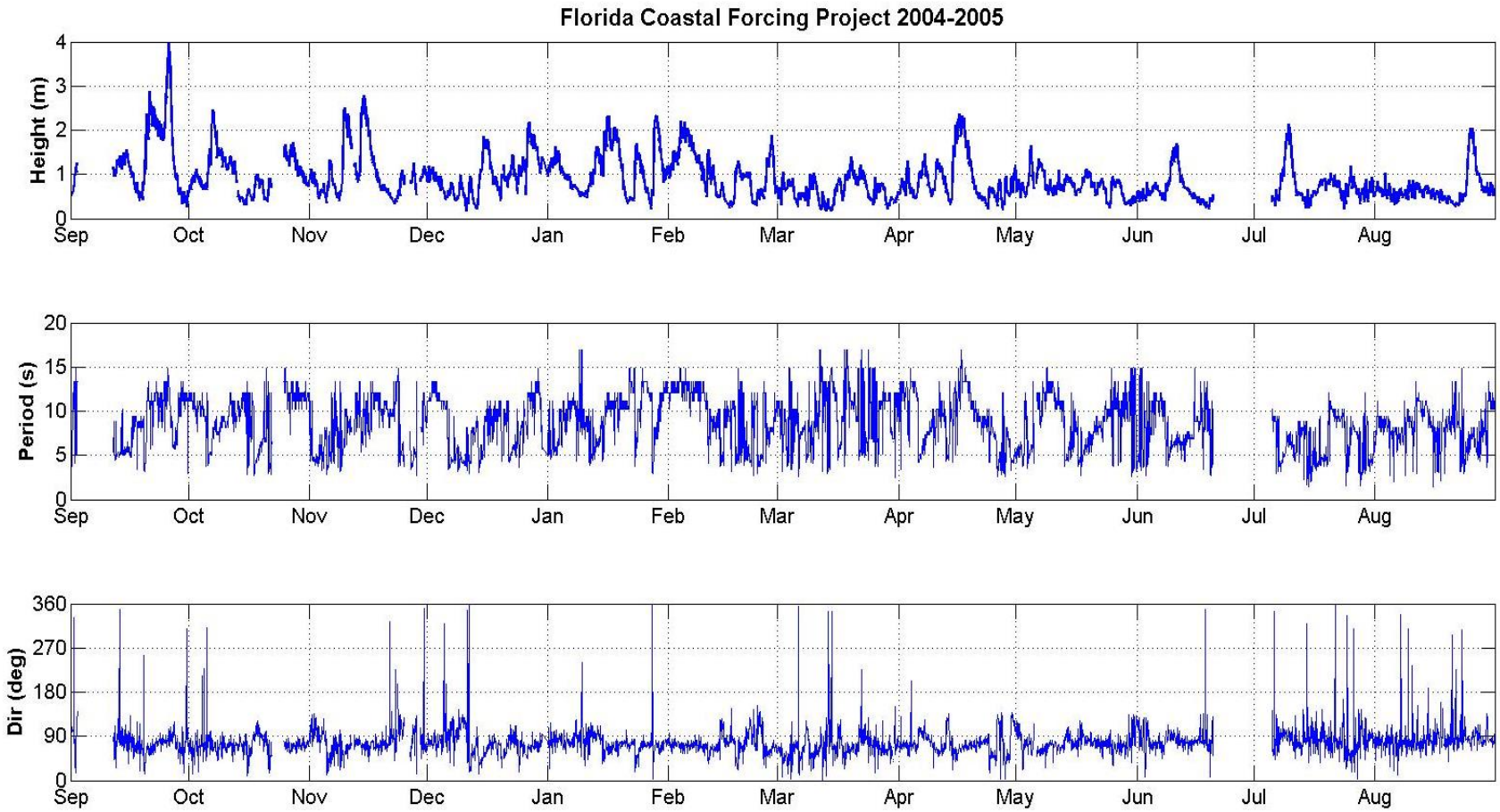

Figure 2.3: Record of energy-based significant wave height (H_{mo}), Peak Period (T_p) and Mean Direction (θ_{mean}) from the Spessard Station 2004-2005.

By inspecting the panels of significant wave height, it can be noted that 02-03 was a relatively calm year, e.g. five storms occurred in which the significant wave height in the nearshore exceeded 1.5 m. The average significant wave height was 0.69 m. with a standard deviation of 0.29 m and with a skew of 1.16. Figure 2.4a presents the wave height distribution for this year with the calculated statistics. The maximum wave height for this year was 2.6 m, while the minimum was 0.12 m.

In distinct contrast, the 04-05 year was a very active year. A total of fifteen storms occurred in which the significant wave height in the nearshore exceeded 1.5 m, and one of these had waves greater than 4 m (Hurricane Jeanne in October of 2004). The average significant wave height was 0.89 m with a standard deviation of 0.51 m and with a skew of 1.53. Figure 2.4b presents the wave height distribution for this year with the calculated statistics. For this year the maximum wave height was 4.01 m, while the minimum was 0.17 m. The maximum wave height was recorded during hurricane Jeanne. It is important to note that the maximum wave height during hurricane Francis was comparable to that of hurricane Jeanne. Averages would increase if measurements from Francis were included.

(a)

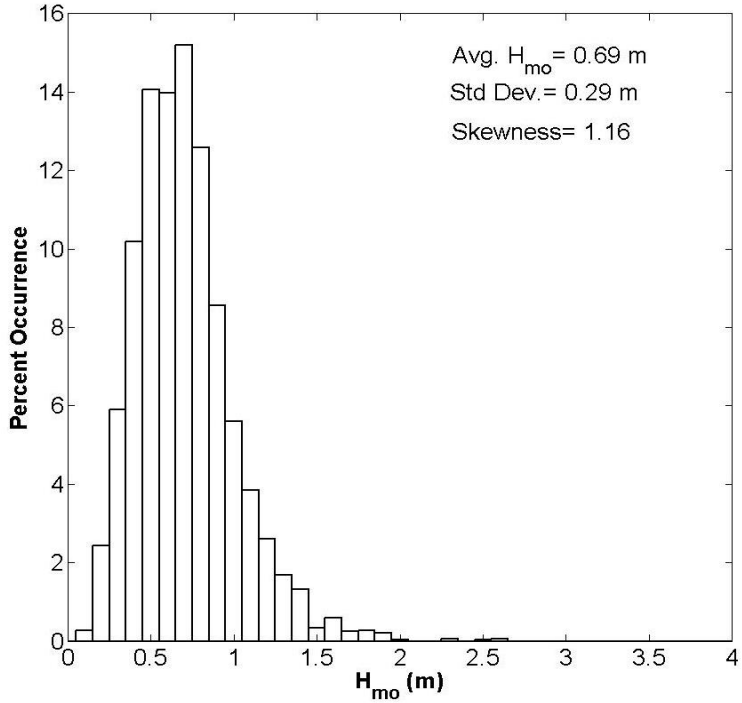

(b)

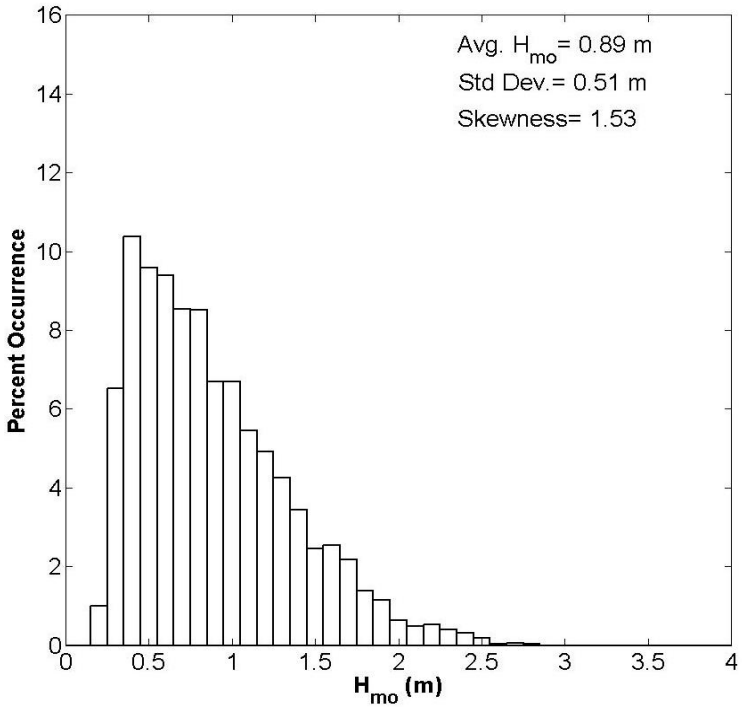

Figure 2.4: Histogram of H_{mo} a) 2002-2003, b) 2004-2005.

The second panels of Figures 2.2 and 2.3 present peak periods for the two years being compared. The instability of peak periods is due to the short period waves generated by the local wind competing with the long period waves that approach from distant sources. For 02-03 the average T_p was 8.21 s with a standard deviation of 2.58 s and skew of 0.3. On the other hand, 04-05 had an average T_p of 8.87 s with a standard deviation of 3.05 and skew of -0.02. Almost half of the measurements fell between 8 and 9 seconds for these two years as shown in Figure 2.5., indicating useful 'typical' values for this region.

Finally the third panel of Figures 2.2 and 2.3 presents mean wave direction, which appears to be very stable for both years. For 02-03 the average θ_{mean} was 75° with a standard deviation of 28° and skew of 4.4, whereas for 04-05 the average θ_{mean} of 78° with a standard deviation of 30° and skew of 3.9. Slightly less than half of the waves during these two years are shore normal (~73° ±4°). Comparing the results from these years reveals that based on the distributions of θ_{mean}, waves approach the nearshore from the southeast more often than from the northeast, regardless of the storm/wave activity. Figure 2.6 presents histograms of θ_{mean} for these two periods.

(a)

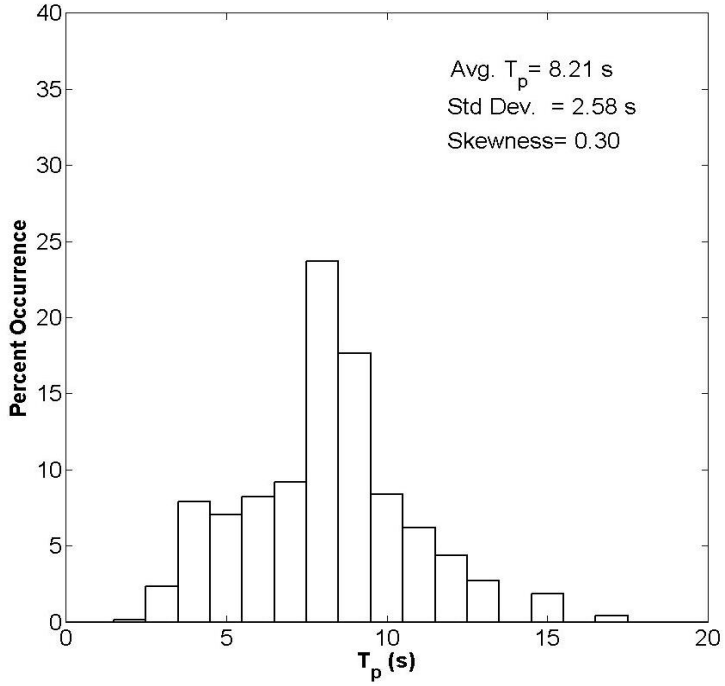

(b)

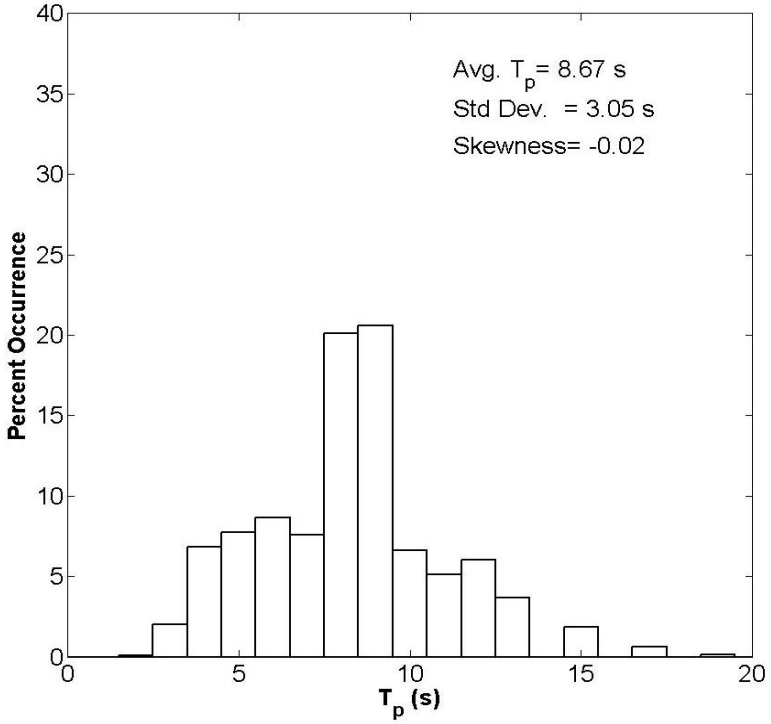

Figure 2.5: Histogram of T_p a) 2002-2003, b) 2004-2005.

(a)

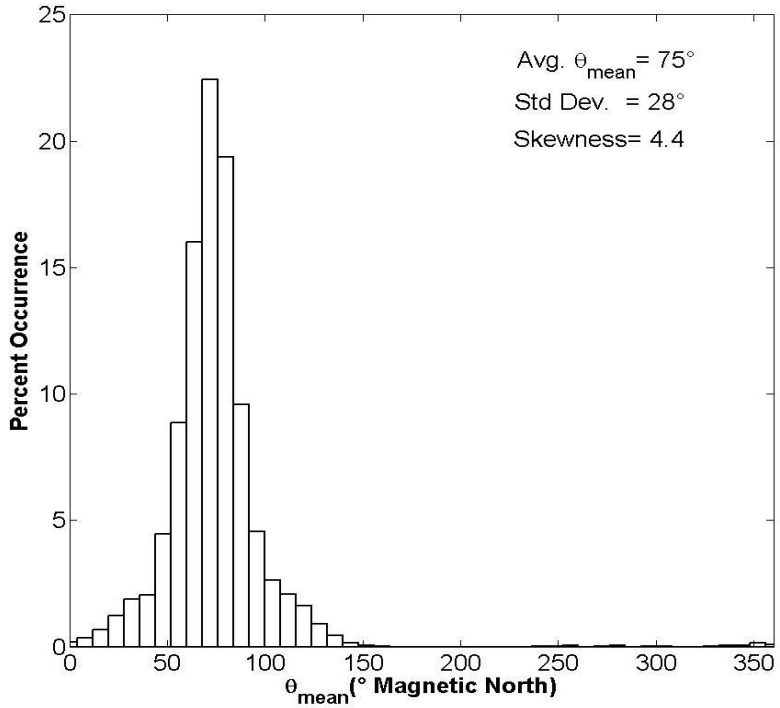

(b)

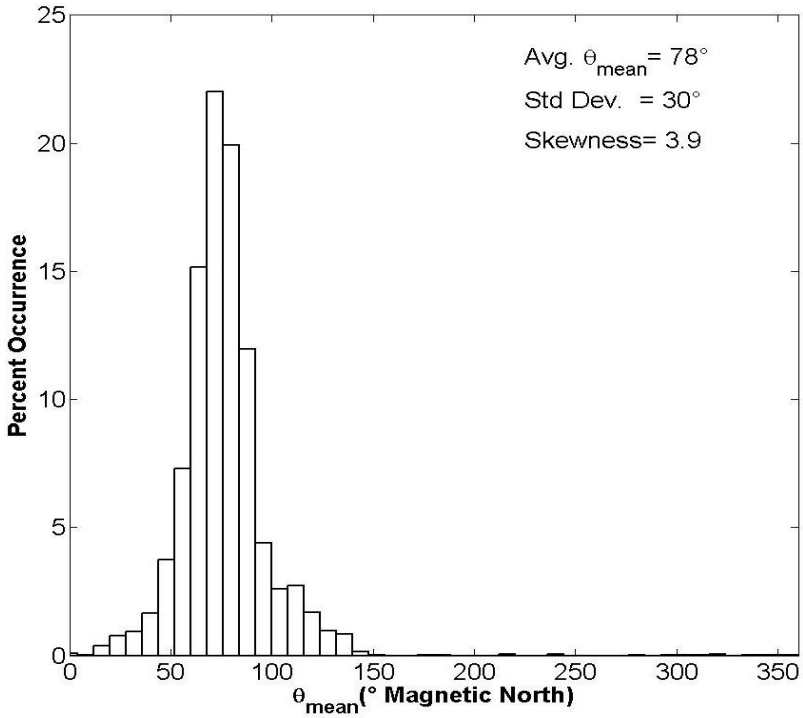

Figure 2.6: Histogram of θ_{mean} a) 2002-2003, b) 2004-2005.

2.2 Analysis of Averaged Spectra

From the FCFP record, 39,759 fully 2D (i.e. frequency-direction) spectra are available. Figure 2.7 presents the average of these spectra as both a contour plot and a mesh plot. The contour plot indicates that the peak of the average of the 2D spectrum occurs at a frequency of 0.125 Hz (i.e. period T=8 s) and at a direction of ~74° (direction from which waves approach, referenced to magnetic north), indicating a neutral long-term net forcing The average energy density is distributed almost symmetrically between 40° and 110°.

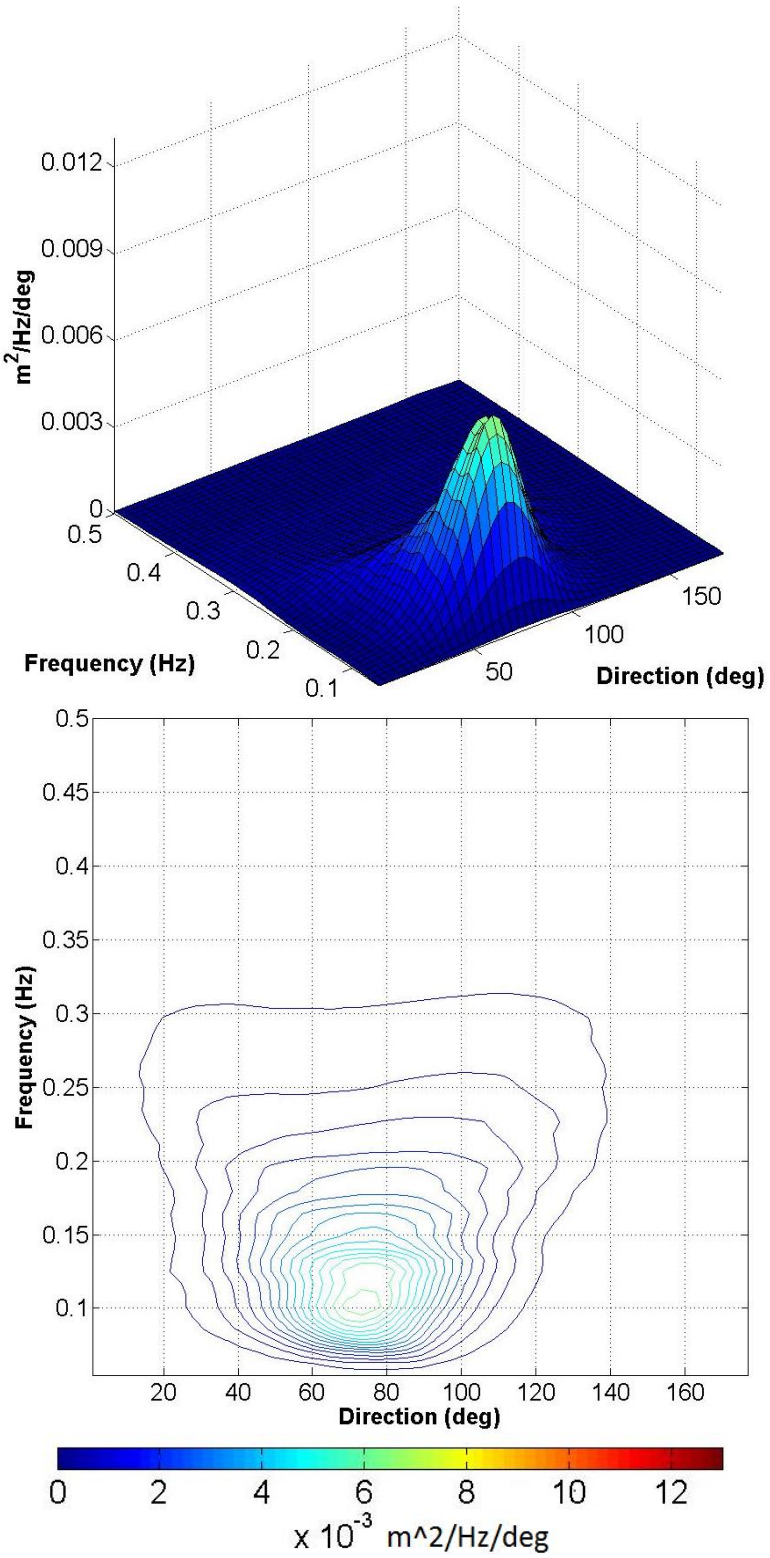

Figure 2.7: Average of all 39,759 directional spectra from the Spessard record.

For further analysis of the directional characteristics, the spectra can be divided into three directional windows, ‘shore-normal’, ‘northeast’, and ‘southeast’. Based on directions measured by the ADCP at Spessard, the shore-normal direction, relative to magnetic north, was estimated by Kennedy and Dean (2005) to be 73°± 4°. Therefore, a measured spectrum with a peak in its directional distribution within this window is categorized as shore-normal. A peak at a value less than 69° is categorized as northeast, and a peak at a value greater than 77° is categorized as southeast.

Figure 2.8 presents the average spectrum of the 8,151 directional spectra that fell within the shore-normal window. Strong symmetry can be observed with only slightly more energy from the southeast. The peak frequency of the average is around 0.1 Hz. Figure 2.9 presents the average of the 20,892 directional spectra that fall within the southeast window. The peak frequency of the average is at 0.125 Hz. The peak direction for the southeast window is at ~81°. Figure 2.10 presents the average of the remaining 10,716 directional spectra that fall within the northeast window. The peak frequency of the average is at 0.110 Hz, but a secondary peak is present at 0.125 Hz. The peak direction for the northeast window is at ~61°. Figures 2.11 and 2.12 present the direction distribution and frequency spectra plots for the entire record, respectively.

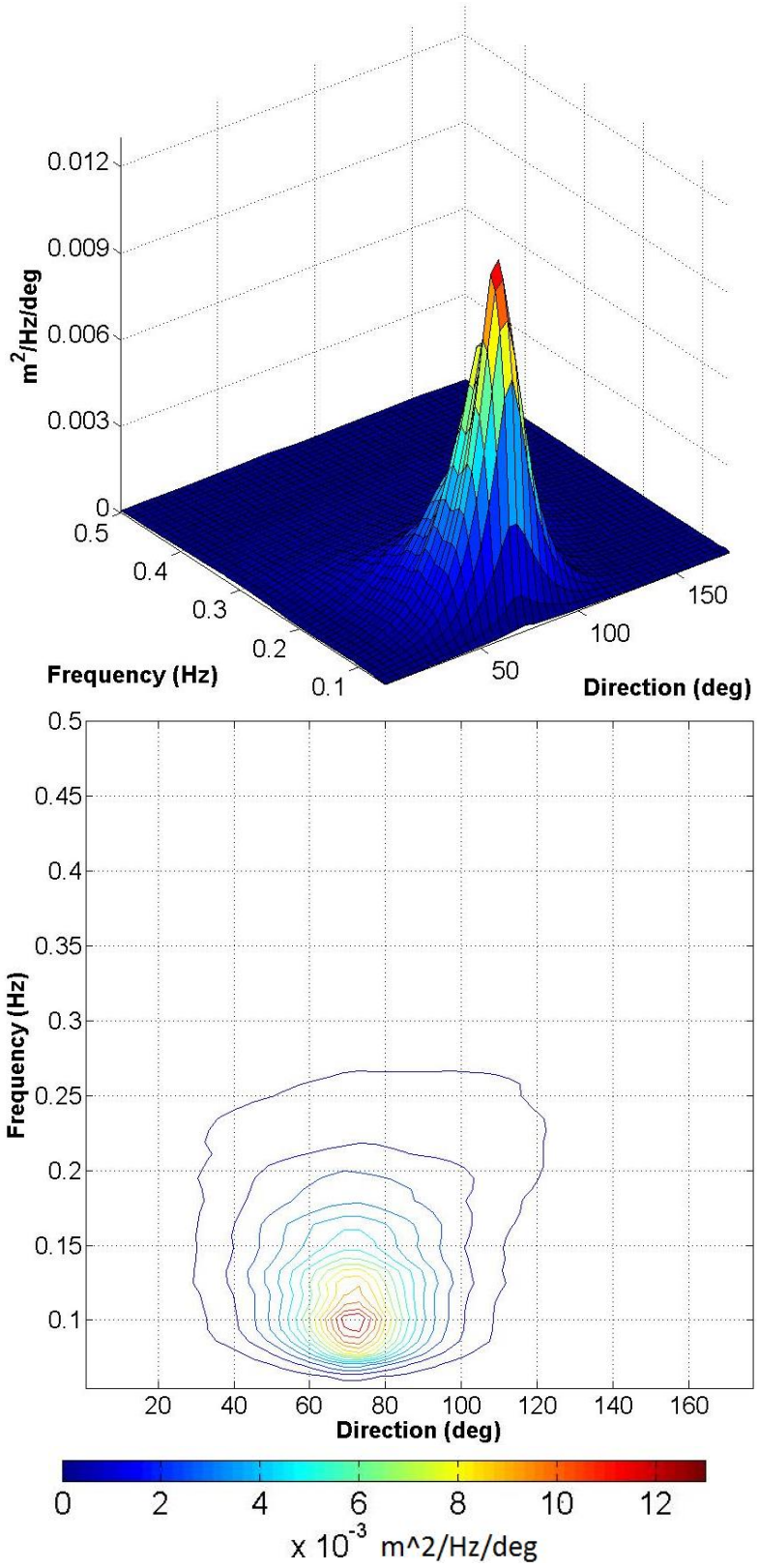

Figure 2.8: Average of 8,151 directional spectra from the shore-normal window.

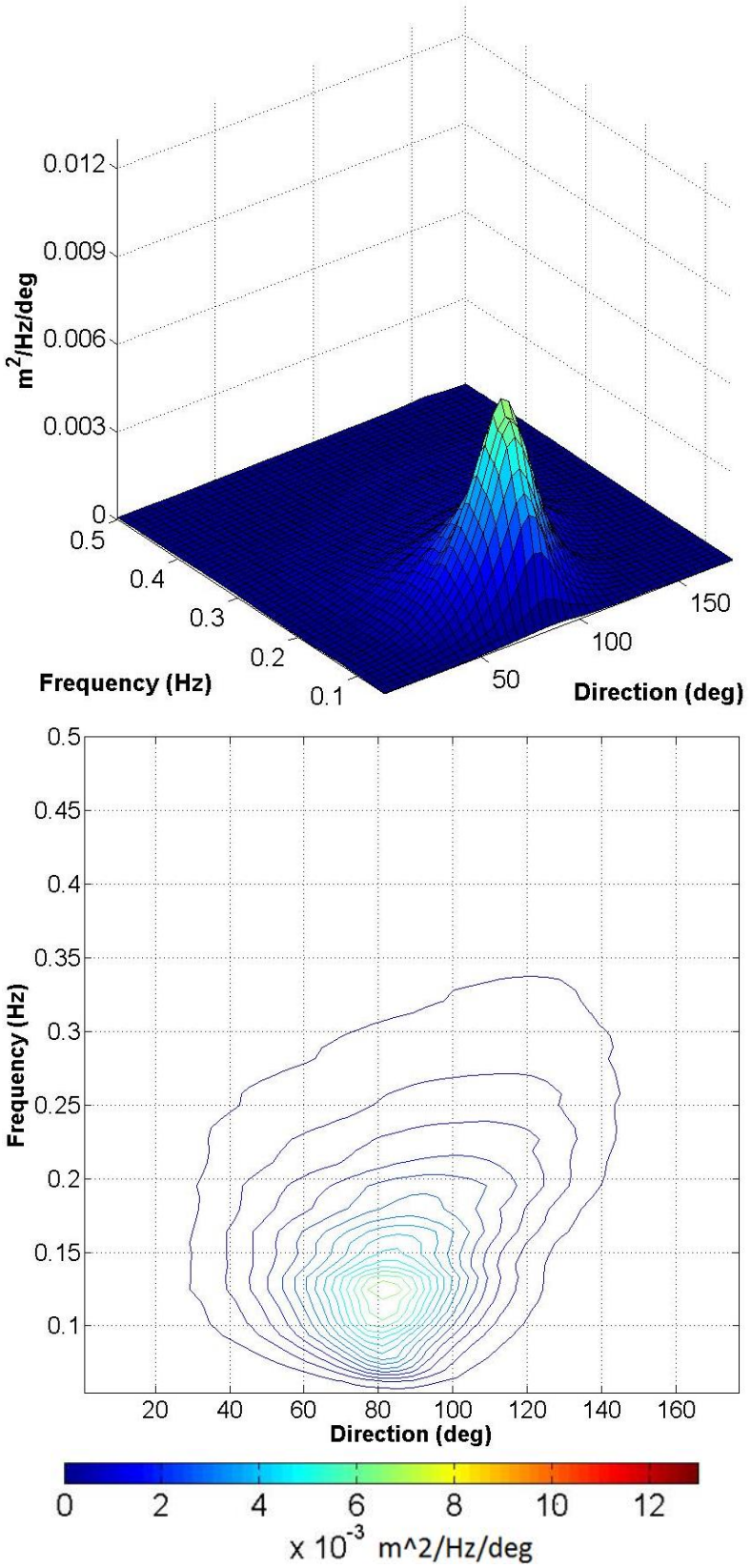

Figure 2.9: Average of 20,892 directional spectra from the southeast window.

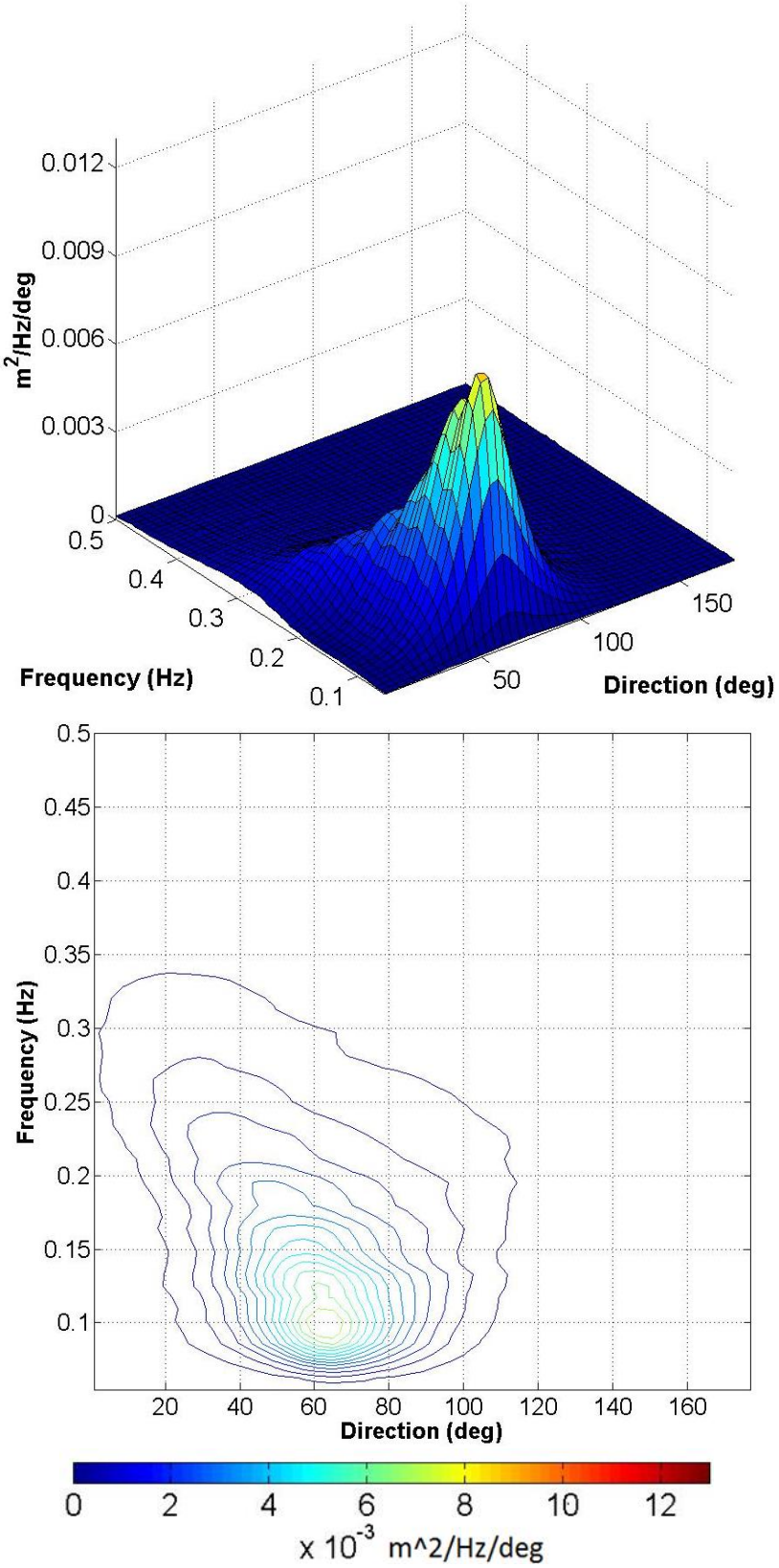

Figure 2.10: Average of 10,716 directional spectra from the northeast window.

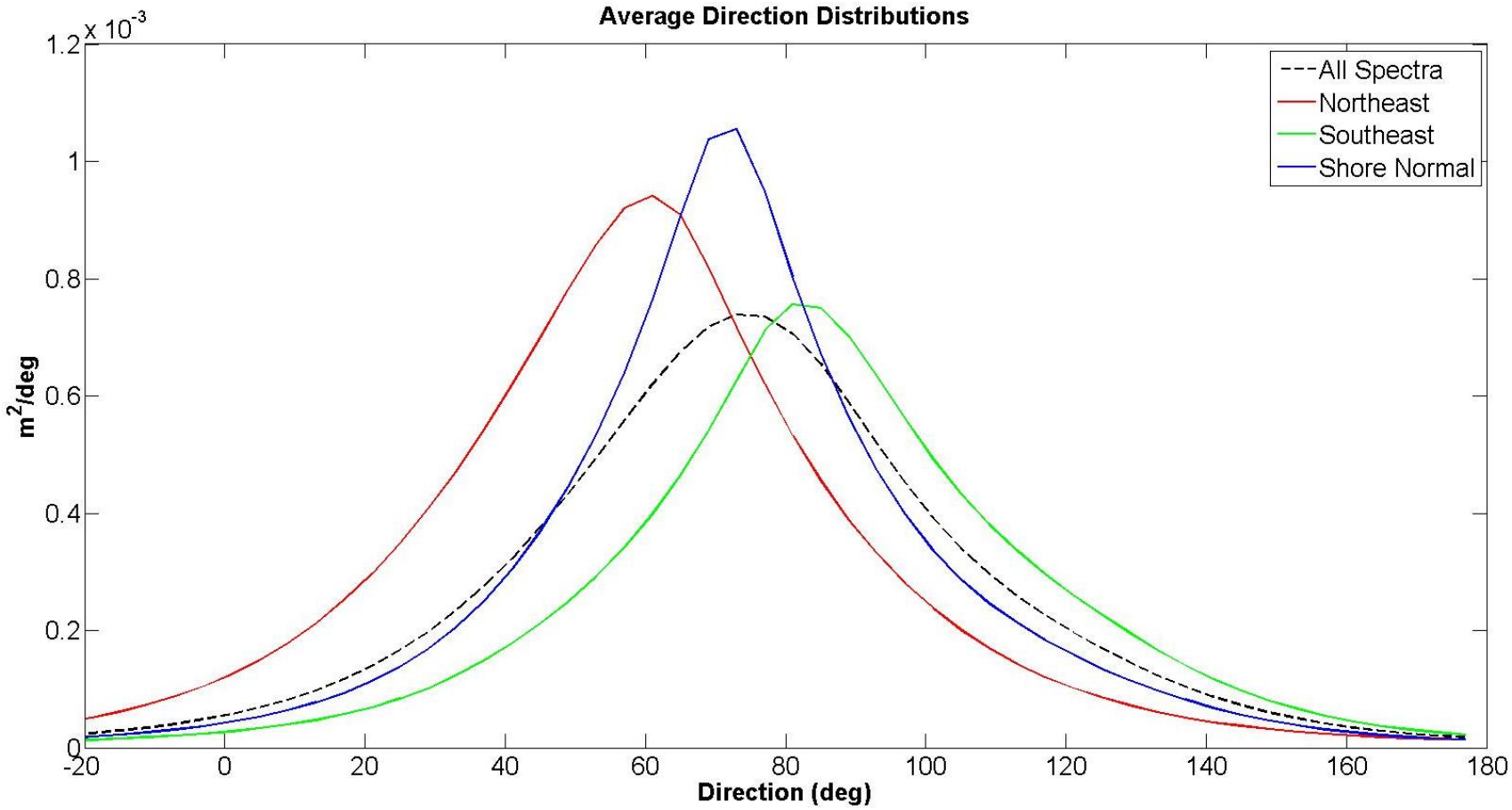

Figure 2.11: Average direction distributions for the Spessard record.

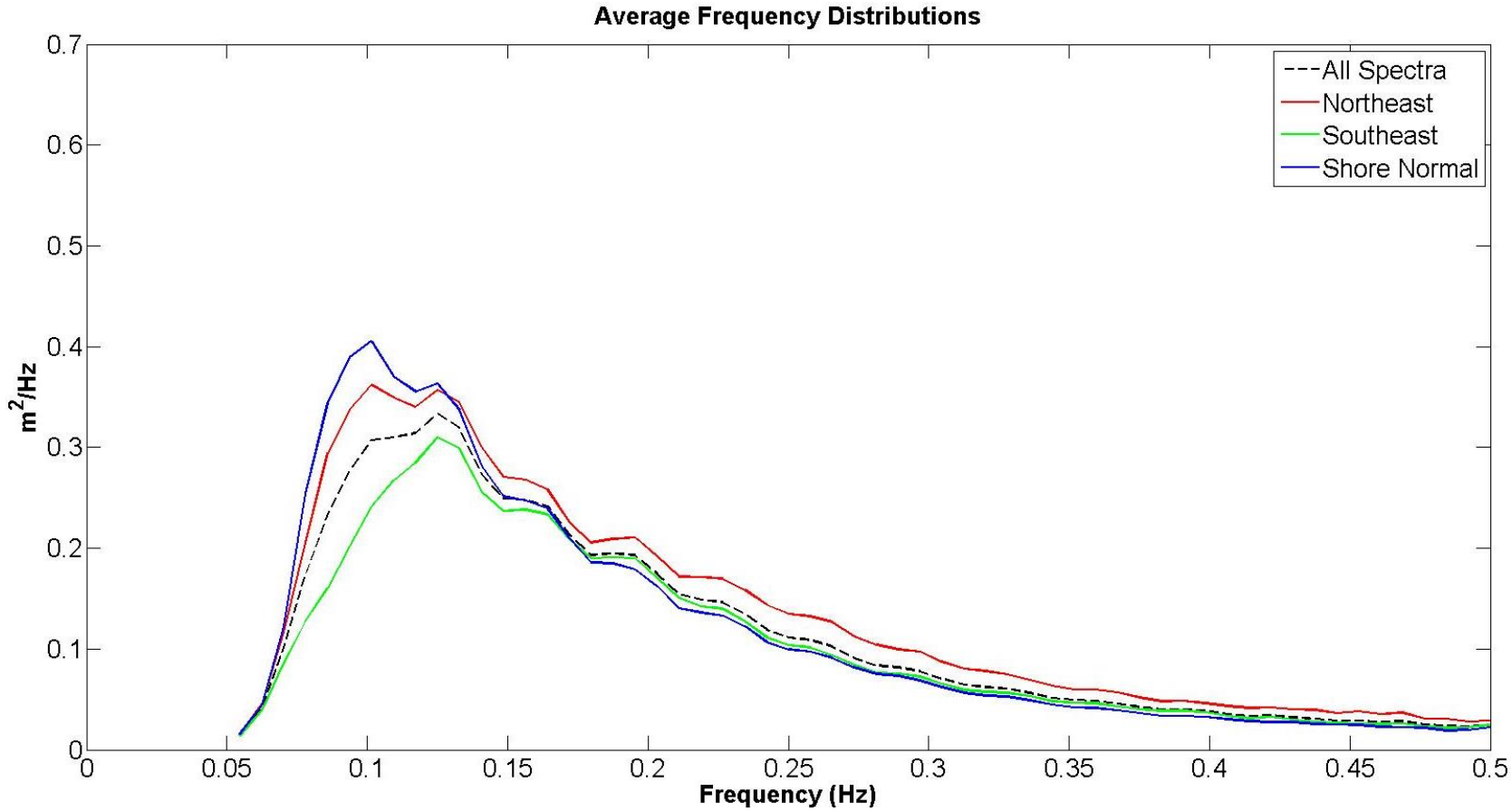

Figure 2.12: Averaged frequency spectra for the Spessard record

Useful information can be extracted by contrasting the results from the three windows. Energy can be calculated by integrating the average spectrum across frequency and direction. Then equation 2.2 can be used to calculate the average H_{mo}. Table 2.2 presents the H_{mo} averages for every window. The northeast window was the most energetic, with an average H_{mo} of 0.87 m.. The shore-normal window was the second most energetic, with an average energy of 0.83 m followed by the southeast window, with an average energy of 0.78 m. Finally, waves coming from the southeast window arrived more often than from the other two windows combined. That is, about 53% of all the waves came from the southeast.

$$H_{mo} = 4\sqrt{E} \tag{2.2}$$

Table 2.2: Average H_{mo} Calculated for each Window

Average H_{mo} (m)			
Window	**02-03 Period**	**04-05 Period**	**All Data**
Southeast	0.64	0.79	0.78
Northeast	0.70	1.01	0.87
Shore-Normal	0.73	0.87	0.83
All Windows	0.69	0.89	0.83

As one means of further analyzing the wave climate at Spessard during 02-03 and 04-05, Figure 2.13 presents the average of 3,721 spectra for 02-03 and 3,967 spectra for 04-05, as contour plots. The peak frequency for 02-03 is 0.125 Hz and the peak direction is at~73°. For 04-05 the peak frequency occurs at 0.09 Hz and the peak direction is at ~73°. Both years have the average

energy distributed symmetrically between 40° and 110°. The total average energy (H_{mo}) for 02-03 was 0.69 m while for 04-05 it was 0.89 m.

It can be noted from Figure 2.14 that during 02-03 all three windows were less energetic than 04-05. During 04-05 shore-normal (avg. H_{mo} = 0.87 m) and northeast (avg. H_{mo} = 1.01 m) waves were very energetic, increasing the total average energy for this period. Table 2.2 presents the average energy from each window. Both years appear to have neutral forcing because of the high percentage of waves approaching from the southeast, 46% and 52% for 02-03 and 04-05, respectively.

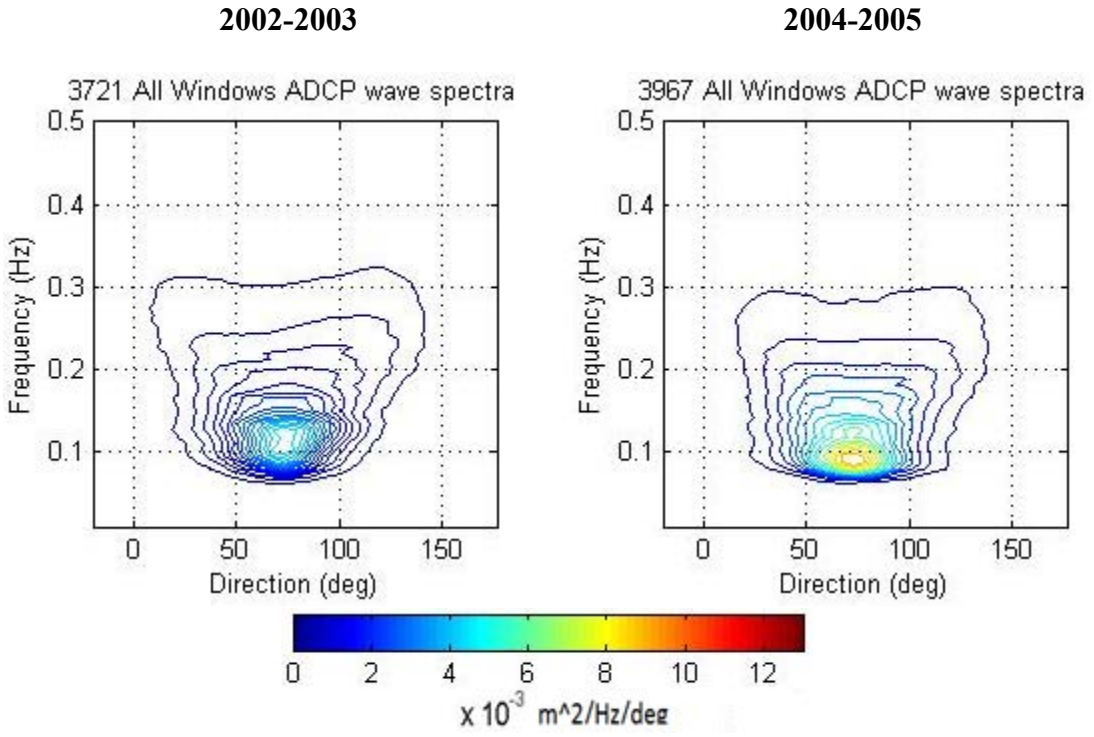

Figure 2.13: Average ADCP Spectra for all Windows.

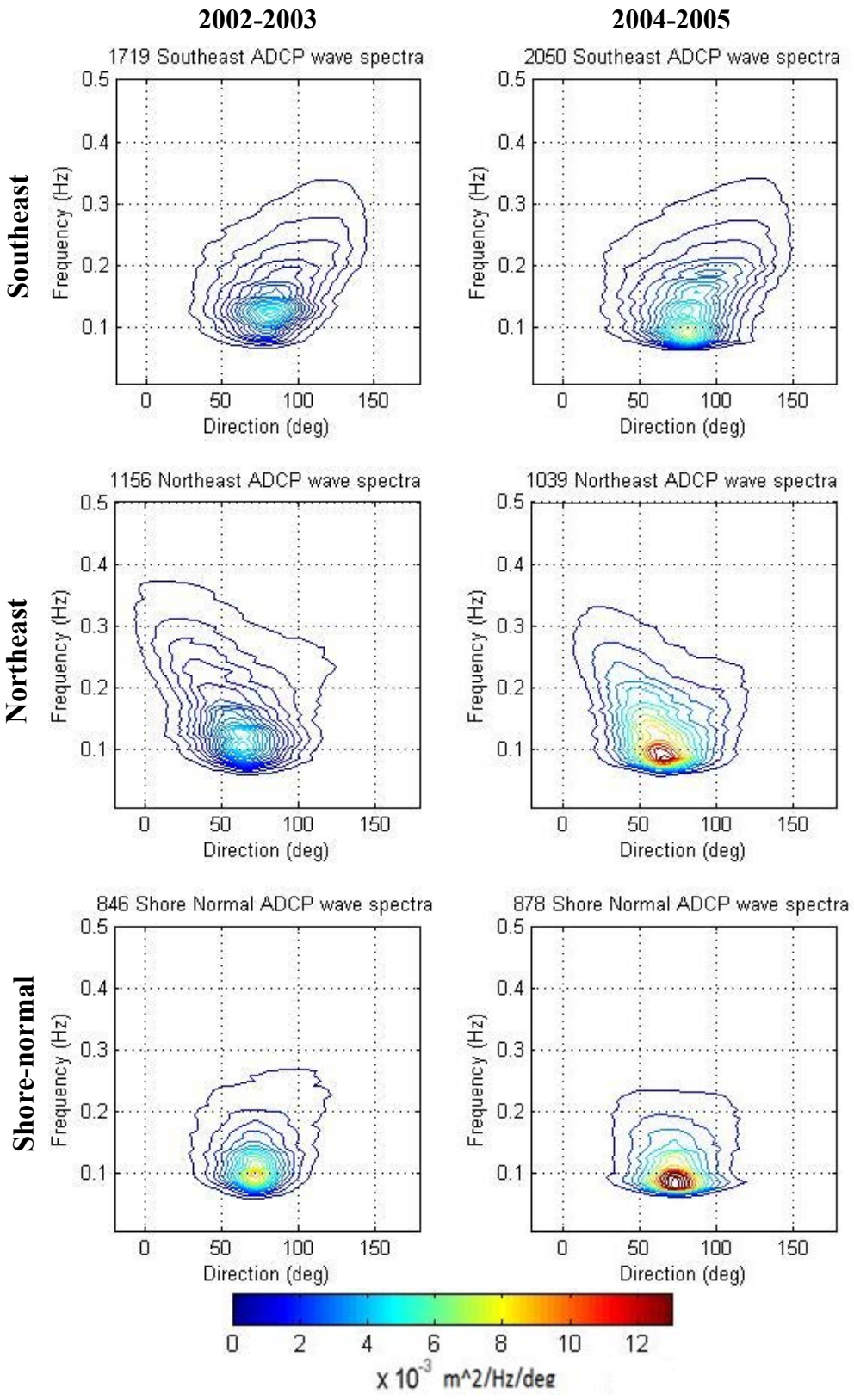

Figure 2.14: Average ADCP Spectra divided into windows.

2.3 Discussion

The wave climate was analyzed based on wave parameters and the average spectra. High yearly and seasonal variability were found in the data. The expectation was to find a north to south forcing during 04-05, since it was a very active year; but results indicate that there was a neutral net longshore forcing for both of the years compared (02-03 and 04-05). The high percentages of southeast waves are the main factor contributing to a balance in the longshore forcing.

If only the averaged spectrum was considered, wave energy in this area is slightly dominated by southerly waves; the energy for the entire record is distributed almost symmetrically with the peak being at ~74° (73° being shore-normal). It was expected to find the peak at a direction less than 73° since all the inlets in this area indicate a strong north to south transport. Reconciling this with the fact that net longshore transport is known to be north to south will be addressed in Chapter 4.

To increase efficiency of wave energy collection devices in east Florida, the device must be at peak productivity when the waves are approaching from the northeast because the majority of the energy comes from the northeast (avg. H_{mo} = 0.87 m) and shore-normal (avg. H_{mo} = 0.83m) windows. But, even though waves coming from the southeast (avg. H_{mo} = 0.78 m) are less energetic, they arrive 52% more often than the other two windows combined. Considerable amounts of energy can also be extracted from the southeast window.

Chapter 3:

PROBABILITY MODELING OF THE WAVE DATA

To characterize the overall wave climate at the Spessard station, the development of probability models is beneficial. This chapter develops probability models for energy-based significant wave height (H_{mo}), mean period (T_{mean}) and peak period (T_p) utilizing the shifted gamma, shifted lognormal and Gaussian distributions. These models are used because of their success in previous studies including Lawson and Abernethy (1975), Ochi (1978), Rossouw (1988) and Leyden and Dally (1996). Computations of the root mean square error (ε_{rms}) will be used to compare the accuracies of the different models. The following equation calculates ε_{rms} in terms of percentage:

$$\varepsilon_{rms} = \sqrt{\frac{\sum_1^N (X_{Model} - X_{Data})^2}{\sum_1^N (X_{Data})^2}} \tag{3.1}$$

3.1 Probabilistic Models

3.1.1 Shifted Gamma Distribution

The gamma distribution has been commonly used in civil engineering applications (Benjamin & Cornell, 1970, pp. 482-483). Leyden and Dally (1996) found success with the shifted gamma

distribution in modeling eight years of wave measurements from the U.S Army Corps of Engineers Field Research Facility in NC.

Although several probability distributions were considered, the present study found that the shifted gamma distribution provided the best representation of the H_{mo} dataset. For the random variable x, the shifted gamma distribution is given by

$$pdf(x) = \frac{\lambda}{\Gamma(k)}[\lambda(x-a)]^{k-1}e^{-\lambda(x-a)} \qquad x \geq a \qquad (3.2)$$

where k is a shape parameter, λ is a scaling parameter, a is a shifting parameter and Γ(k) is the gamma function defined by $\Gamma(k) = \int_0^\infty e^{-y}y^{k-1}dy$. To calculate the best-fit parameters, the method of moments was used. This method utilizes the mean ( ), the standard deviation (σ) and the skew (s) of the dataset to solve the following equations:

$$s = \frac{2}{\sqrt{k}} \qquad (2.3)$$

$$\sigma = \frac{\sqrt{k}}{\lambda} \qquad (3.4)$$

$$\bar{x} = a + \frac{k}{\lambda} \tag{3.5}$$

3.1.2 Shifted Lognormal Distribution

The Lognormal distribution has also been used within the civil engineering field (Benjamin & Cornell, 1970, pp. 483-486). Studies made by Lawson and Abernethy (1975) found that the lognormal distribution provided a good fit to significant wave height data from Botany Bay, Australia. Leyden (1997) found that the shifted lognormal distribution successfully represented the eight years of H_{mo} data from the FRF's linear array and an offshore buoy. The shifted lognormal distribution for the random variable x is given by

$$pdf(x) = \frac{1}{\sqrt{2\pi}\sigma_{lnY}(x-a)} exp\left\{-\frac{1}{2}\left[\frac{\ln(x-a) - m_{lnY}}{\sigma_{lnY}}\right]^2\right\} \qquad x \geq a \tag{3.6}$$

where $Y = x - a$, and m_{lnY} is the mean of $ln\, Y$ and σ_{lnY} is the standard deviation of $ln\, Y$. Once again the method of moments was used to determine the best-fit parameters. The following equations are solved using the first three moments of the data (, σ, and s):

$$s = 3\frac{\sigma}{m_Y} + \left(\frac{\sigma}{m_Y}\right)^3 \tag{3.7}$$

$$a = \bar{x} - m_Y \tag{3.8}$$

By solving the following equation the coefficients σ_{lnY} and m_{lnY} can be calculated as

$$V_Y = \frac{\sigma}{m_Y} \tag{3.9}$$

$$\sigma_{lnY}^2 = \ln(V_Y^2 + 1) \tag{3.10}$$

$$m_{lnY} = \ln m_Y - \frac{1}{2}\sigma_{lnY}^2 \tag{3.11}$$

3.1.3 Gaussian Distribution

Wave period is a very important parameter to consider when, e.g., designing a coastal structure. Many numerical models require wave height, wave period and wave direction as an input. After testing the shifted gamma, shifted lognormal and Gaussian distributions for both mean and peak wave period, the probability density function that found the most success in representing the

mean wave period is the Gaussian. The Gaussian distribution is one of the most commonly used models in applied probability theory (Benjamin & Cornell, 1970, pp. 249-261). The Gaussian distribution for the random variable x is given by

$$pdf(x) = \frac{1}{\sigma\sqrt{2\pi}} exp - \frac{(x - \bar{x})^2}{2\sigma^2} \tag{3.12}$$

3.2 Statistics and Models of Energy-Based Significant Wave Height for the Spessard Data

Figure 3.1 presents the histogram of H_{mo} for the entire record at Spessard. The dataset has an average H_{mo} of 0.82 m, a standard deviation of 0.44 m, and skew of 1.32. The maximum significant wave height observed in the record is 4.1 m, occurring during Hurricane Jeanne as mentioned previously.

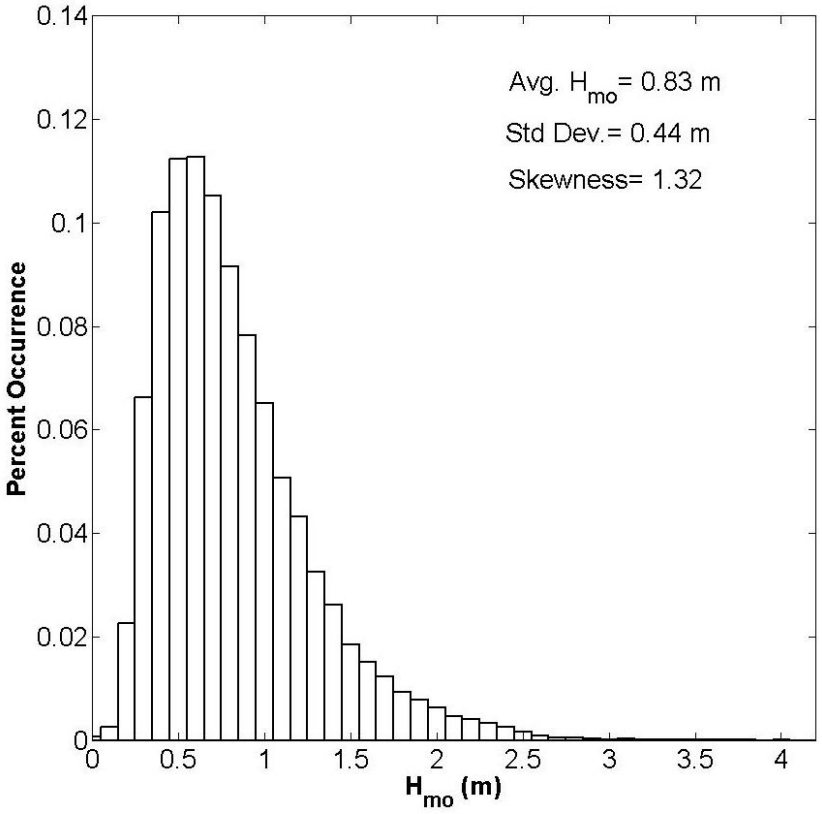

Figure 3.1: Histogram of energy-based significant wave height (H_{mo}) from Spessard.

Figure 3.2 shows the capability of the shifted gamma and shifted lognormal distributions to model the Spessard H_{mo} data. Both models provide a good fit for the data, but they underestimating the peak of the data slightly. The shifted gamma distribution underestimates the peak of the histogram by 1.36%, while the shifted lognormal by 1.86%. The root mean square error (ε_{rms}) for the shifted gamma model is 3.00%, whereas for the shifted lognormal model the root means square error is 7.84%. Table 3.1 shows the root mean square error and the best-fit parameters for both distributions. Overall, the shifted lognormal model is slightly superior to the shifted lognormal, given the fact that it goes to zero at 0.1 m. The shifted gamma model diverged from the data both near the peak of the histogram and with wave heights of less than 0.2 m.

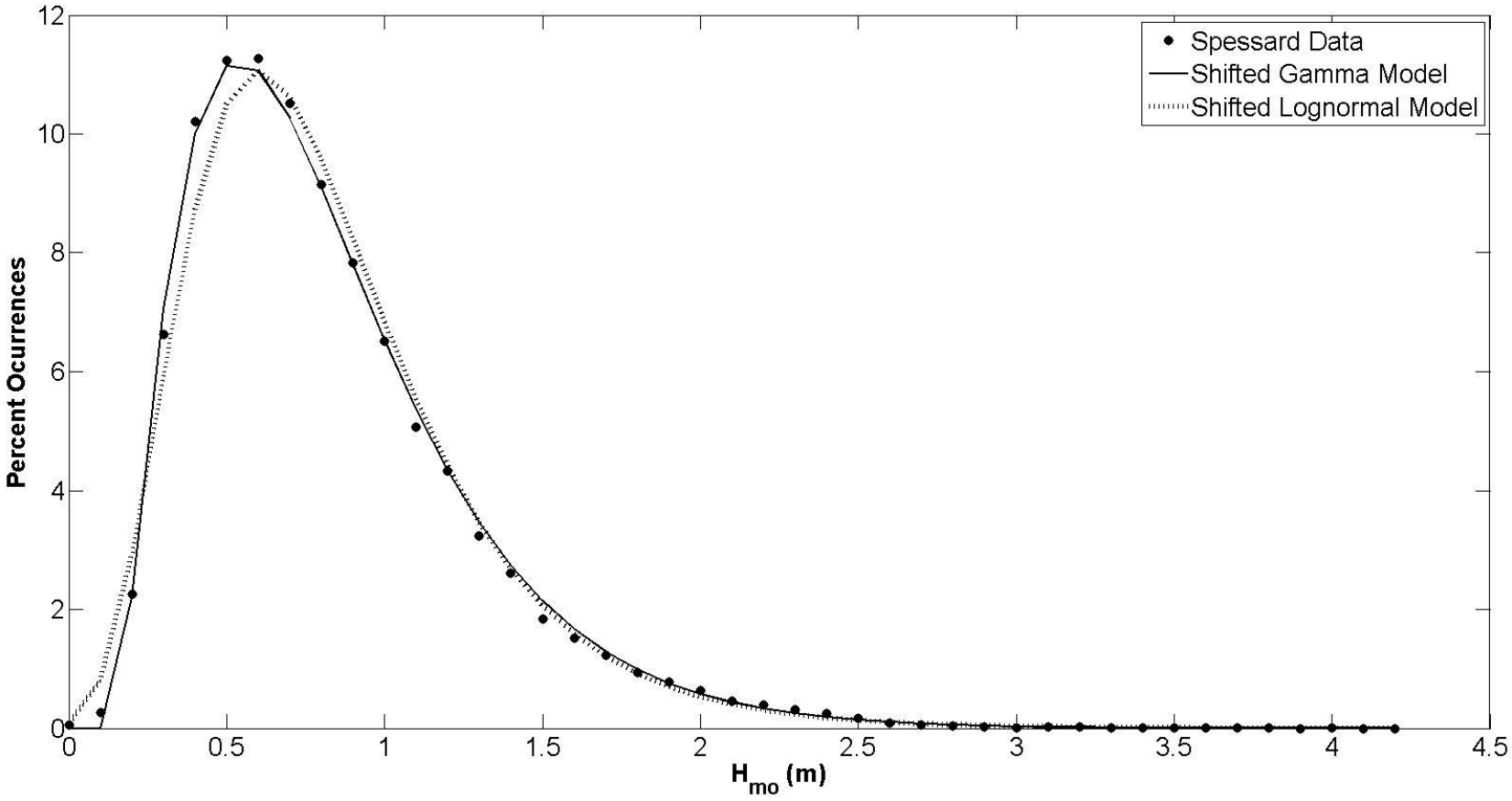

Figure 3.2: Comparison of the shifted gamma and shifted lognormal models to the H_{mo} data.

Table 3.1: Best-fit model parameters and root mean square errors (ε_{rms}) for the H_{mo} data

	Shifted Gamma Model				Shifted Lognormal Model			
	a (m)	k	$\lambda(m^{-1})$	$\varepsilon_{rms\ (\%)}$	a (m)	σ_{lnY}	m_{lnY}	$\varepsilon_{rms\ (\%)}$
Spessard H_{mo} Data	0.171	2.31	3.46	3.00	-0.236	0.398	-0.0198	7.84

3.3 Statistics and Model of Mean Period (T_m) for the Spessard Data

The histogram of T_{mean} was best represented by the lognormal distribution. The shifted gamma could not be used because a bin size greater than 2.5 s had to be used (see equation 3.2, a= 2.3). Figure 3.3 presents the histogram of T_{mean} for the entire record. The dataset has an average T_{mean} of 5.46 s, with a standard deviation of 1.70 s and skew of 1.01. Table 3.2 presents the best-fit parameters and root mean square error for the shifted lognormal distribution.

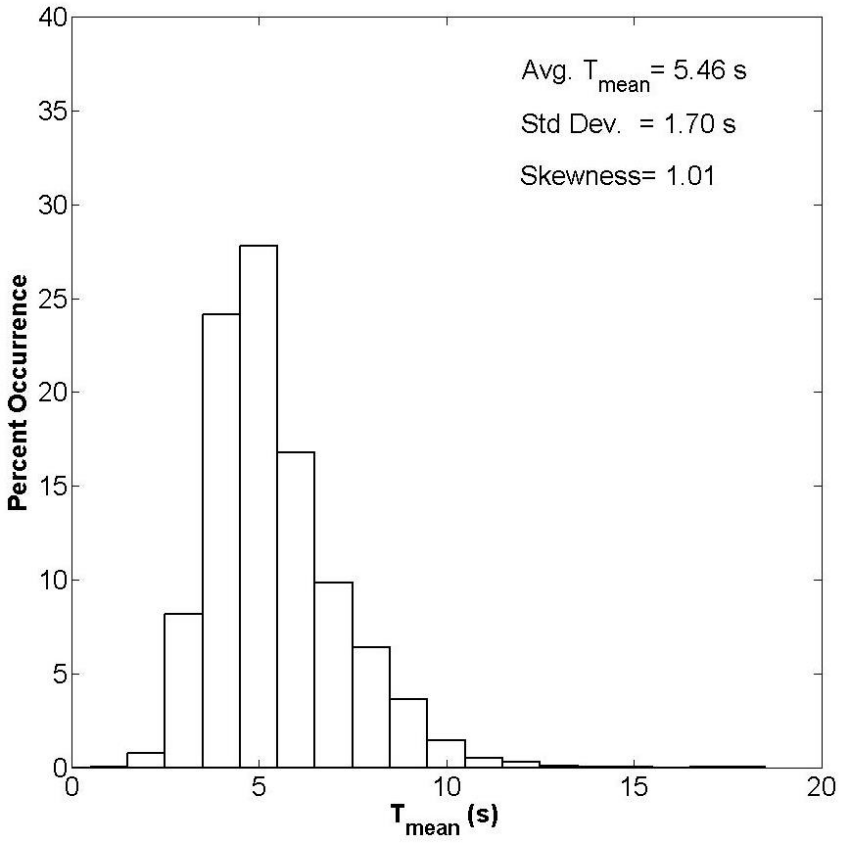

Figure 3.3: Histogram of mean period (T_{mean}).

Table 3.2: Best-fit model parameters and root mean square error (ε_{rms}) for the T_{mean} data

	Shifted Lognormal Model			
	a(m)	σ	m_{lnY}	ε_{rms} (%)
Spessard T_{mean} Data	0.232	0.316	1.60	9.34

Figure 3.4 shows the capability of the shifted lognormal distribution to model the Spessard T_{mean} data. Overall, the model represents the data fairly well, but deviates with wave periods between 4-7 seconds and under-estimates the peak of the distribution. The root mean square error for the shifted lognormal model is 9.34%.

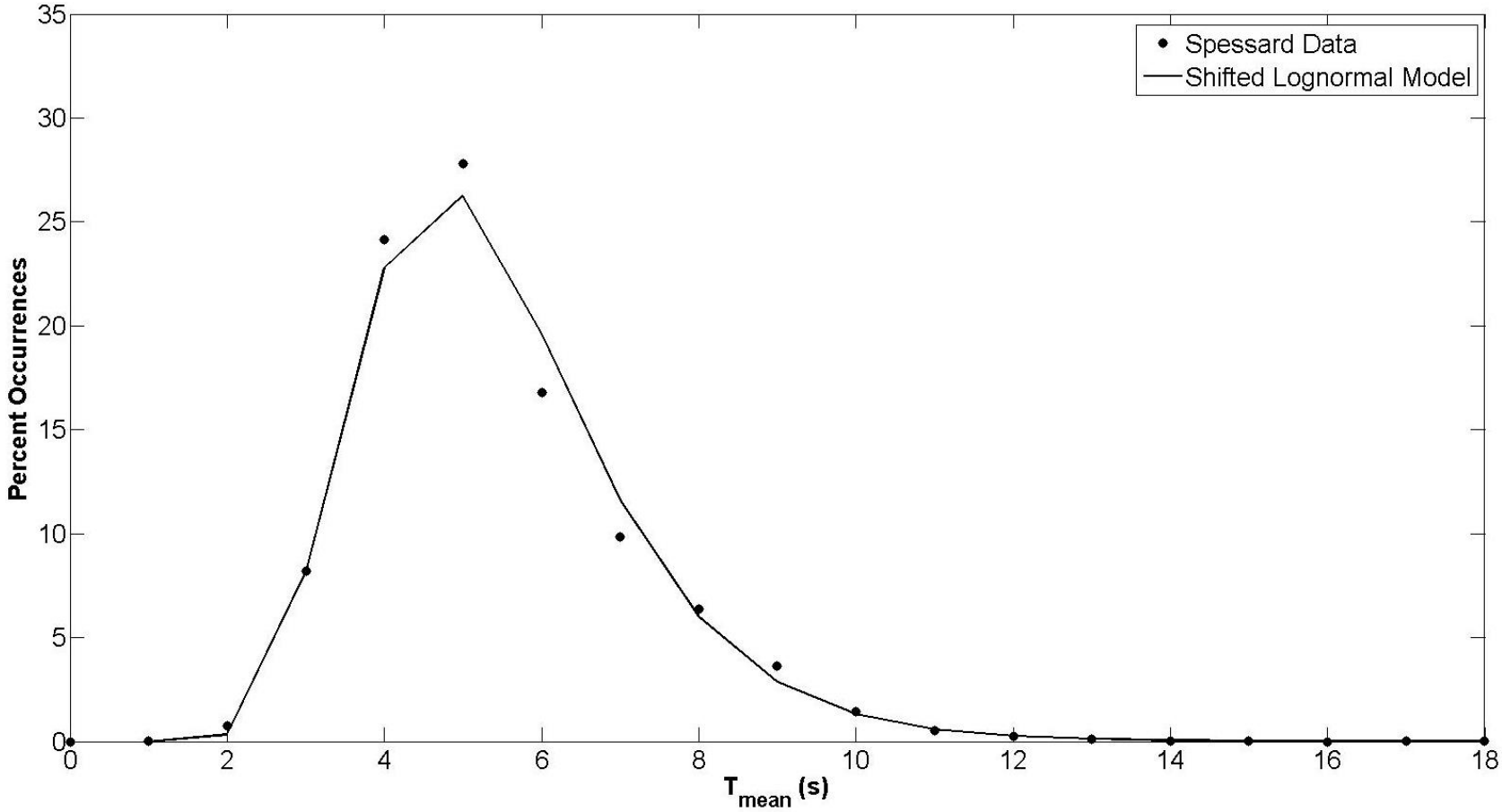

Figure 3.4: Comparison of the shifted lognormal model to the T_{mean} data.

3.4 Statistics and Model of Peak Period (T_p) for the Spessard Data

Before attempting to model the distribution of T_p, the bin size had to be doubled (from 1 s to 2 s) to remove the irregular behavior of the histogram. Figure 3.5 presents the histogram of T_p for the entire record. Note the almost symmetric structure in the distribution. For this reason, the Gaussian distribution was selected for modeling. The dataset has an average T_p of 8.24 sec, with a standard deviation of 2.82 sec and skew of 0.18. Table 3.3 presents the best-fit parameters and root mean square error for the Gaussian distribution.

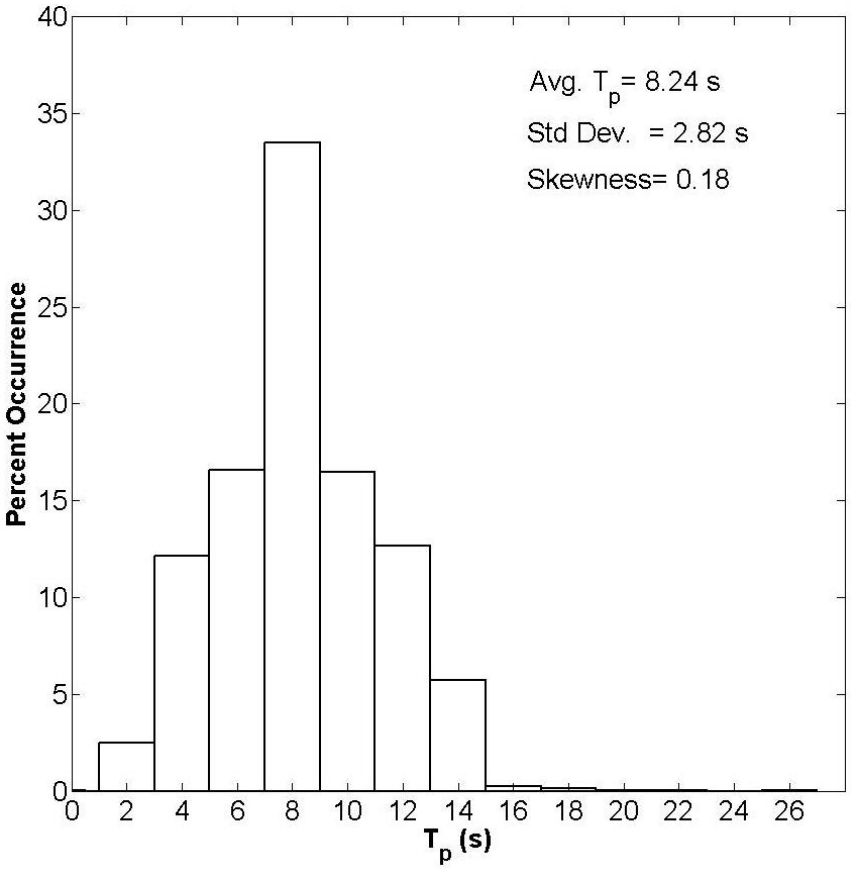

Figure 3.5: Histogram of peak period (T_p).

Table 3.3: Best-fit model parameters and root mean square error (ε_{rms}) for the T_p data

	Gaussian Model		
	$\bar{x}$ (m)	σ (m)	$\varepsilon_{rms\ (\%)}$
Spessard T_{peak} Data	8.24	2.82	22.9

Figure 3.6 presents a comparison of the Gaussian distribution model to the Spessard T_p data. Overall, the model captures the shape of the distribution but misses the peak. Consequently, the root mean square error for this model is 22.9%.

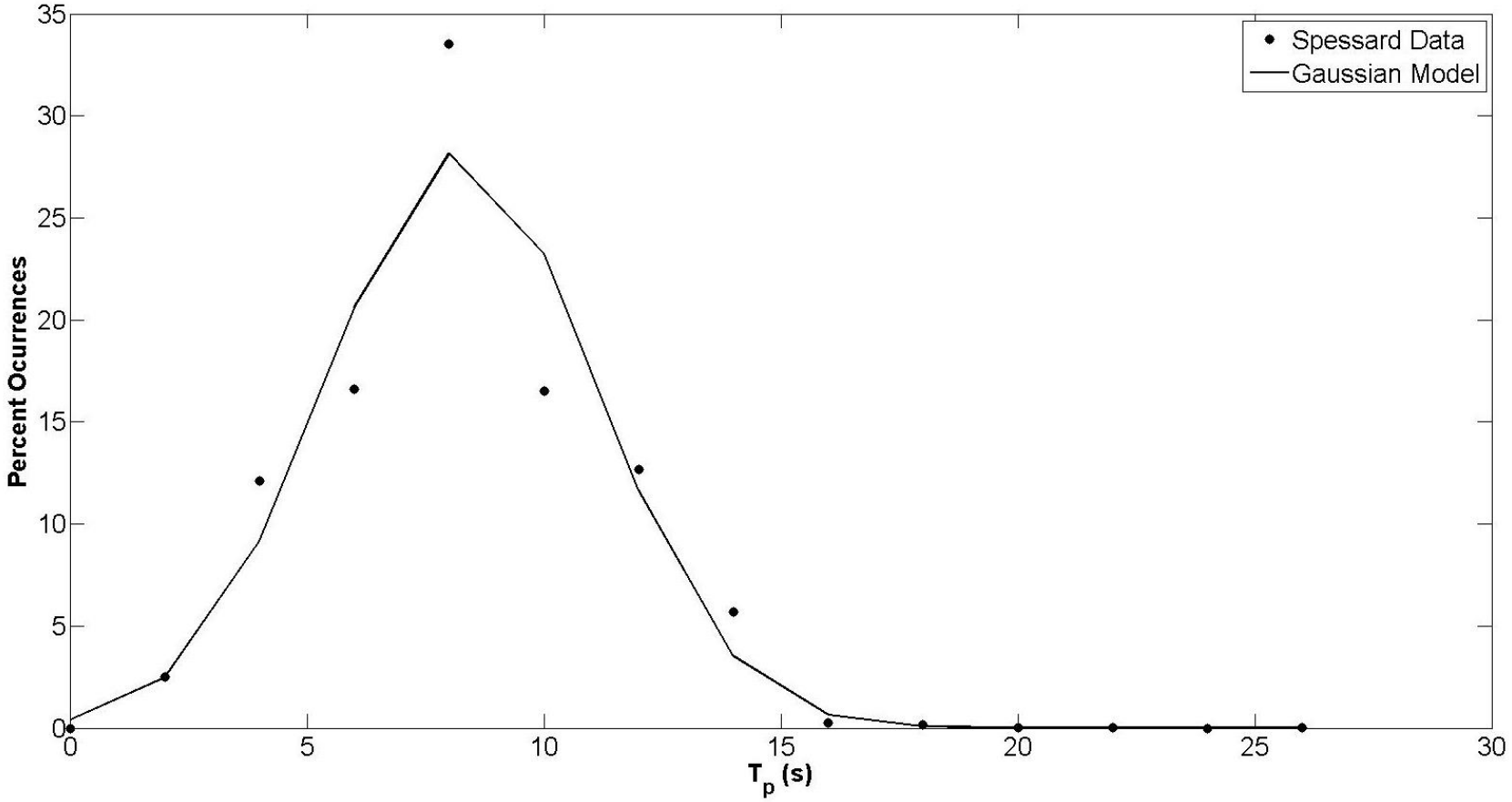

Figure 3.6: Comparison of the Gaussian model to the T_p data.

3.5 Discussion

Both the shifted gamma and shifted lognormal distributions had success in modeling the Spessard significant wave height data, with the shifted gamma being slightly better. Although both models missed the peak of the data, the root mean square error for both distributions, shifted gamma distribution (3.00%) and shifted lognormal (7.84%), was relatively small.

The shifted lognormal distribution had some success in representing the T_{mean} data. However, the model did not fit the middle of the histogram well, and perhaps another means of selecting the parameters, such as the maximum likelihood method, would improve agreement.. The root mean square error for this distribution was 9.34%. The shifted lognormal distribution can be used to model long-term mean period datasets.

Finally, a coarse bin width was important to for the development of the T_p histogram. The Gaussian distribution had only marginal success modeling the T_p histogram, notably underestimating the peak. The root mean square error was found to be 22.9% for this distribution. One issue is that the ADCP reports its measurements in terms of peak frequency rather than peak period, and it may be better to model the peak frequency and then invert the result by transformation of random variables to model T_p.

Chapter 4:

RADIATION STRESS TENSOR CROSS-COMPONENT Sxy

As mentioned previously, the Spessard dataset is very valuable because it is a relatively long record of high-resolution directional spectra measured in the nearshore. This presents an opportunity to compute the Radiation Stress Tensor cross-component S_{xy} using the nearshore spectra with high directional resolution, in contrast to using bulk parameters and directional estimates as in common practice in coastal engineering. This parameter is important because it provides an indication of the forcing of the longshore current due to obliquely incident waves. This chapter presents and compares the results of integrating S_{xy} from the fully directional spectrum versus a parameter-based computation of S_{xy}. Furthermore, the variability of S_{xy} is analyzed on a yearly and seasonal basis by presenting yearly averages and time series plots. This chapter will also use the Spessard dataset to establish long-term estimates of the radiation stress climate for the east coast of Florida by seeking patterns in the behavior of S_{xy}. Finally, the importance of long-term datasets is going to be established.

4.1 Radiation Stress Estimates: Integrated S_{xy} vs Parameter-Based S_{xy}

On an open coast, the radiation stress component S_{xy} is one of the two forces responsible for driving longshore currents in the surf zone (Longuet-Higgins and Stewart, 1964), the other being the local wind stress. For random waves, S_{xy} can be computed using either 1) an integration of

the complete, directional spectrum, or 2) computation using only spectral parameters. Battjes (1972) showed that, according to linear wave theory, S_{xy} can be computed from the integral:

$$S_{xy} = \int_0^{\infty} \int_{-\pi}^{\pi} E(f,\theta) \frac{c_g(f)}{c(f)} \sin\theta \cos\theta \, d\theta \, df \tag{4.1}$$

where $E(f,\theta)$ is the frequency-direction energy spectrum, $c_g(f)$ and $c(f)$ are the frequency dependent group and phase velocities, respectively. However, it is common practice in coastal engineering to approximate the value of S_{xy} by the use of spectral parameters as show in the following equation

$$S_{xy} = \frac{1}{16} \rho \, g \, H_{mo}^2 \frac{c_g(f_p)}{c(f_p)} \sin\bar{\theta} \, \cos\bar{\theta} \tag{4.2}$$

in which f_p is the peak spectral frequency, and $\bar{\theta}$ is the mean direction. The coordinate system for making the S_{xy} estimates is rotated and aligned to the shoreline orientation at Spessard. Positive values of S_{xy} indicate north-to-south longshore forcing, while negative values indicate south to north longshore forcing.

Figure 4.1 presents a time series of S_{xy} estimates for the entire record using both equations. Figure 4.2 presents the results from Figure 4.1 in a scatter plot, showing that the integrated S_{xy} is in general only 42% of the parameter-based estimate. The correlation between these methods was 0.73. The parameter-based approximation over-predicts the value of S_{xy} because all energy is assigned to a single direction (Ruessink et al., 2001). Ruessink (2001) found the over-prediction to be 60% by using data from a linear array of pressure transducers, at Duck FRF. Consequently, this indicates the importance of using high-resolution, fully directional spectra in coastal engineering applications including radiation stress computations and longshore currents estimates.

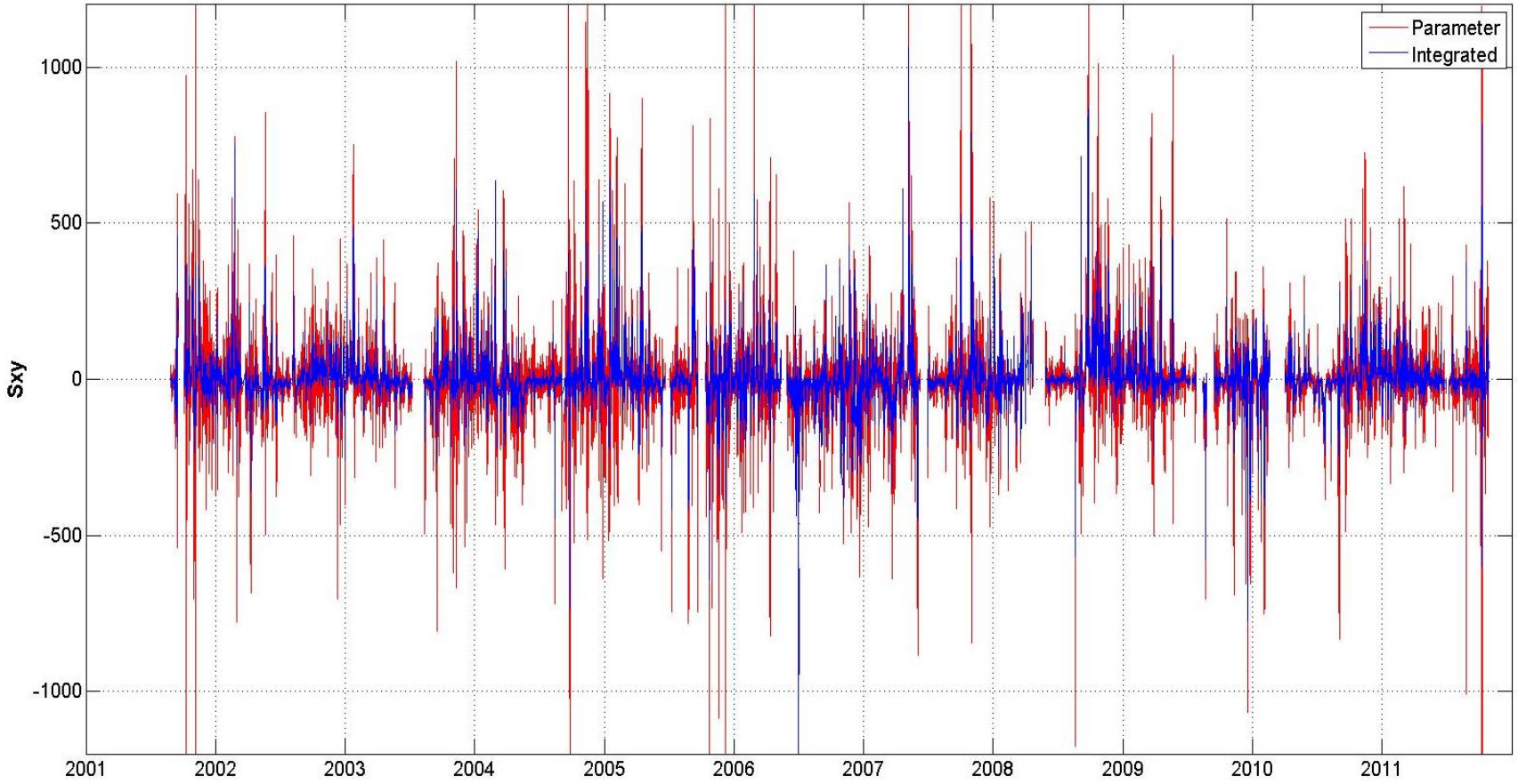

Figure 4.1: Time series of integrated-based vs parameter-based Radiation Stress (S_{xy}) estimates at Spessard.

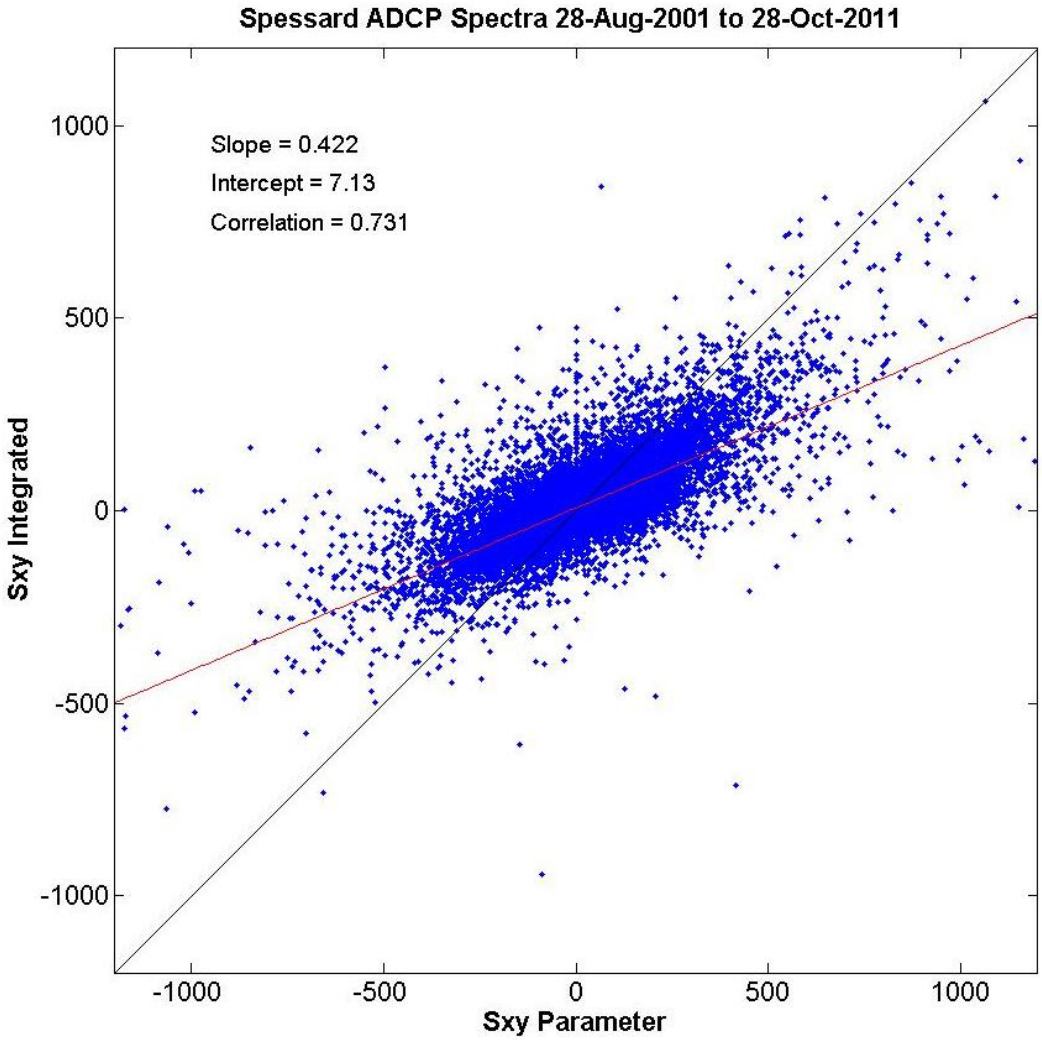

Figure 4.2: Scatter plot of integrated-based vs parameter-based Radiation Stress (S_{xy}) estimates at Spessard.

Table 4.1 presents a comparison of the yearly averages between the two methods. It can be noted that both methods agree on the sign of the averge estimates in all the years except 2003-2004. Nevertheless, during some years the difference between the averages of the two methods varies greatly. Table 4.2 presents a comparison of the standard deviations calculated for both methods. Parameter-based standard deviations are much higher than those from the integrated-based method.

Table 4.1: Comparison of average radiation stress (S_{xy}) between integrated-based and parameter-based estimates

Time Period	Integrated S_{xy} (N/m)	Parameter Based S_{xy} (N/m)
2001-02	11.4	7.30
2002-03	10.3	6.74
2003-04	4.22	-9.00
2004-05	13.4	2.13
2005-06	-0.09	-17.0
2006-07	-8.79	-19.1
2007-08	5.50	0.78
2008-09	31.0	36.8
2009-10	-11.0	-24.0
2010-11	16.2	19.4
Average	7.22	0.41

Table 4.2: Comparison of the standard deviation of radiation stress (S_{xy}) between integrated-based and parameter-based estimates

Time Period	Integrated Sxy (N/m)	Parameter Based Sxy (N/m)
2001-02	78.7	146.4
2002-03	48.7	87.1
2003-04	67.9	119.2
2004-05	93.7	186.0
2005-06	79.3	157.0
2006-07	96.3	128.5
2007-08	72.7	119.7
2008-09	90.5	141.6
2009-10	65.9	108.5
2010-11	57.9	100.2
Average	77.2	133.4

4.2 Behavior of Integration-Based Radiation Stress S_{xy} at Spessard Holland Park

The behavior of the radiation stress component, S_{xy}, in the nearshore is highly variable from year to year. Appendix D presents yearly time series of integrated-based S_{xy} estimates. Some of the years have active S_{xy} seasons while others do not, suggesting significant variability in the longshore current forcing from one year to another.

Figure 4.3 presents a histogram of S_{xy} estimates from the Spessard dataset. The average S_{xy} was 7.22 N/m with a standard deviation of 77.2 N/ m and with a skew of 1.81. A positive S_{xy} average for the entire record indicates net north-to-south forcing at this location, which is commonly assumed for the east coast of Florida. However, the fact that S_{xy} is nearly balanced is somewhat surprising, given the distinct indication of net north-to-south transport at east coast jettied inlets.

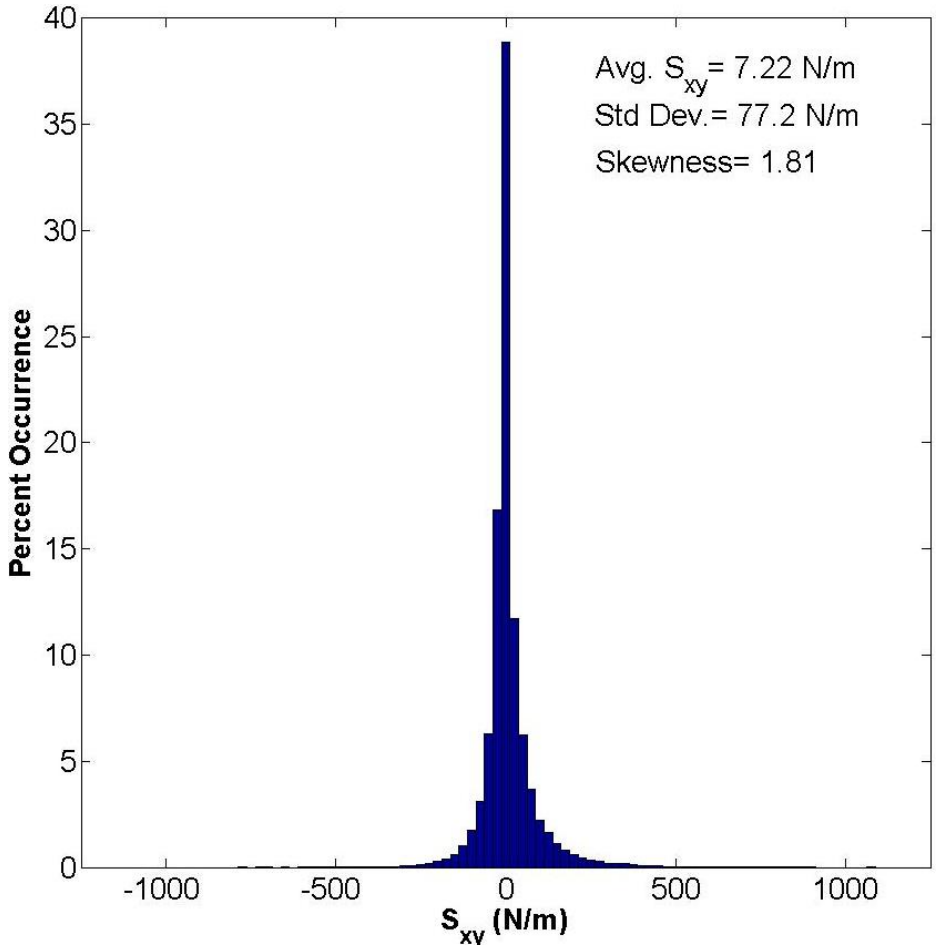

Figure 4.3: Histogram of Integrated-Based Radiation Stress (S_{xy}) Estimates at Spessard.

4.2.1 Analysis of the Years with the Highest and Lowest Average S_{xy}

Net longshore sediment transport in the east coast of Florida is known to be north-to-south. Nevertheless, three out of the ten years had a negative yearly average. As a means to further investigate these results, an average-spectra analysis was performed between the years with the lowest and highest S_{xy} average, 2009-10 and 2008-09, respectively.

Figure 4.4 presents the average of 3,964 and of 3,671 fully 2D spectra for 08-09 and 09-10, respectively. Figure 4.5 presents the average spectrum separated into the three different windows. Top plots in this figure display the average of the directional spectra that fall within the southeast window, for 08-09 and 09-10 respectively. The middle and bottom plots display the average spectra from the northeast and shore-normal windows, respectively. During 08-09 39% of the waves came from the southeast compared to 62% during 09-10. Also 36% and 19% of the waves came from the northeast during 08-09 and 09-10, respectively.

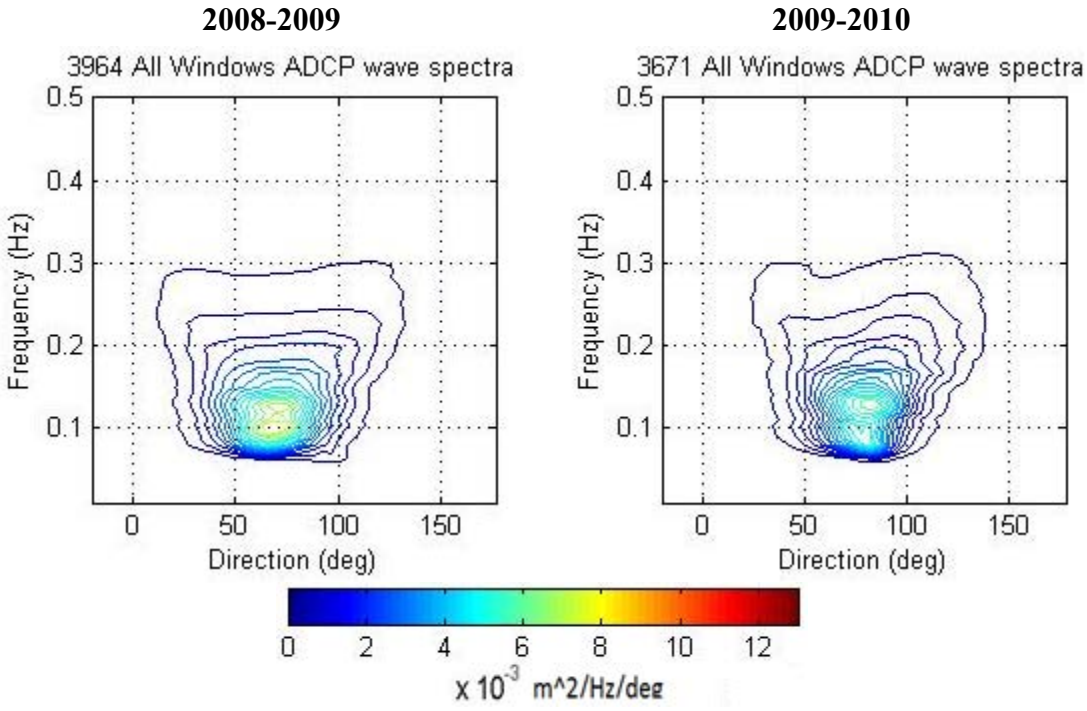

Figure 4.4: Average ADCP Spectra for all Windows for 08-09 and 09-10.

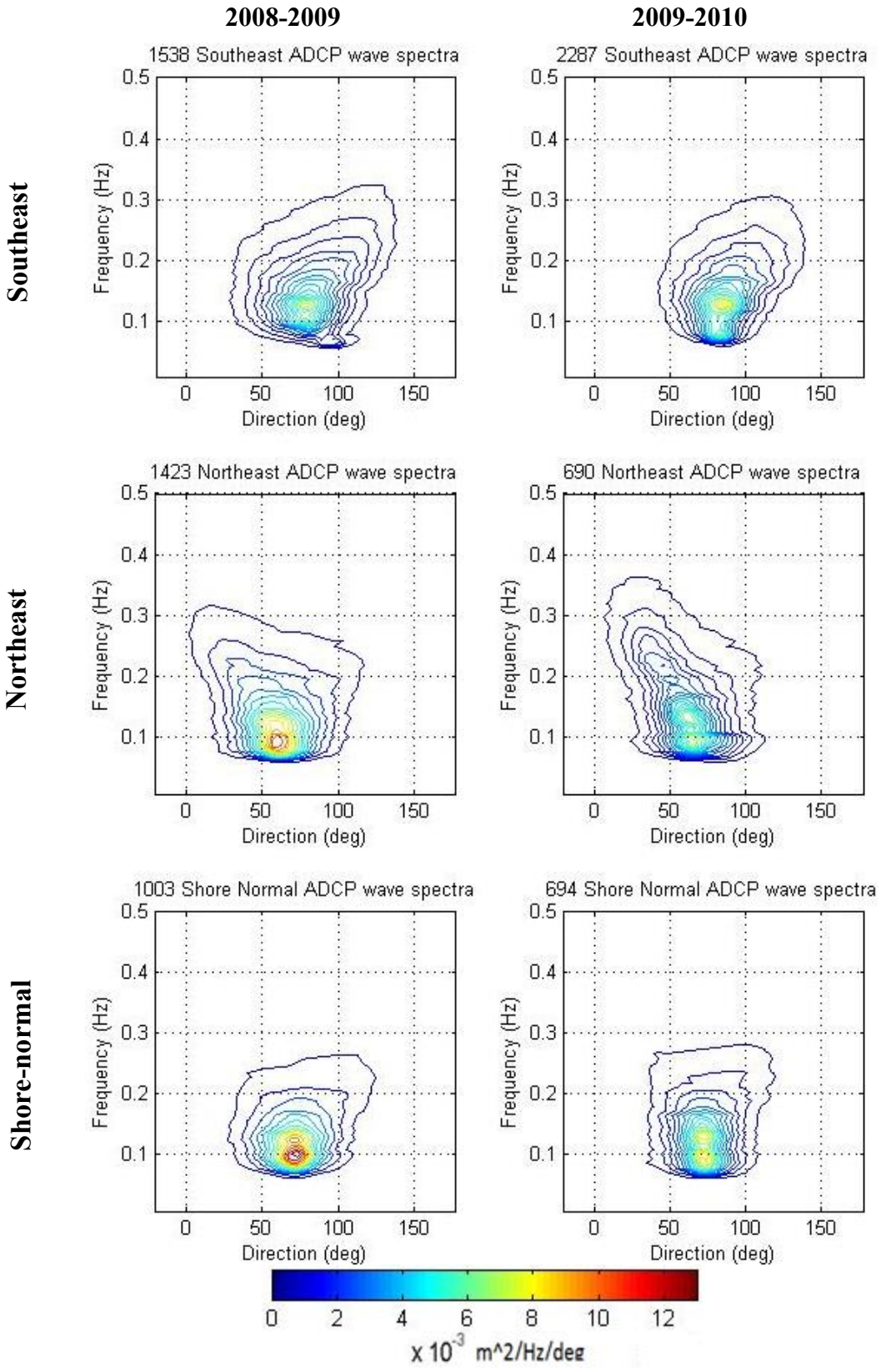

Figure 4.5: Average ADCP Spectra divided into separate windows for 08-09 and 09-10.

Table 4.3 presents the average energy for each window. During 08-09 the average energy is greater in each window than 09-10. Figures 4.6 and 4.7 present the average direction distribution for 08-09 and 09-10 respectively. The peak of the average of the 2D spectrum occurs at a direction of ~70° (north-to-south forcing) and ~82° (south-to-north forcing) for 08-09 and 09-10, respectively. It can be concluded that 08-09 had the largest positive S_{xy} average because it had a very energetic northeast window and a high percentage of waves (36%) approached from the northeast. On the other hand, 09-10 had the smallest S_{xy} average because the difference in average H_{mo} between the northeast and southeast window is small (0.05 m) and a high percentage of waves (62%) came from the southeast.

Table 4.3: Average H_{mo} Calculated for each Window

Average H_{mo} (m)			
Window	**08-09 Period**	**09-10 Period**	**All Data**
Southeast	0.74	0.73	0.78
Northeast	0.91	0.78	0.87
Shore-Normal	0.84	0.72	0.83
All Windows	0.83	0.74	0.83

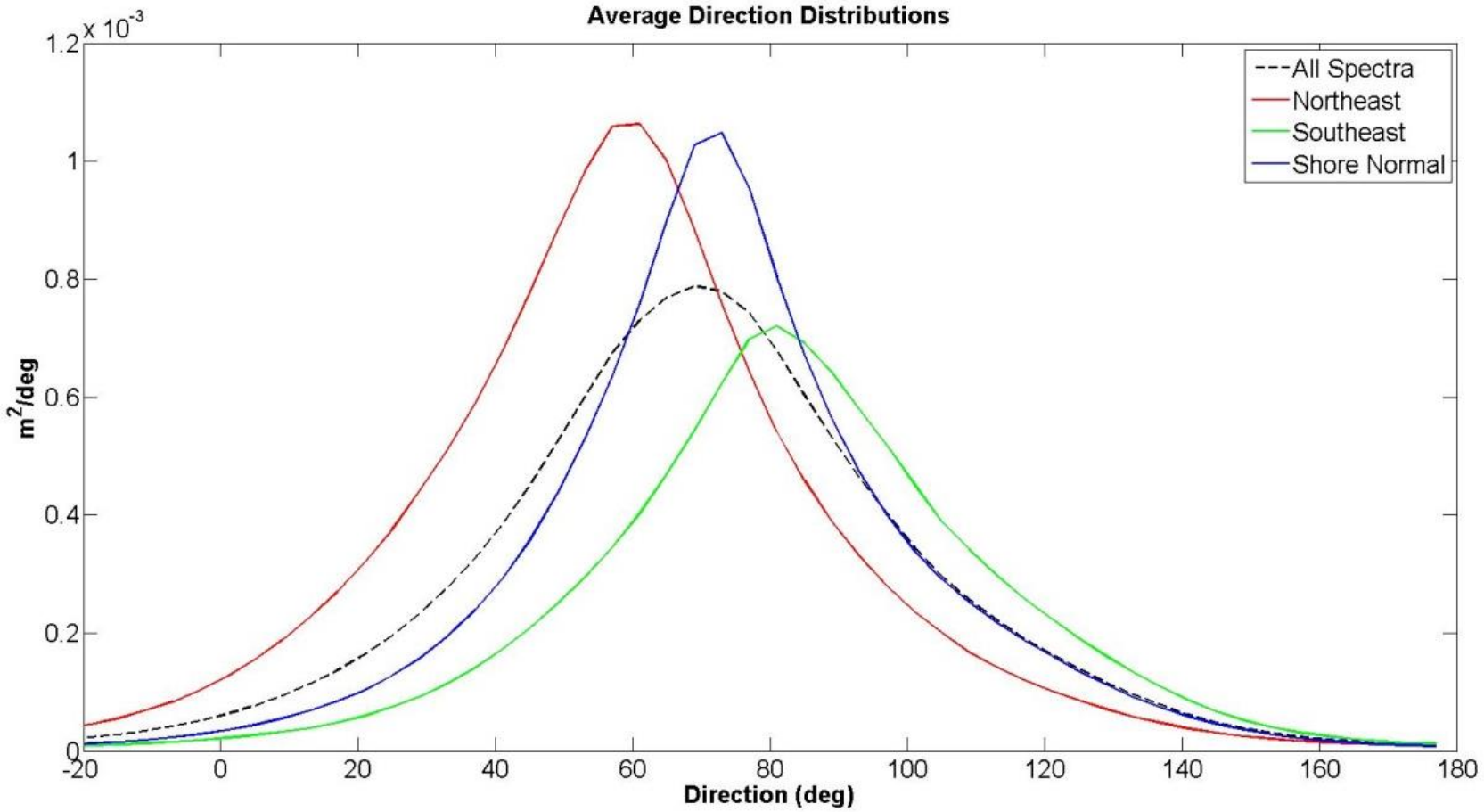

Figure 4.6: Average Direction Distribution 08-09.

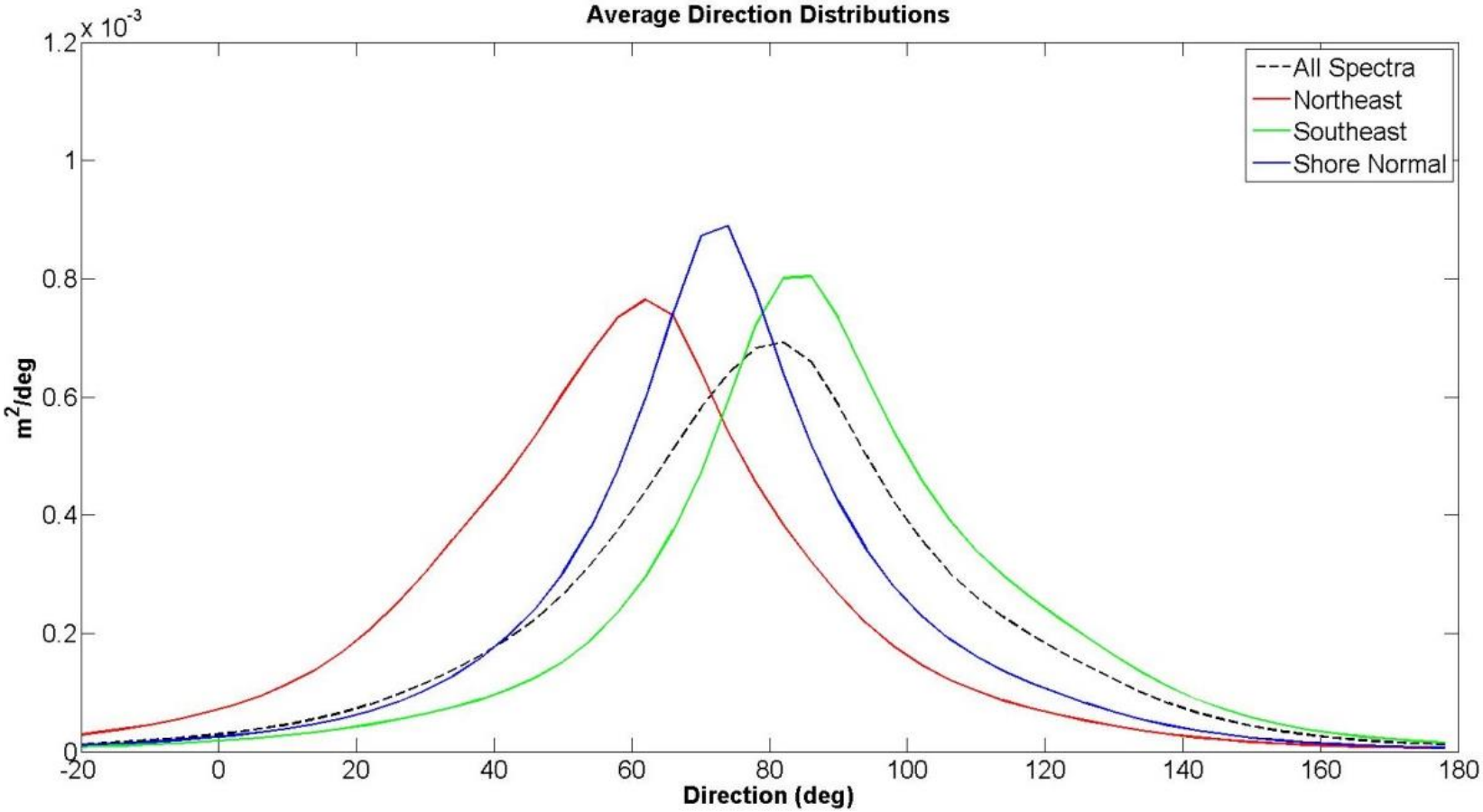

Figure 4.7: Average Direction Distribution 09-10.

4.2.2 Analysis of Integration-Based Radiation Stress (S_{xy}) Variability

Figure 4.8 presents a time series of integrated-based S_{xy} annual average. The average was done in the following manner: 1) daily averages were calculated and, 2) each day was averaged with the corresponding date in the subsequent years (e.g. Jan. 1, 2002 was averaged with Jan.1, 2003, 2004, 2005…etc.). It can be noted that during the winter season (Sept.-May.) S_{xy} average estimates came up mostly positive, while during the summer (May.-Sept.) they came up as negative for the most part indicating seasonal patterns in S_{xy}. It is also important to point out that during the months of April and May there were times where the value of S_{xy} spiked. This might indicate that during the change of seasons, longshore currents might be at their peak forcing. It is important to note that the average of this time series plot is equal to the total average of S_{xy} (7.22 N/m) stated previously.

Figure 4.8: S_{xy} Daily Almanac

To further explore the variability of S_{xy}, a 2-month running average was calculated and is presented in Figure 4.9. Yearly and seasonal variability can be noted. Also, it can be noted from the figure that seasonal S_{xy} patterns are present in the data. S_{xy} is predominantly positive between the months of October and April (7 out of 10 times) and negative between April and October (7 out of 10 times).

4.3 Importance of Long-term Datasets

Figure 4.10 presents a comparison of different time scale averages of S_{xy} averages. It is important to keep in mind that the average S_{xy} for the entire record was 7.22 N/m and that short-term wave measurements may not provide accurate information for coastal analyses. If 3 months of data were collected at this site, then there would be a 33% chance that the net forcing would be directed south-to-north. This percentage increases as the time scale averaging decreases. Not only you can get a higher or lower average, but you can also get an incorrect direction. Individual plots comparing each time scale average are presented in Appendix E.

Figure 4.11 presents a comparison of the calculated standard deviation between the four different time scale averages. The standard deviation increases by more than a factor of two between 12-month and 1-month averages. It can be concluded that results based on long-term measurements analysis have smaller margins of error than those from short-term measurements.

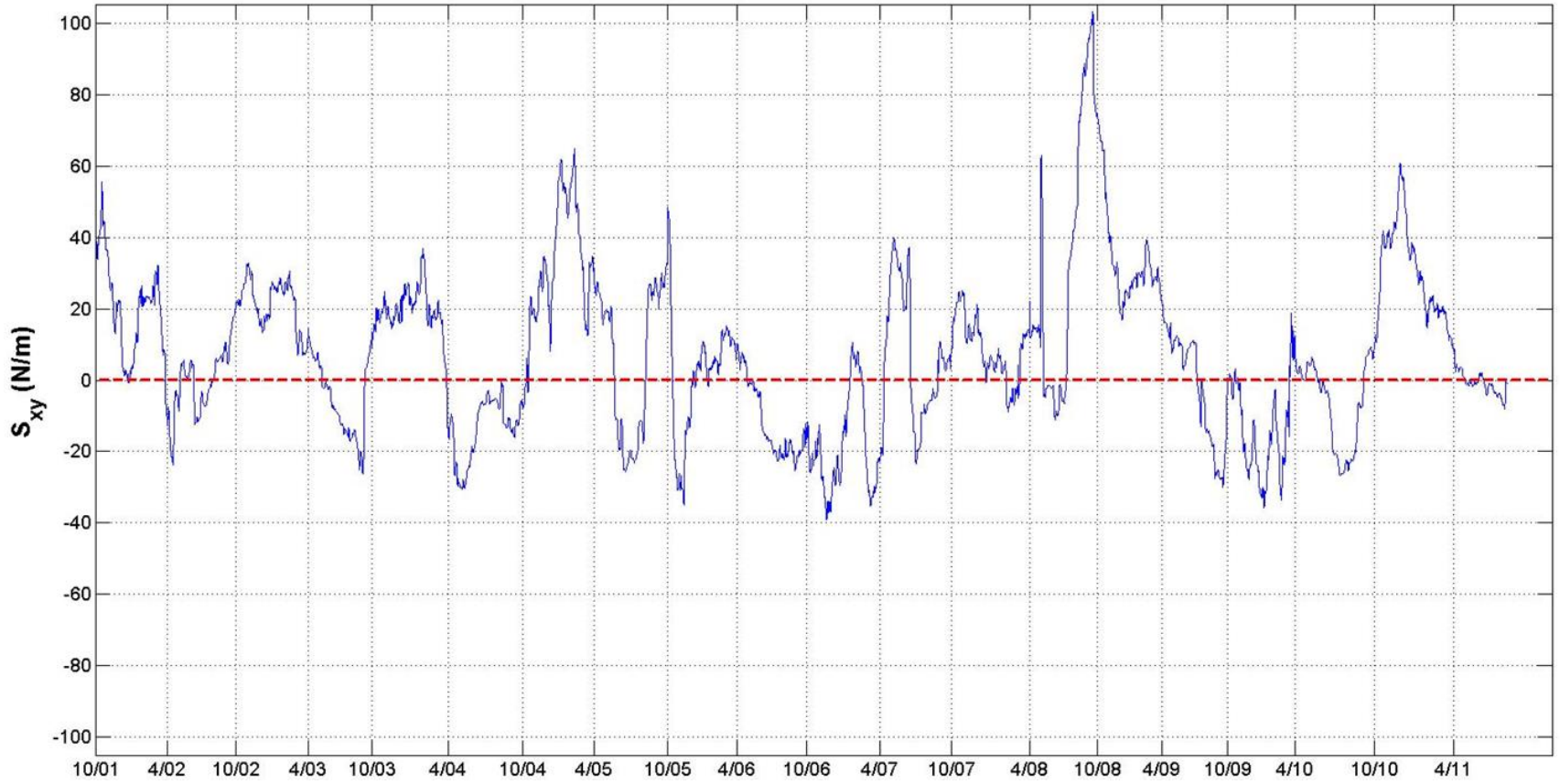

Figure 4.9: 2-Month Running Average of Integrated-Based Radiation Stress (S_{xy})

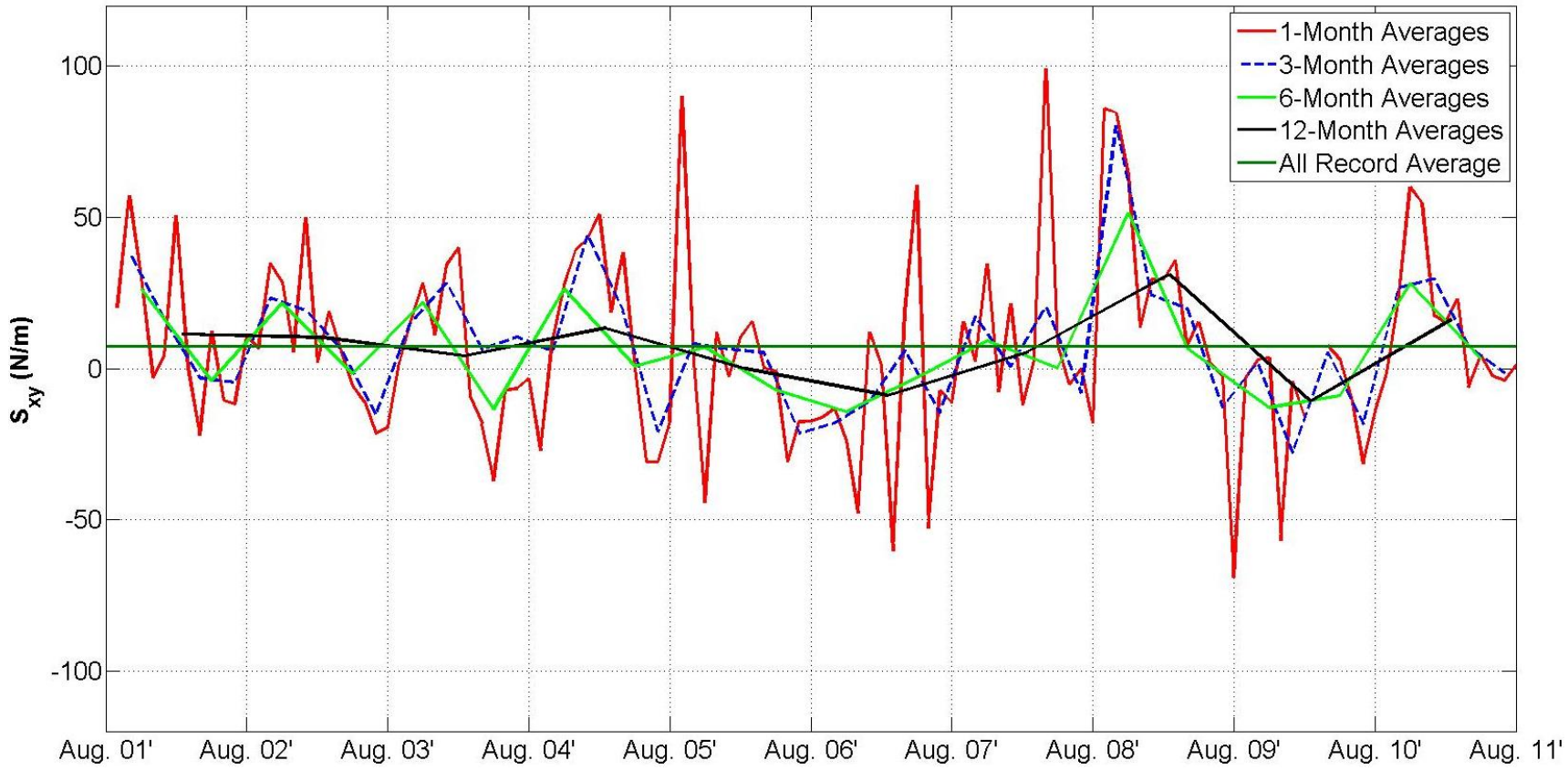

Figure 4.10: Comparison of different time scales radiation stress (S_{xy}) averages

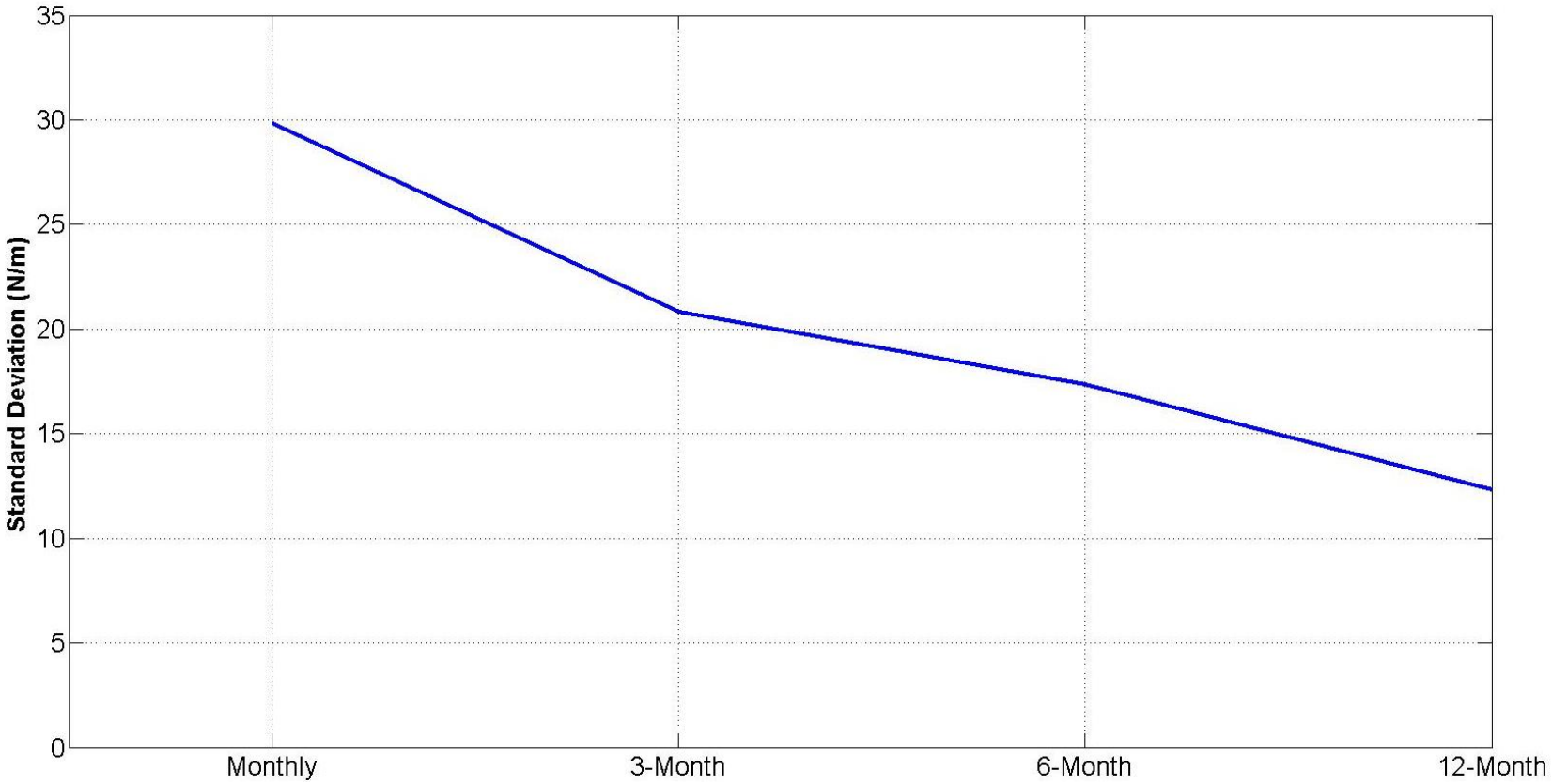

Figure 4.11: Comparison of the standard deviation between different time-averaging periods

4.4 Discussion

It is very important to use high-resolution, fully directional spectra in coastal engineering applications. A comparison was done of S_{xy} estimates between the integration-based calculation and parameter-based approximations. The results indicate that the parameter-based approximation over-predicts S_{xy} by 42%, because this method assigns all the wave energy into one direction (Ruessink et al., 2001). Figure 4.1 clearly shows this discrepancy. Also, the parameter-based method had a much higher yearly standard deviation than the integrated-based.

It is assumed in the east coast of Florida that the net longshore forcing is north-to-south. The average S_{xy} for the Spessard record was 7.22 N/m indicating a net north-to-south longshore forcing, as it was hypothesized. A larger average was expected, given the offsets present in all the inlets in east coast of FL. Nevertheless, offsets have been formed by many years of sediment transport, so even a 7.22 N/m average can make a big difference over, e.g. 50 years.

Results showed that the annual and seasonal variability of S_{xy} was very high but some seasonal patterns were present in the data. Figures 4.8 and 4.9 indicate that there are seasonal patterns in the behavior of S_{xy}. S_{xy} is predominantly positive between the months of October and April (70% of the time) and negative between April and October (70% of the time). Finally, results indicate that short-term wave records may not provide accurate information for planning purposes. For example, if only 3-months of data were collected at this site, there would be a 33% chance that the longshore forcing would be directed from south-to-north. Figure 4.11 shows that the standard deviation decreases with longer-term datasets, indicating that the margin of error decreases when long-term datasets are analyzed.

Chapter 5:

WIND STRESS ANALYSIS

A higher average of longshore forcing was expected at this particular location, given that the Port Canaveral entrance and Sebastian Inlet, Figures 1.1 and 1.2 respectively, display significant offsets which indicate a strong net north-to-south transport from year to year. In searching for a plausible explanation, this chapter presents the analysis of six years of wind data from the Spessard station collected from September 12, 2002 until October 7, 2008.

5.1 Wind Stress Estimates

As mentioned before, wind is also a force responsible for driving longshore currents in the nearshore. Wind transfers a momentum to the sea surface that generates currents. The wind stress vector can be represented from the following relation

$$\vec{\tau} = \rho C_d \vec{U}_{10} \left| \vec{U}_{10} \right| \tag{5.1}$$

where ρ is the air density, $C_d$is the drag coefficient, $\left| \vec{U}_{10} \right|$ is the norm of the wind speed vector at 10 m elevation and $\vec{U}_{10}$is the wind speed vector. C_d can be calculated from the following equation proposed by Garratt (1977)

$$C_d = \frac{1}{1000}\left(\frac{15}{20} + \frac{40}{600}U_{10}\right) \quad (5.2)$$

Table 5.1 was developed using both equation 5.1 and 5.2. It presents yearly averages of wind stress at Spessard. During the entire record, 4 out of the 7 years had a positive average, but the total average came out as negative.

Table 5.1: Yearly averages of wind stress at Spessard

Yearly Averages	
Year	**Wind Stress (N/m^2)**
2002	0.00132
2003	0.00179
2004	0.00215
2005	0.00096
2006	-0.00652
2007	-0.0104
2008	-0.00832
Average	-0.00272

The expectation was to find a positive wind stress average. Positive average would indicate a net north-to-south longshore forcing. Even if the surf zone was 100 m width, this would not change much the average forcing. When long period waves approach the shore from the northeast (during nor'easters); they refract and break almost at a shore-normal direction (73°). It was assumed that currents, during nor'easter storms, would be generated by the winds directed from the north. Further study of this subject is required to better understand wind generated currents during storm events. It can be concluded that currents generated by oblique waves are the main contributor for longshore sediment transport.

Chapter 6:

CONCLUSIONS

Over ten years of ADCP data collected at Melbourne Beach, FL were analyzed. The data show large examples of yearly variability in the nearshore wave climate. The two years compared (02-03 and 04-05) showed a clear example of the variability in the energy-based significant wave height (H_{mo}), peak period (T_p), mean direction (θ_{mean}) and energy distribution from year to year. The results show that wave climate is very unpredictable from year to year.

Analysis of the average spectrum for the entire record indicates a neutral net forcing for this location. The energy for the entire record is distributed almost symmetrically, with the peak being at ~74° (73° being shore-normal). Analysis of the averaged spectrum by itself might not be a good indicator of the net longshore forcing. Further analysis on the directional spectra revealed that waves from the northeast (avg. H_{mo} = 0.87 m) were much more energetic than those from the southeast (avg. H_{mo} = 0.78 m) and shore-normal (avg. H_{mo} = 0.83m). Nevertheless, 53% of the waves arrived from the southeast, more than the other two windows combined.

Energy-based significant wave height (H_{mo}), peak period (T_{peak}) and mean period (T_{mean}) distributions were studied and modeled. The method of moments was used to calculate the best fit parameters for all distributions. The shifted gamma and shifted lognormal distributions provided a good fit to the Spessard H_{mo} data. A slightly better fit was accomplished by the shifted

gamma model (3.00% error) compared to the shifted lognormal (7.84% error). The shifted gamma model can be used to model long-term H_{mo} distributions.

The shifted lognormal model had success modeling T_{mean} data. The model got into trouble in the 4-7 sec range of the data, therefore missing the two peaks of the distribution. The root mean square error (ε_{rms}) for this distribution was 9.34%. The shifted lognormal distribution can be used to model long-term mean period datasets. Lastly, the Gaussian distribution provided the best fit to the T_p data (22.9%). One of the reasons for a high ε_{rms} is because the ADCP reports its measurements in terms of peak frequency rather than peak period.

Radiation stress (S_{xy}) estimates were computed using the integration-based and parameter-based approximations. Results revealed that the parameter-based approximation over-predicts the integrated S_{xy} by 42% (Figure 4.1 and 4.2). Ruessink (2001) concluded that the parameter-based approximation assigns all the wave energy into one direction, therefore over-predicting the value of S_{xy}. The use of use of high-resolution, fully directional spectra in coastal engineering applications is highly recommended.

It was hypothesized that net longshore forcing in the east coast of Florida is north-to-south, as it is commonly assumed. The calculated S_{xy} average of 7.22 N/m^2 for the entire record indicates a net north-to-south forcing of the longshore current at this site. There is clear agreement between our results and the stated hypothesis.

Furthermore, the S_{xy} analysis showed yearly and seasonal variability. Also Figures 4.8 and 4.9 show seasonal S_{xy} patterns. S_{xy} was mostly positive between the months of October and April

(70% of the time) and negative between April and October (70% of the time). Finally; results indicate that short-term wave measurements may not provide accurate information for planning purposes. For example, if only one-month of data were collected at this site, there would be a 41% chance that the longshore forcing would be directed from south-to-north. Figure 4.11 clearly shows that the standard deviation decreases with longer-term records.

Finally, a higher average of longshore forcing of the currents was expected at this particular location. To further analyze longshore currents, wind stress estimates were calculated at Spessard. The calculated wind stress average of 2.7×10^{-3} N/m^2 indicate a south-to-north longshore forcing due to winds. Further analysis is recommended on this subject to better understand the wind generated currents. It can be concluded that sediment transport is mostly driven by wave generated currents.

REFERENCES

Print Publications:

Battjes, J.A., "Radiation Stresses in Short-Crested Waves," J.Mar.Res., 1972, V30, pp.56-64

Dally, W.R., and Osiecki, D.A., "Nearshore Wave and Current Measurements During Hurricane Jeanne," Shore and Beach, 2005, V73, No. 2-3, 29-33.

Garratt, J.R., "Review of Drag Coefficients Over Oceans and Continents," Monthly Weather Review, 1977, 105, 915-929.

Kennedy, A., and Dean, R.G., "Wave Gauge Orientation at Melbourne Beach, FL," contract report to the Florida Beaches and Shore Resources Center, 2005, 11pp.

Lawson, N.V. and Abernethy, C.L., "Long-Term Wave Statistics off Botany Bay," Proceedings of the 2nd Australian Conference on Coastal and Ocean Engineering, Sydney, Australia, pp. 167-176, 1975.

Leadon, M.E., Dally, W.R, and Osiecki, D.A., "The Florida Coastal Forcing Project," Proc. of the Florida Shore and Beach Preservation Association., Orlando Florida, 2004.

Leyden, V., and W. Dally, "Probabilistic Modeling of Long-Term Wave Climate," Coastal Eng., Proceedings, 1996.

Leyden, V., "Probabilistic Modeling of Long-Term Wave Climate," Thesis, Florida Institute of Technology, 1997.

Longuet-Higgins, M. S.; Stewart, R. W., "Radiation stresses in water waves; a physical discussion, with applications," Deep Sea Research, 1964, 11 (4): 529–562,

Ochi, M.K., "On Long-Term Statistics for Ocean and Coastal Waves," Proc. 16th Conf. Coastal Engineering, pp. 59-75, 1978.

Rossouw, J., "Design Waves and Their Probability Density Functions," Proc. 21st Conf. Coastal Engineering, pp. 822-834, 1988.

Ruessink, B. G., J. R. Miles, F. Feddersen, R. T. Guza, and S. Elgar, "Modeling the alongshore current on barred beaches," J. Geophys. Res., 106, 22, 451-22, 463, 2001.

Electronic Sources:

Absalonsen, L. and R.G. Dean “Characteristics of shoreline change along the sandy beaches of the State of Florida: an Atlas,” 2010, http://nsgl.gso.uri.edu/flsgp/flsgpm10001.pdf, accessed April 1, 2014.

NOAA, “Ocean Facts”, http://oceanservice.noaa.gov/facts/population.html , last revision 2013, last accessed September 27, 2013.

U.S. ARMY, CORPS OF ENGINEERS, Field Research Facility Homepage, http://www.frf.usace.army.mil, accessed March 15, 2014.

APPENDIX A

Shore Station at Spessard Holland Park, Melbourne Florida

Figure A.1: Spessard Holland Park, Brevard County (Photographer: W. Dally).

APPENDIX B

WaveMon Format 8 Sample Output Files and Parameters

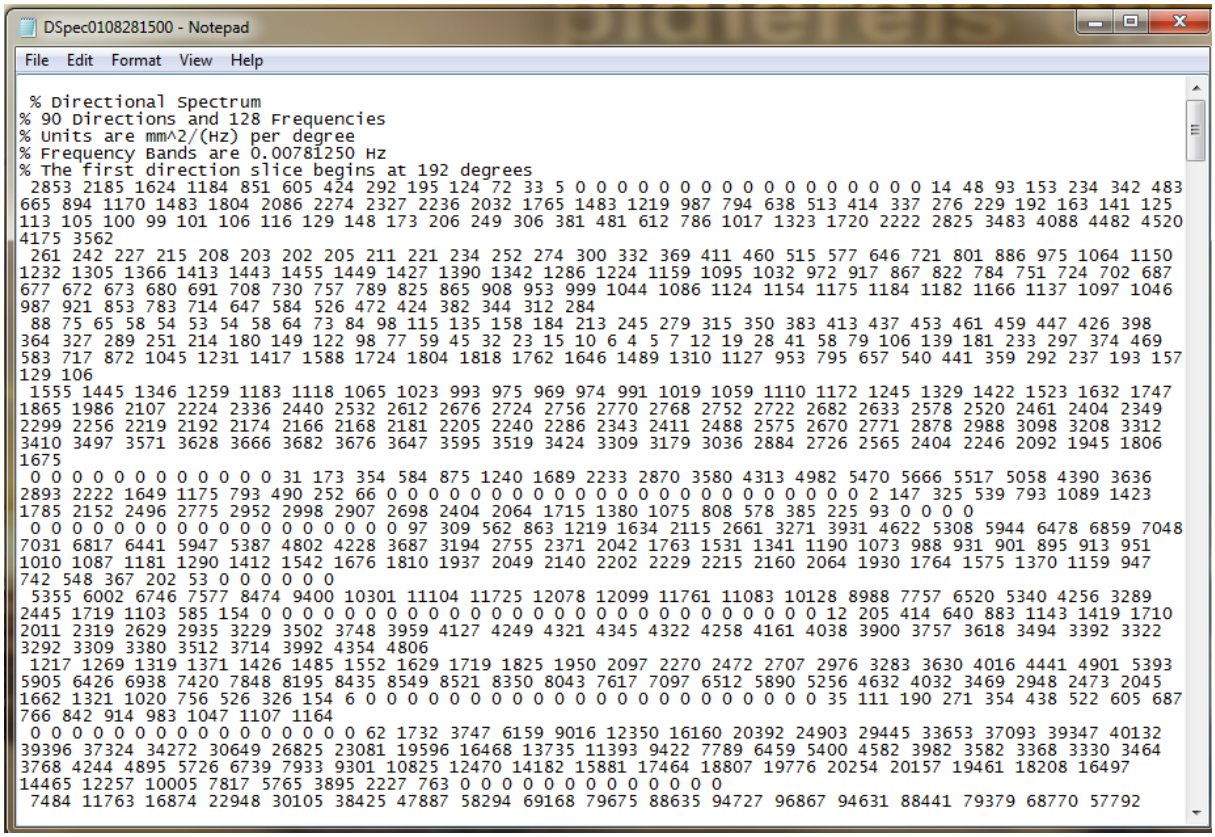

Figure B.1: Example of Directional Spectrum File.

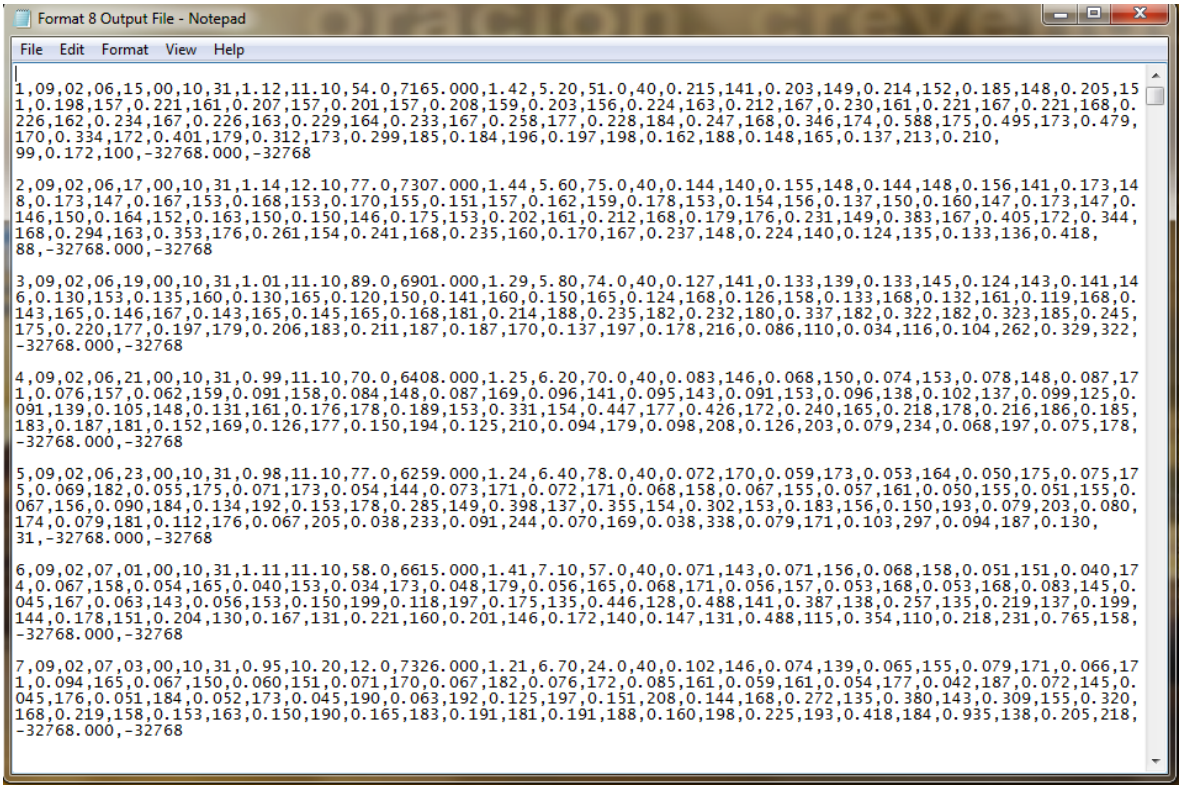

Figure B.2: Example of Format 8 Output Parameter File.

Format 8

Waves Parameters Log: Format 8

String	Description
Burst#	Burst number
YY,MM,DD,HH,mm,ss,cc	Date and time field. Leading zeros are always included to maintain fixed length. YY = 2 fixed digits for year, MM= 2 fixed digits for month, and DD= 2 fixed digits for day. HH = 2 fixed digits of hours, mm = 2 fixed digits of minutes, ss = 2 fixed digits of seconds, and cc = 2 fixed digits of 1/100th seconds.
Hs	Significant Wave Height (meters) $Hs = 4\sqrt{M_0}$
Tp	Peak Wave Period (seconds) - period associated with the largest peak in the power spectrum
Dp	Peak Wave Direction (degrees) - peak direction at the peak period.
Depth	Water level (from pressure sensor) (millimeters)
$H_{1/10}$	$H_{1/10}$ (10% highest waves) = 1.27 * Hs
Tmean	Mean Period (seconds) $T_{01} = T\_\_ = \frac{M_0}{M_1}$
Dmean	Mean Peak Wave Direction (degrees)
#bins	Number of bins
depthlevel1Magnitude	Depth Level 1 Magnitude (m/s)
depthlevel1Direction	Depth Level 1 Direction (deg)
↓	
depthlevelNMagnitude	Depth Level N Magnitude (m/s)
depthlevelNDirection	Depth Level N Direction (deg)

Figure B.3: List of Format 8 Wave Parameters

APPENDIX C

Yearly Time Series of Energy-Based Significant Wave Height, Peak Period, Mean Direction, Wind Direction and Wind Velocity

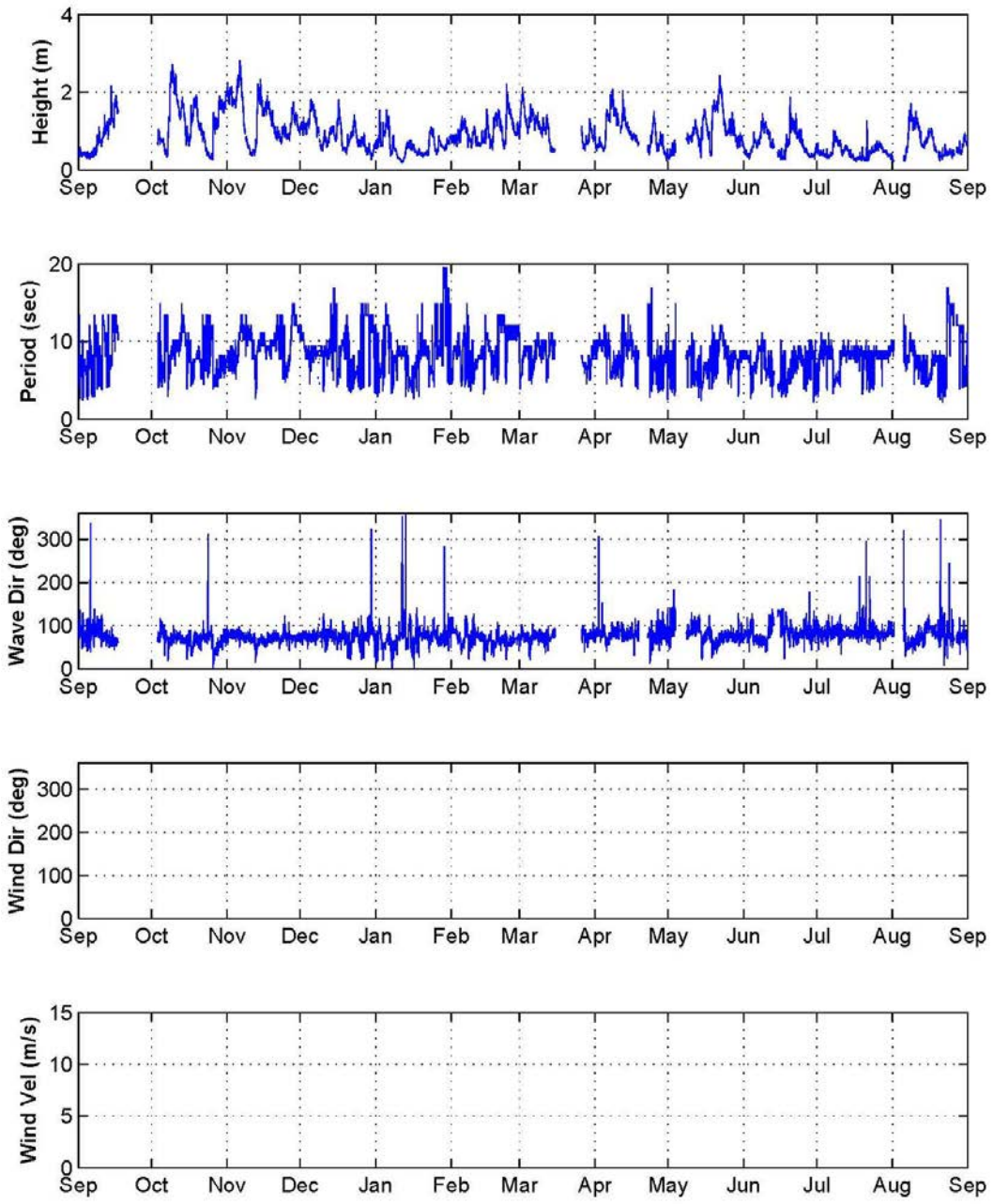

Figure C.1: Record of energy-based significant wave height (H_{mo}), peak period (T_p), mean direction (θ_{mean}), wind direction and wind velocity from FCFP Station Spessard 2001-2002.

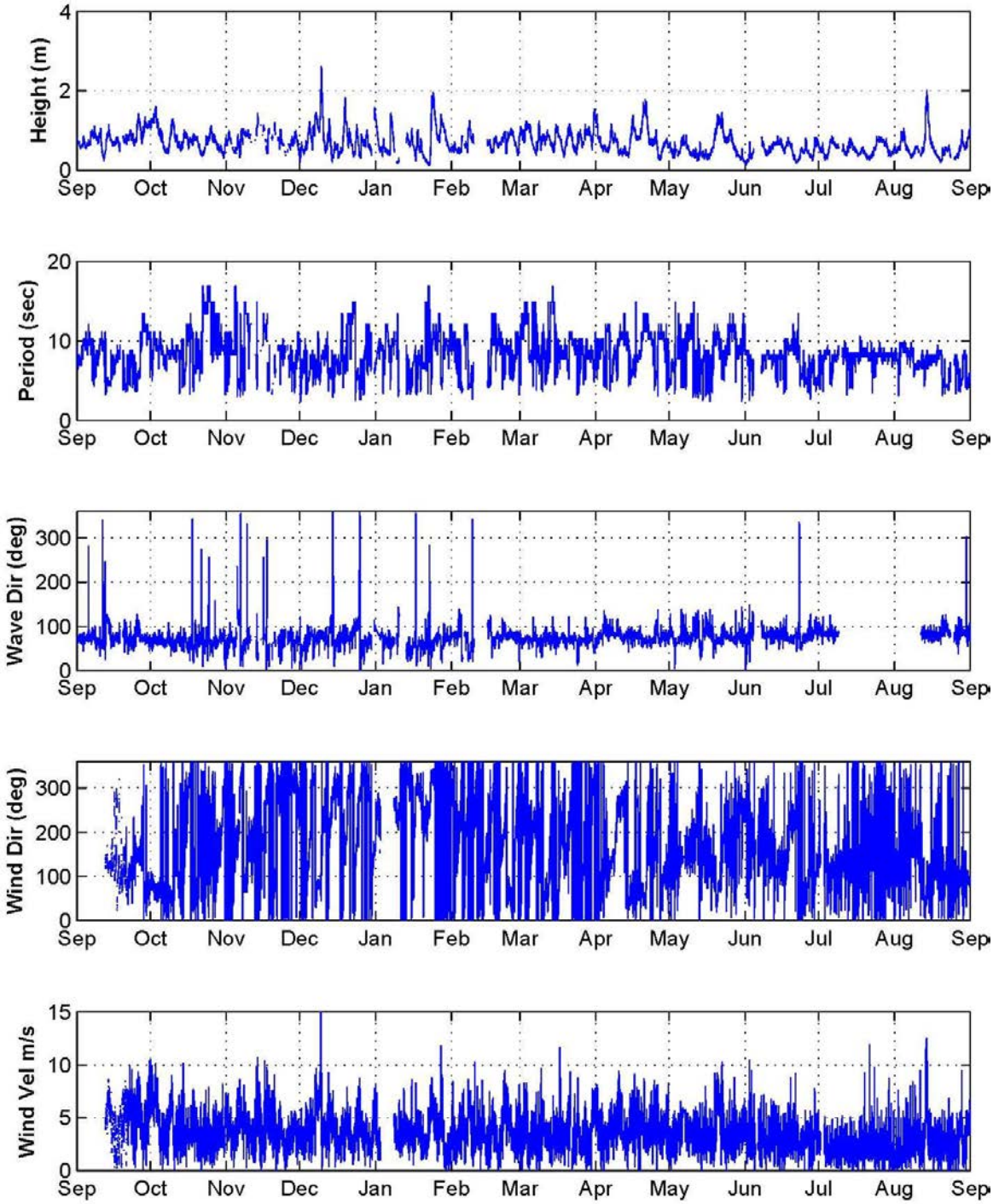

Figure C.2: Record of energy-based significant wave height (H_{mo}), peak period (T_p), mean direction (θ_{mean}), wind direction and wind velocity from FCFP Station Spessard 2002-2003.

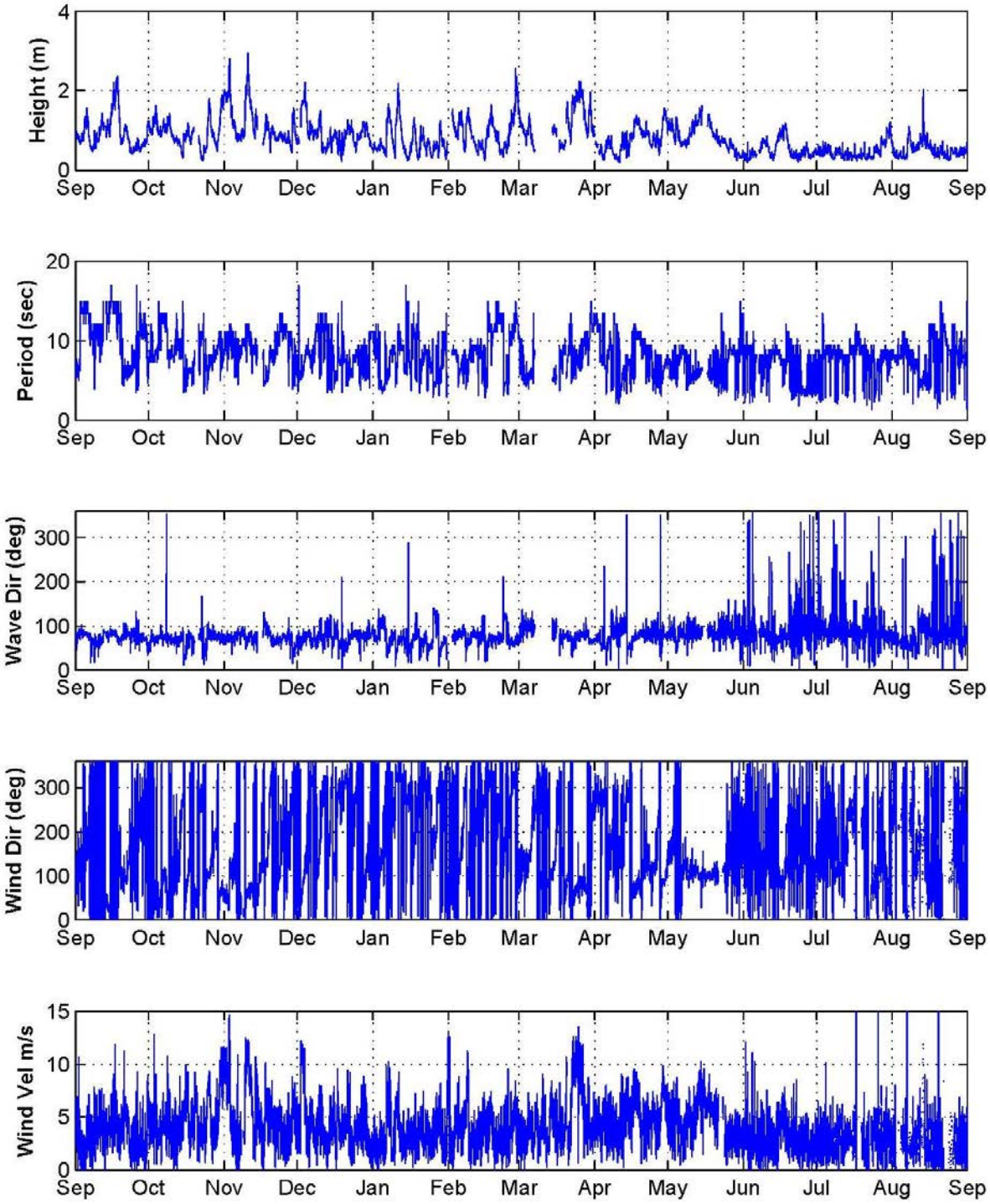

Figure C.3: Record of energy-based significant wave height (H_{mo}), peak period (T_p), mean direction (θ_{mean}), wind direction and wind velocity from FCFP Station Spessard 2003-2004.

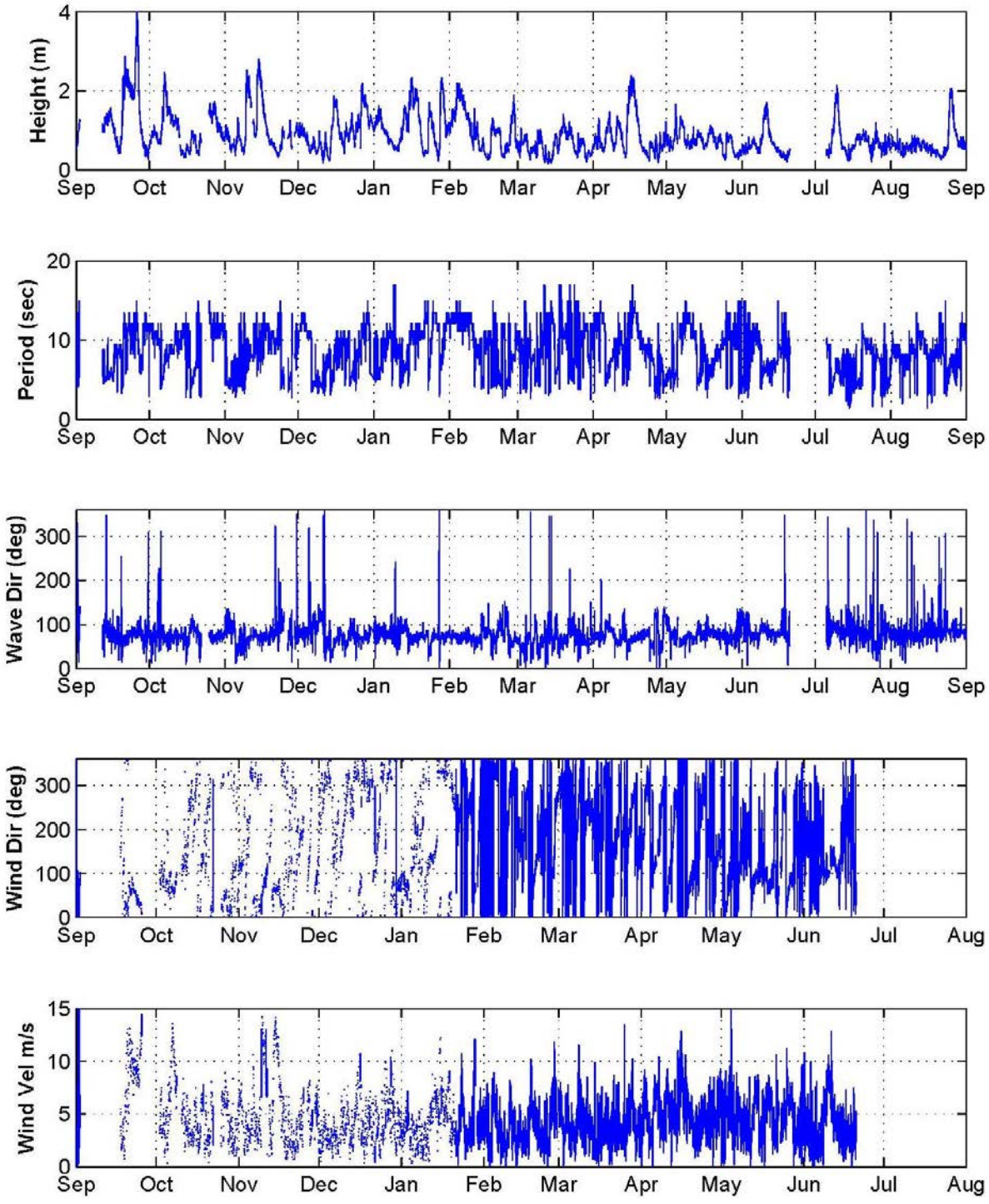

Figure C.4: Record of energy-based significant wave height (H_{mo}), peak period (T_p), mean direction (θ_{mean}), wind direction and wind velocity from FCFP Station Spessard 2004-2005.

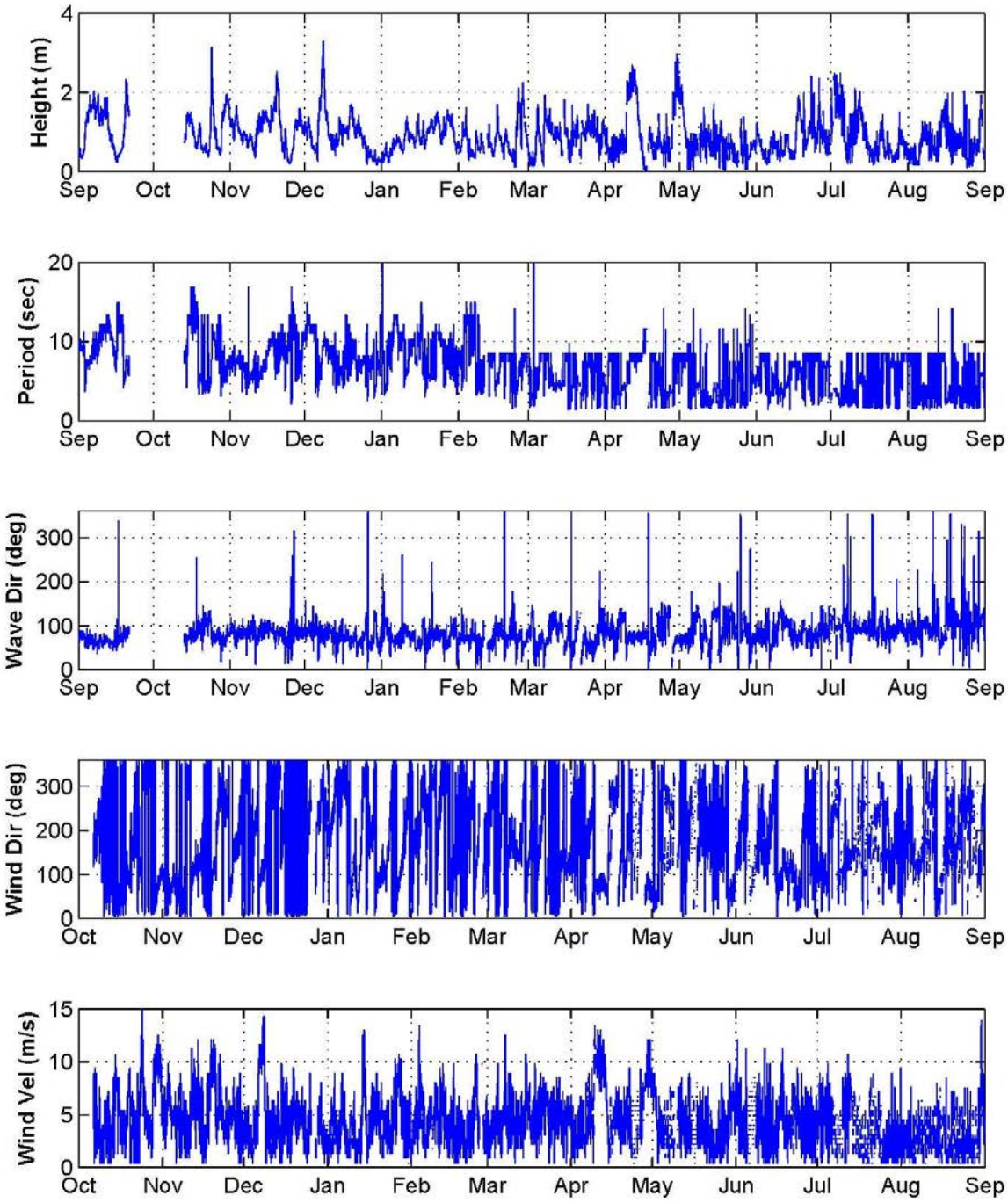

Figure C.5: Record of energy-based significant wave height (H_{mo}), peak period (T_p), mean direction (θ_{mean}), wind direction and wind velocity from FCFP Station Spessard 2005-2006.

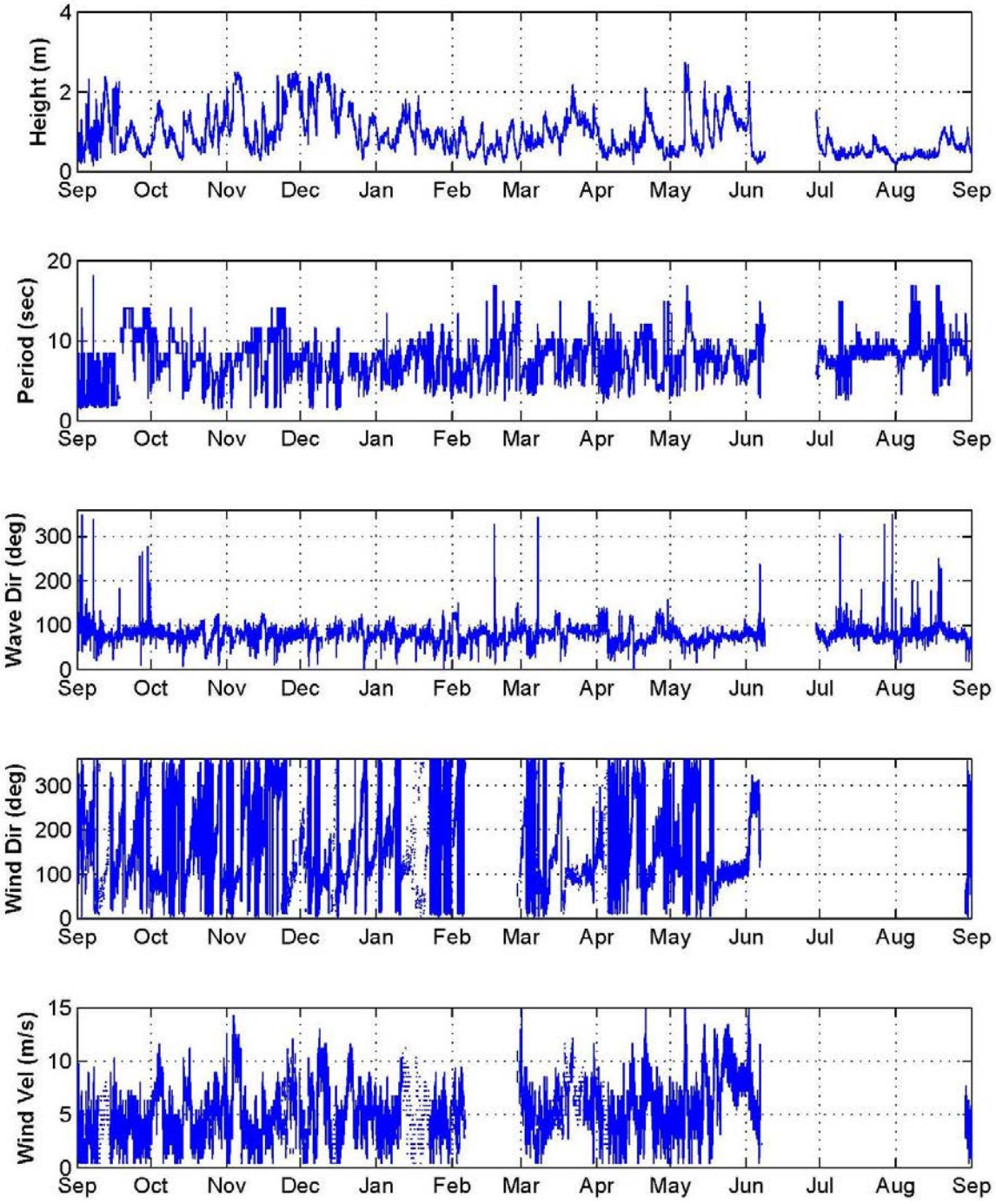

Figure C.6: Record of energy-based significant wave height (H_{mo}), peak period (T_p), mean direction (θ_{mean}), wind direction and wind velocity from FCFP Station Spessard 2006-2007.

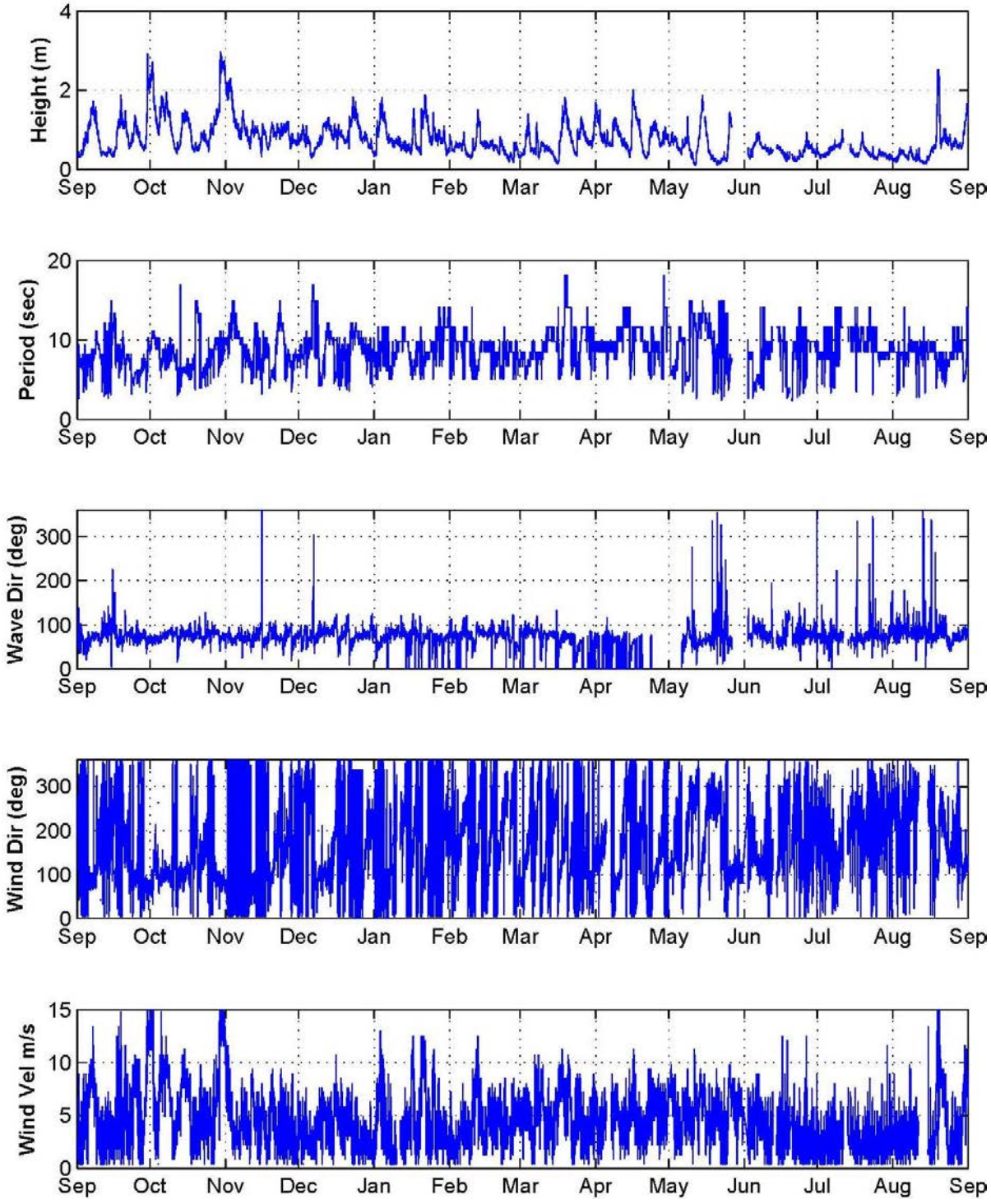

Figure C.7: Record of energy-based significant wave height (H_{mo}), peak period (T_p), mean direction (θ_{mean}), wind direction and wind velocity from FCFP Station Spessard 2007-2008.

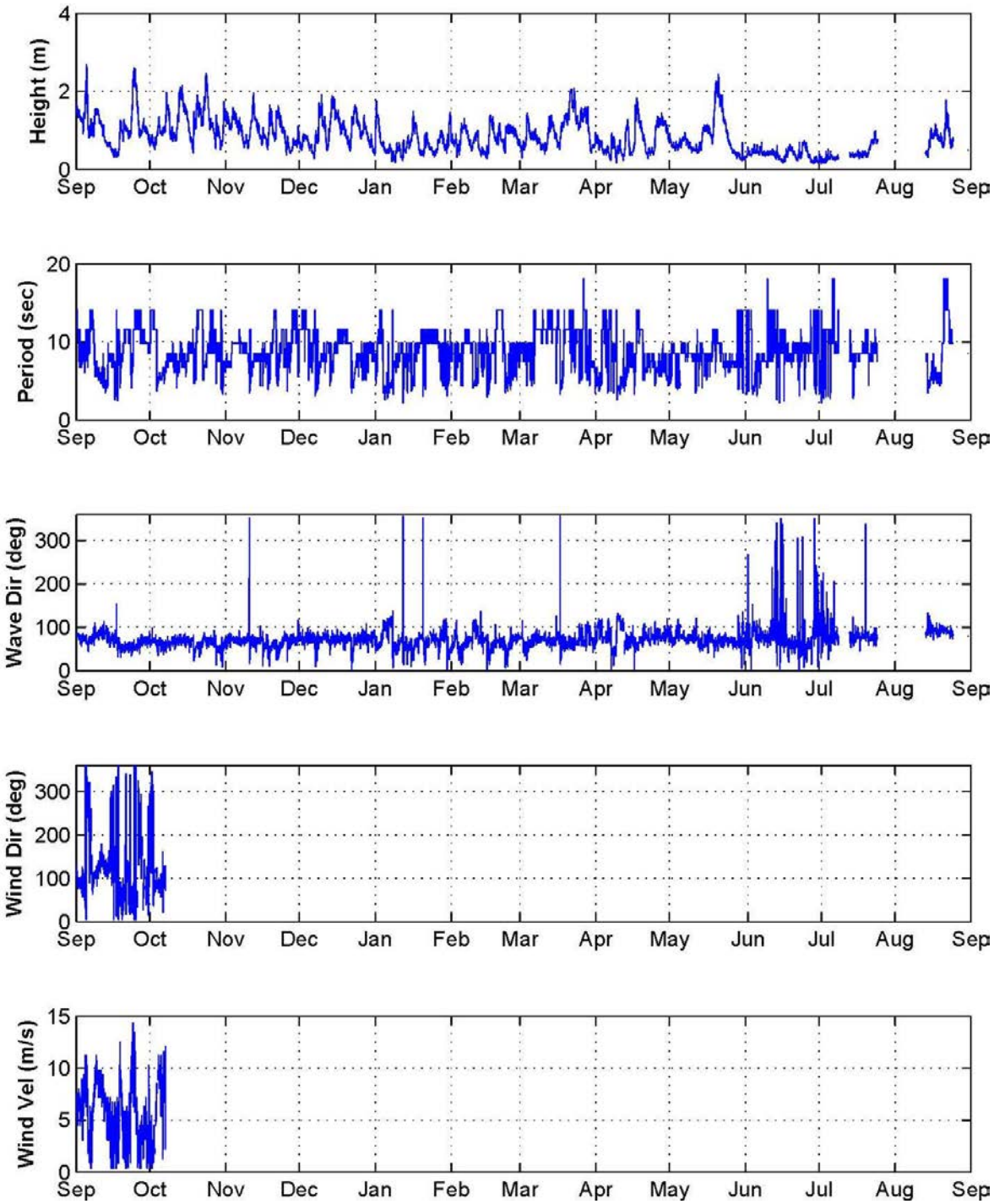

Figure C.8: Record of energy-based significant wave height (H_{mo}), peak period (T_p), mean direction (θ_{mean}), wind direction and wind velocity from FCFP Station Spessard 2008-2009.

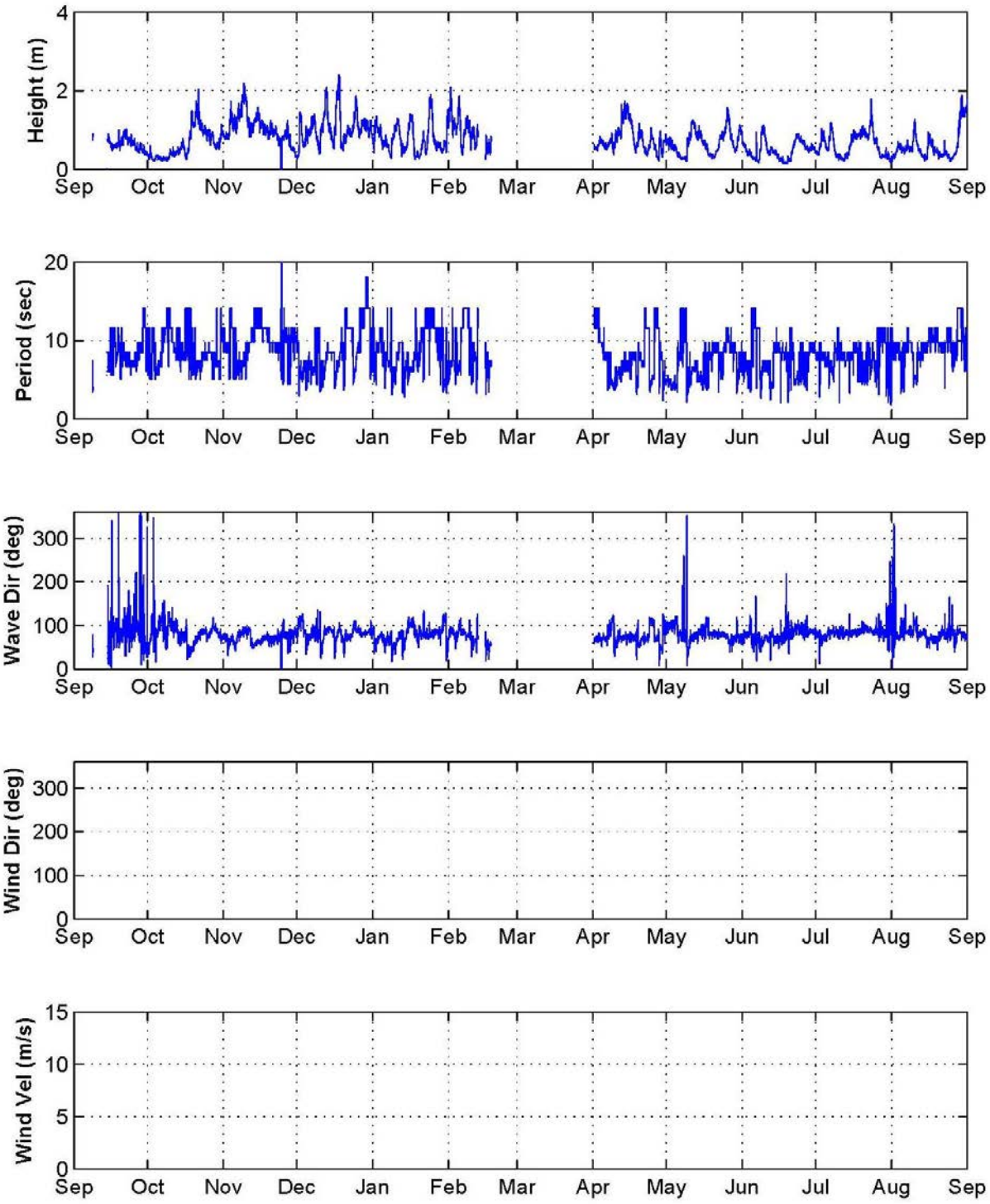

Figure C.9: Record of energy-based significant wave height (H_{mo}), peak period (T_p), mean direction (θ_{mean}), wind direction and wind velocity from FCFP Station Spessard 2009-2010.

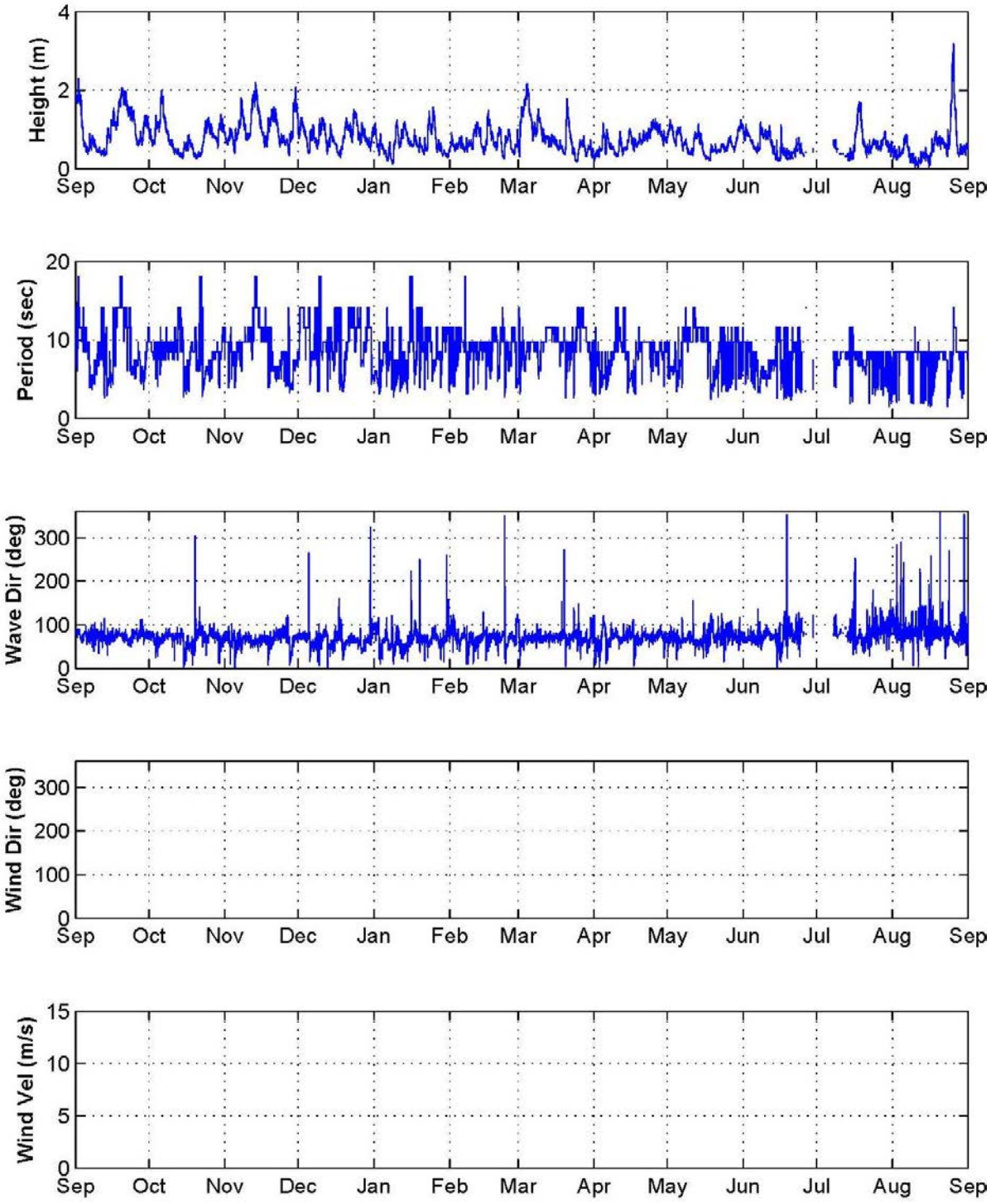

Figure C.10: Record of energy-based significant wave height (H_{mo}), peak period (T_p), mean direction (θ_{mean}), wind direction and wind velocity from FCFP Station Spessard 2010-2011.

APPENDIX D

Record of Radiation Stress Estimates

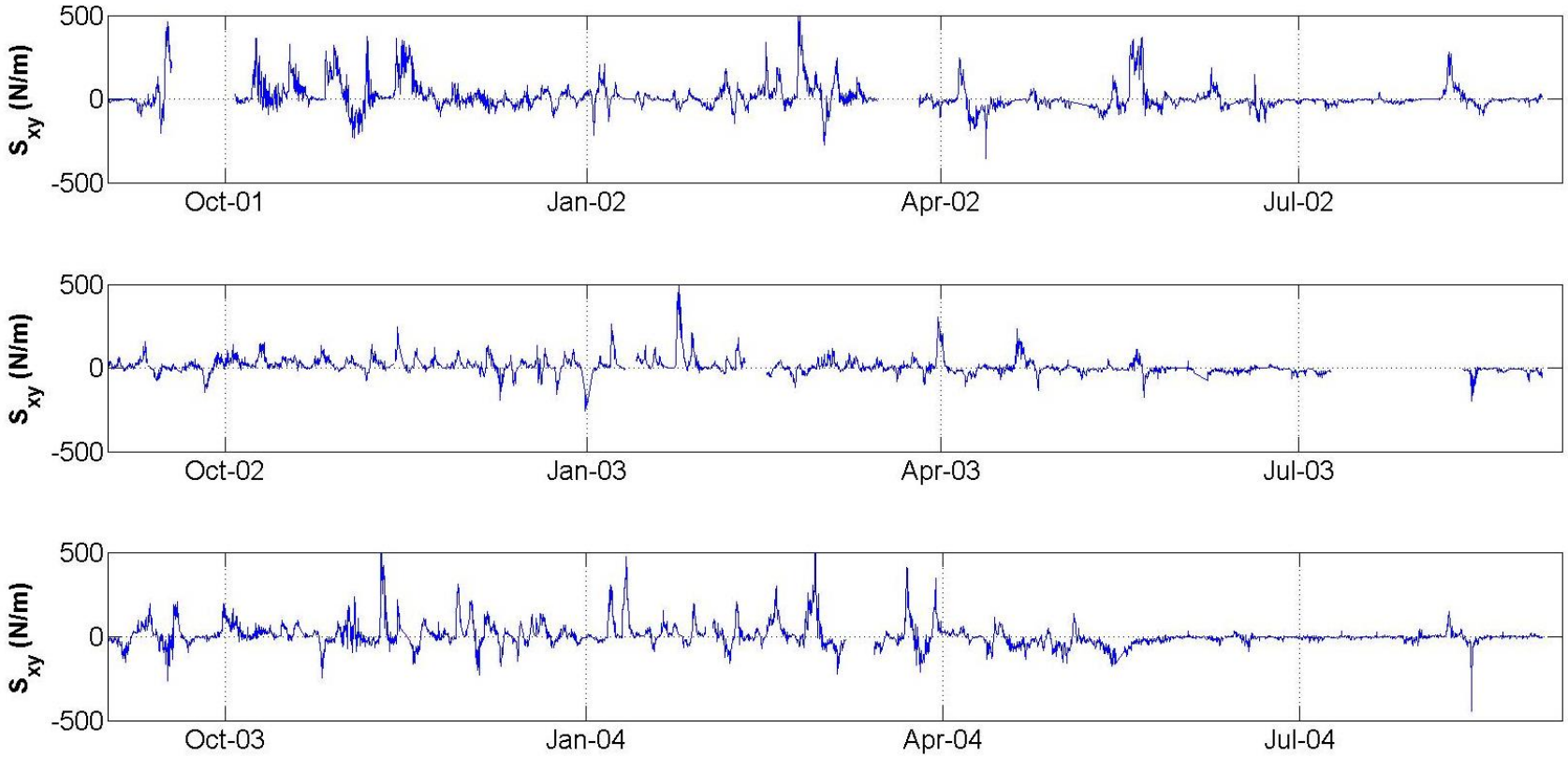

Figure D.1a: Radiation stress (S_{xy}) estimates from the Spessard Station (continue).

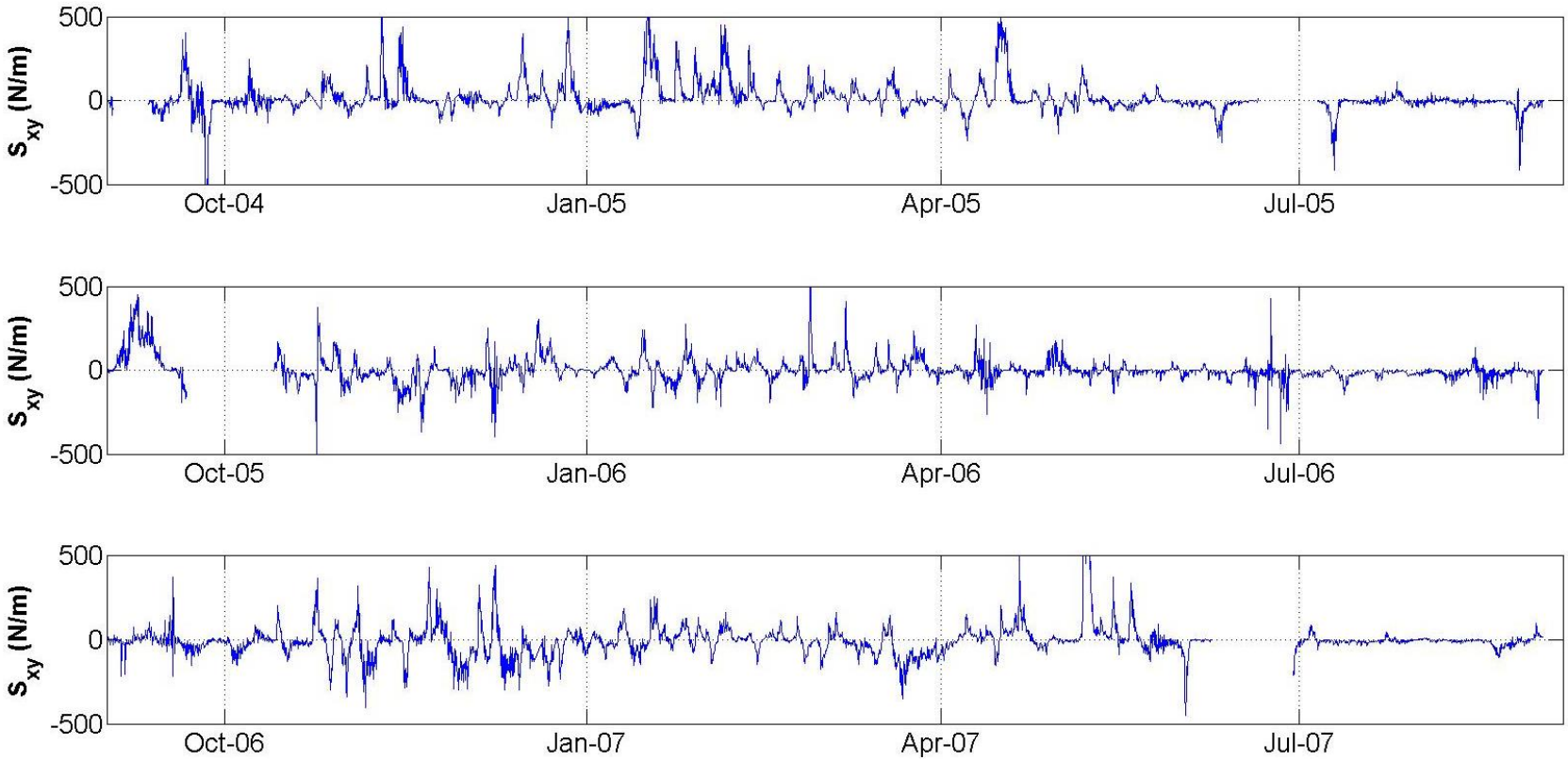

Figure D.1b: Radiation stress (S_{xy}) estimates from the Spessard Station (continue).

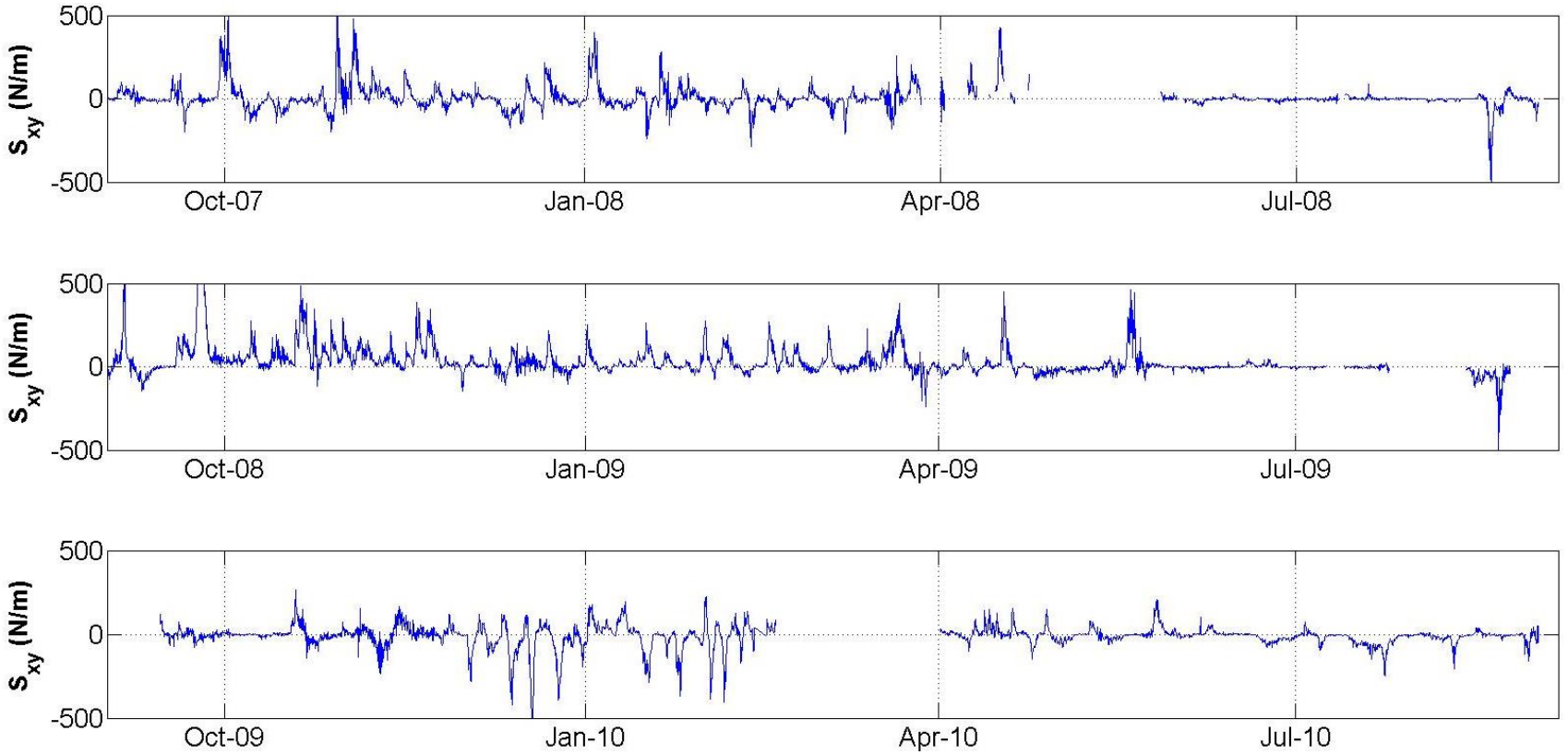

Figure D.1c: Radiation stress (S_{xy}) estimates from the Spessard Station (continue).

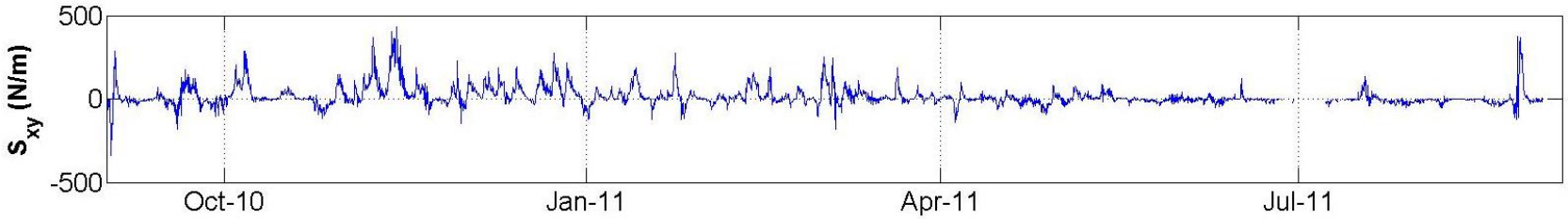

Figure D.1d: Radiation stress (S_{xy}) estimates from the Spessard Station (concluded).

APPENDIX E

Comparison of Time Scale Averages

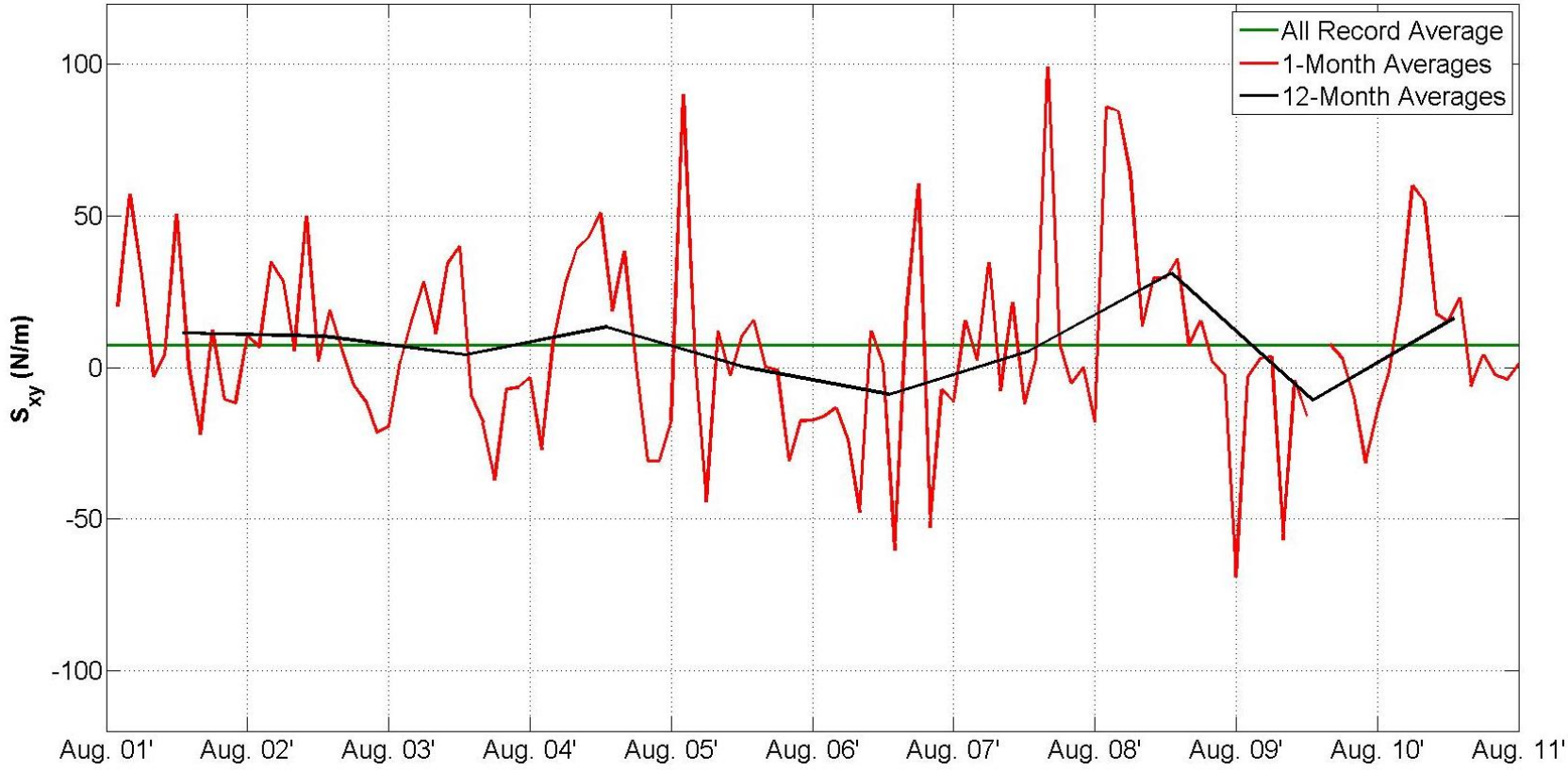

Figure E.1: Comparison Between 1-Month and 12-Month Radiation Stress (S_{xy}) Averages. The All Record Average is 7.22 (N/m).

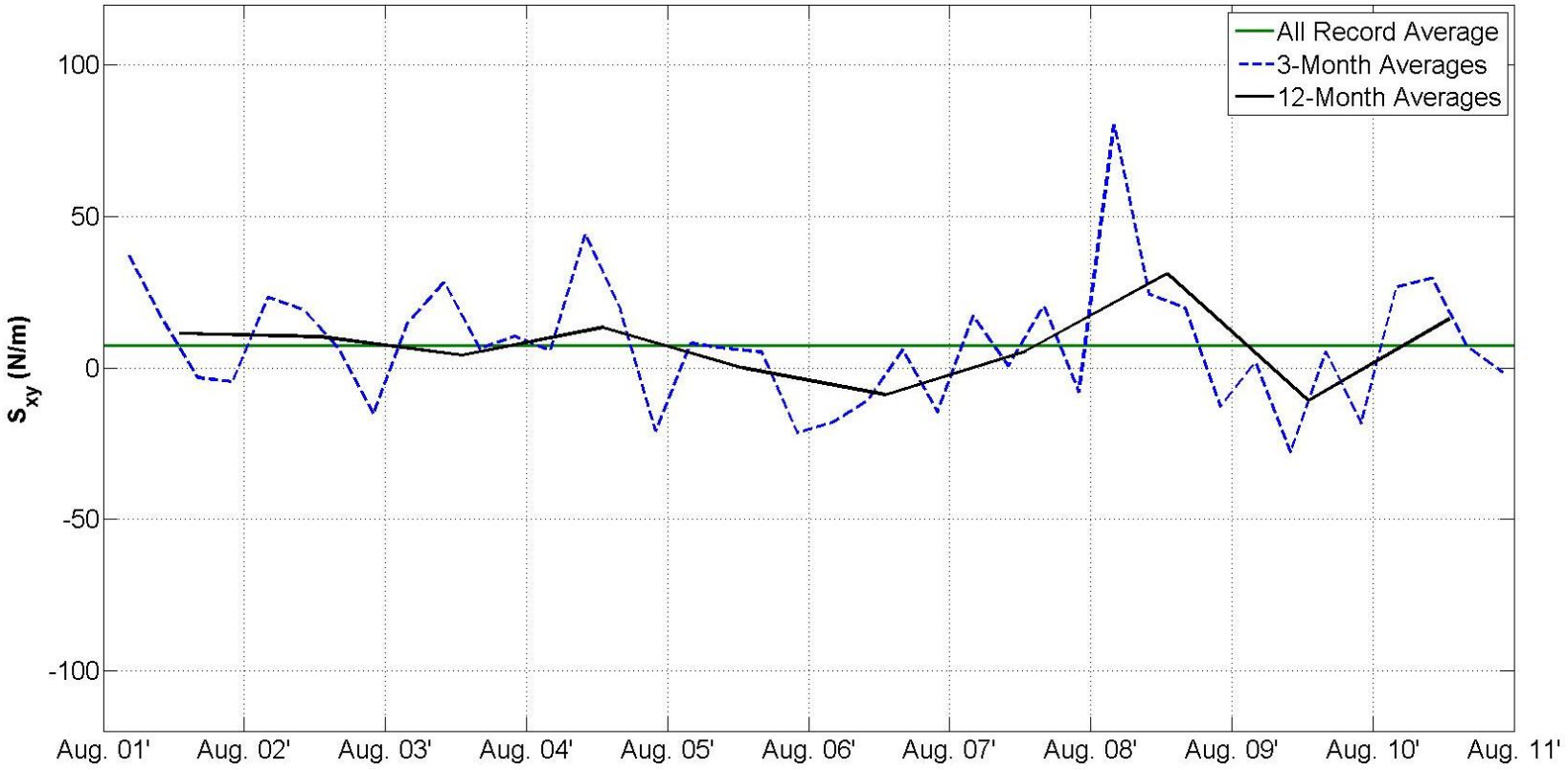

Figure E.2: Comparison Between 3-Month and 12-Month Radiation Stress (S_{xy}) Averages. The All Record Average is 7.22 (N/m).

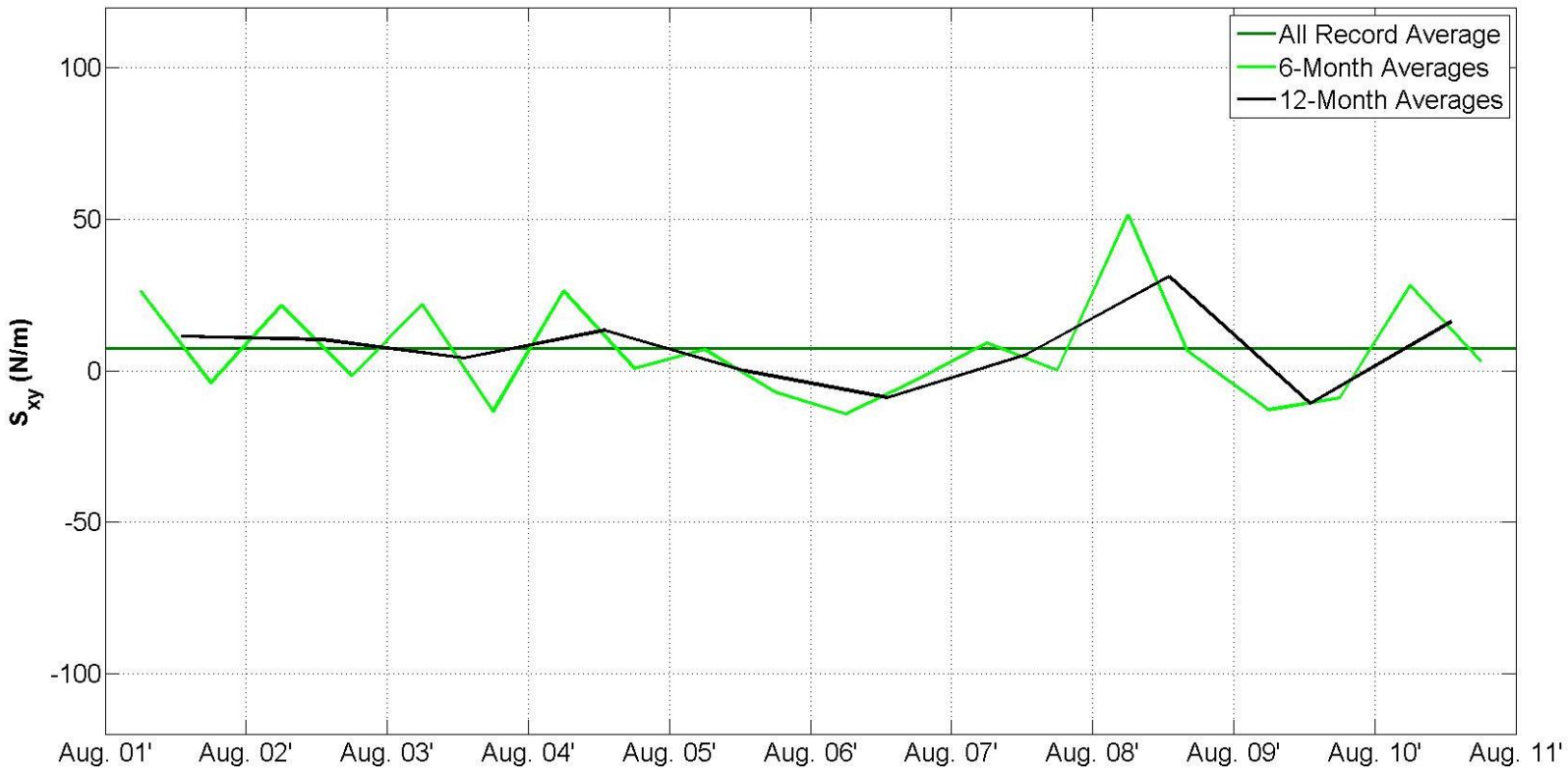

Figure E.3: Comparison Between 6-Month and 12-Month Radiation Stress (S_{xy}) Averages. The All Record Average is 7.22 (N/m).

VITA

Luis Montoya was born in United States of America (USA) and raised in Colombia. When he was 16 years old he moved back to the USA to finish his high school career and with hopes of playing division I soccer. He played 3 years in the University of North Florida (UNF) soccer team. In 2012, he graduated with honors and received a Bachelor of Science degree in Civil Engineering. During his last semester, Luis had the opportunity to meet Dr. Resio who at the time was developing a graduate coastal program at UNF. After doing some research on coastal engineering, Luis decided to join the program.

During his masters, Luis collaborated on various research projects with Dr. Dally, Dr. Resio and Dr. Bacopoulos. Finally, he plans to pursue a PhD degree in coastal engineering.